# Sabine Rödelsperger

# Real-time Processing
# of Ground Based Synthetic Aperture Radar (GB-SAR)
# Measurements

**München 2011**

# Real-time Processing
# of Ground Based Synthetic Aperture Radar (GB-SAR)
# Measurements

Vom Fachbereich 13 Bauingenieurwesen und Geodäsie
der Technischen Universität Darmstadt
zur Erlangung des akademischen Grades
eines Doktor-Ingenieurs (Dr.-Ing.) genehmigte Dissertation

von

## Dipl.-Ing. Sabine Rödelsperger

aus

Offenbach am Main

München 2011

Referent:     Prof. Dr.-Ing. Carl Gerstenecker
Korreferent:  Prof. Dr.-Ing. Matthias Becker

Tag der Einreichung:          11.01.2011
Tag der mündlichen Prüfung:  15.06.2011

# Zusammenfassung

In den letzten Jahren hat sich bodengestütztes Radar mit synthetischer Apertur (GB-SAR) zu einem leistungsstarken Instrument für die Überwachung von Bewegungen und Deformationen bei Massenbewegungen, z. Bsp. Hangrutschungen, Gletscher und Vulkane, entwickelt. Das Ziel dieser Arbeit ist die Entwicklung eines echtzeitfähigen Verfahrens für die Analyse von GB-SAR Daten, um den Status einer Massenbewegung mit der geringstmöglichen Verzögerung nach der Datenerfassung zu bestimmen.

Das GB-SAR Instrument IBIS-L ermöglicht die Fernerkundung eines Objektes bis zu einer Entfernung von 4 km, indem es Mikrowellen mit einer Frequenz von 17.2 GHz aussendet und die reflektierten Echos empfängt. Alle 5 bis 10 Minuten wird ein zweidimensionales Amplituden- und Phasen-Bild generiert mit einer Auflösung von 0.75 m in Entfernung und 4.4 mrad in Azimut (4.4 m in 1 km Entfernung). Die gemessene Amplitude hängt von Objektgeometrie und -reflektivität ab. Aus der Differenz zweier Phasenbilder, die zu unterschiedlichen Zeitpunkten gemessen wurden, können für jede Auflösungszelle Bewegungen in Blickrichtung abgeleitet werden. Es können ausschließlich relative Phasendifferenzen gebildet werden (zwischen $-\pi$ und $+\pi$), dass heißt, die Anzahl der Phasendurchgänge (Mehrdeutigkeit) ist unbekannt.

Außer von Bewegungen, wird die Phasendifferenz auch von atmosphärischen Störungen und Rauschen beeinflusst. Um die Bewegungen abzuleiten, müssen für alle Auflösungzellen im Bild sowie für alle Zeitschritte die Phasenmehrdeutigkeiten bestimmt und der atmosphärische Effekt geschätzt werden. Es existiert bereits eine Vielzahl von Techniken zum Bestimmen der Phasenmehrdeutigkeiten, die speziell für weltraumgestütztes SAR entwickelt wurden. Der Begriff Persistent Scatterer Interferometrie (PSI) steht für Techniken, die nur Zeitreihen von Punkten (PS) betrachten deren Phasenmessgenauigkeit gut ist (Standardabweichung unter 0.3 bis 0.4 rad) (Ferretti et al., 2001; Kampes, 2006). Die bekannten PSI Techniken sind allerdings nur bedingt echtzeitfähig, da sie Zeitreihen analysieren.

Das in dieser Arbeit beschriebene, echtzeitfähige Verfahren wurde speziell für die Anforderungen von bodengestütztem SAR entwickelt. Es ist eine Kombination von PSI mit Multi Model Adaptive Estimation (MMAE) (Marinkovic et al., 2005; Brown and Hwang, 1997). Die PS werden gemäß Ferretti et al. (2001) aus der Amplitudendispersion bestimmt, die ein Maß für die Phasenmessgenauigkeit darstellt. Daraus wird eine Untermenge (PS Candidates (PSC)) ausgewählt, die zur Schätzung von Mehrdeutigkeiten und Atmosphäre herangezogen werden. Aufgrund zeitlicher Änderungen der Qualität der Punkte durch z. Bsp. Steinschläge, ist die PSC Auswahl abhängig von der Zeit.

Zur Vereinfachung der Bestimmung der Mehrdeutigkeiten werden sie nicht aus den Zeitreihen selbst geschätzt, sondern aus der Differenz der Zeitreihen zweier benachbarter PSC, da dadurch atmosphärische Effekte reduziert werden. Für jede mögliche Mehrdeutigkeitslösung einer Zeitreihendifferenz existiert ein Kalman Filter um sequentiell den Status eines kinematischen Prozesses zu schätzen. In jedem Zeitschritt werden die neuen Beobachtungen den Filtern hinzugefügt. Die beste Mehrdeutigkeitslösung wird mit Hilfe von Wahrscheinlichkeiten bestimmt, die anhand der Differenz der beobachteten und prädizierten Phase berechnet werden. Nach der rein zeitlichen Mehrdeutigkeitsbestimmung wird für jeden Zeitschritt die räumliche Konsistenz geprüft und die Mehrdeutigkeiten der eigentlichen PSC Zeitreihen abgeleitet. Der atmosphärische Effekt wird aus einer Kombination von meteorologischen Daten und Filterung geschätzt. Anschließend werden die PS in das Netzwerk integriert.

Mit diesem Verfahren erhält man eine erste Schätzung der Bewegungen an den PS innerhalb weniger Sekunden bis Minuten nach der Datenerfassung. Mit jedem Zeitschritt werden neue Beobachtungen hinzugefügt und die Bestimmung der Mehrdeutigkeiten verbessert bis sie schließlich festgesetzt werden. Die endgültige Schätzung der Bewegungen liegt daher einige Minuten bis eine Stunde nach der Datenerfassung vor.

Die Leistungsfähigkeit der Technik wird anhand von synthetischen sowie beobachteten Daten gezeigt. Die Ergebnisse von Kampagnen an vier verschiedenen Orten werden dargestellt: ein Steinbruch in Dieburg, Deutschland, eine Felswand in Bad Reichenhall, Deutschland, eine Kraterflanke auf Sao Miguel, Azoren und eine Hangrutschung in der Nähe von Innsbruck in den Österreichischen Alpen.

4

# Summary

In the last years, Ground based Synthetic Aperture Radar (GB-SAR) has proven to be a powerful tool for monitoring displacements and deformation that accompany mass movements like e.g. landslides, glaciers and volcanic hazards. The goal of this thesis is to develop a real-time capable technique that allows to analyse GB-SAR data and assess the state of a mass movement with the least delay possible after a GB-SAR measurement is acquired.

The GB-SAR instrument IBIS-L allows the remote monitoring of an object at a distance of up to 4 km by transmitting microwaves at a frequency of 17.2 GHz and receiving the reflected echoes. Every 5 to 10 minutes, it delivers a two-dimensional amplitude and phase image with a range resolution of 0.75 m and a cross-range (azimuth) resolution of 4.4 mrad (4.4 m at a distance of 1 km). The amplitude depends on object geometry and reflectivity. By computing the difference of two phase images observed at two different points in time, displacements in line-of-sight can be derived for each resolution cell. Only relative phase differences can be formed (ranging between $-\pi$ and $+\pi$), thus, the number of full phase cycles (i.e. phase ambiguity) is unknown.

Apart from displacements, the phase difference is also influenced by atmospheric disturbances and noise. To determine displacements, it is necessary to unwrap the phase differences (i.e. determine the phase ambiguities) and estimate the atmospheric effect for each resolution cell and for each time step. Many different methods exist for phase unwrapping, mainly developed for spaceborne SAR. The term Persistent Scatterer Interferometry (PSI) describes a set of techniques, which analyses only phase time series at persistent scatterers (PS), i.e. resolution cells with a good phase standard deviation (usually less then 0.3 to 0.4 rad) (Ferretti et al., 2001; Kampes, 2006). The common PSI methods are, however, not directly real-time capable as they analyse time series.

The real-time analysis tool described in this thesis is especially designed for GB-SAR requirements. It is a combination of PSI with Multi Model Adaptive Estimation (MMAE) (Marinkovic et al., 2005; Brown and Hwang, 1997). The PS are selected according to Ferretti et al. (2001) using the amplitude dispersion index, which describes the phase accuracy. Only a subset of this selection, the PS candidates (PSC), are used for phase unwrapping and estimation of the atmosphere. Due to temporal changes of PS quality, caused by e.g. rock falls, the PSC selection is changing with time.

To simplify the unwrapping, the ambiguities are not estimated from the time series itself but rather on the difference of the time series of two neighbouring PSC. By that the atmospheric effect is reduced. For each possible ambiguity solution of a time series difference, a Kalman Filter exists to sequentially estimate the state of a kinematic process. At each time step new observations are added to the filter. The best ambiguity solution is selected based on probabilities, which are computed from the difference between observed and predicted phase. After this temporal unwrapping, a spatial unwrapping is performed for each time step to make sure that the determined solution is spatially consistent. The atmospheric effect is estimated after the unwrapping using a combination of meteorological data and filtering. Finally, the remaining PS are integrated into the network.

With this technique, a first estimation of the displacements at the PS is available a few seconds to minutes after the data acquisition. With every time step, new observations are added, which will improve the determination of ambiguities until they can be fixed. Thus, the final estimation of displacements is available a few minutes to one hour after the data acquisition.

The performance of the technique is shown by unwrapping synthetic data and real data from observation campaigns at four different locations: a quarry in Dieburg, Germany, a mountain side in Bad Reichenhall, Germany, a caldera flank on Sao Miguel, Azores and a landslide near Innsbruck in the Austrian Alps.

# Contents

# 1 Introduction

Hazards involving ground movements can lead to enormous human and economic losses. Ground movement and instabilities can either be caused by natural conditions and processes (e.g. climatic variations, volcanic activities, tectonic processes, glaciers) or by anthropogenic actions (e.g. mining, ground water withdrawal, deforestation). Every year, one Million people are exposed to weather-related landslide hazards around the globe (ISDR, 2009). Due to the recent climate change it is likely that the decrease of permafrost areas, changes in precipitation patterns and increase of extreme weather events will influence the weather-related mass movement activities (IPCC, 2007). Studies on the effect of climate change on landslides showed no significant increase of such events up to now but the geographic distribution, frequency and intensity is likely to change (ISDR, 2009; Collison et al., 2000; Modaressi, 2006). Continuous monitoring of such regions can give insight into mechanisms and triggers of hazardous events.

The monitoring of ground movements typically comprises the actual observation of displacement and deformation as well as the observation of triggering factors, such as e.g. rainfall or temperature. Geodetic methods, e.g. Global Positioning System (GPS), total stations and leveling, allow the continuous monitoring of displacements and deformation with high accuracy (e.g. Angeli et al., 2000; Gili et al., 2000). They are, however, limited to observations at distinct points. Laser scanning and photogrammetry deliver areal displacements by generating and comparing DEMs at different times (e.g. Bitelli et al., 2004). Photogrammetry can only be applied during day time and both methods are only operable during good weather conditions. Since the late 1970s, spaceborne Interferometric Synthetic Aperture Radar (InSAR) enables the monitoring of displacements of large areas with high spatial resolution during all weather conditions (Bamler and Hartl, 1998; Massonnet and Feigl, 1998). The temporal resolution, however, is limited by the repeat cycle of the satellite, which is usually several days. With the recent development of Ground based Synthetic Aperture Radar (GB-SAR), it is possible to determine displacements and deformation of areas, up to $4\,\mathrm{km}^2$ in size with high spatial resolution (few meters), high temporal resolution (several minutes) and high accuracy (submillimeters to millimeters) (Pieraccini et al., 2003; Luzi et al., 2006; Herrera et al., 2009). Due to the use of microwaves, the monitoring can continue during all weather conditions.

The result of one GB-SAR acquisition is a two-dimensional image with range and azimuth resolution containing amplitude and phase. The phase is dependent on the distance between instrument and resolution cell at the object. By acquiring two images, an interferogram, i.e. the areal phase difference map can be formed. It depends on displacement and deformation of the object relative to the instrument, atmospheric changes between object and instrument and noise. Only the relative phase difference, ranging between $-\pi$ and $+\pi$, can be measured. The number of full phase cycles $(2\pi)$, i.e. ambiguity, is unknown. Thus, the maximum object velocity observable is limited by the sampling rate. Additionally, noise and atmospheric disturbances can make it difficult to find the correct ambiguity, which has to be determined for each time step at each resolution cell.

The objective of this thesis is, to develop a tool to analyse GB-SAR data in real-time, i.e. with the least delay possible, which can then act as basis for making rapid decisions, e.g. in terms of countermeasures or evacuation. The analysis of GB-SAR data comprises the determination of ambiguities, i.e. phase unwrapping in space and time, and the correction of atmospheric effects.

In chapter 2, the basic principles and concepts of the Synthetic Aperture Radar (SAR) technique with focus on GB-SAR are discussed. The instrument IBIS-L, which was used for all tests and developments is introduced and its advantages and disadvantages to other common displacement monitoring techniques are described. Due to the use of microwaves, the geometry and properties of SAR images differ completely from those of optical images. Amplitude and achievable accuracy for phase differences are dependent on object geometry and material. Areas densely covered with vegetation are generally not observable while rock faces and barren land can be monitored with high accuracy.

In chapter 3, the state of the art of post processing SAR data is given. The chapter is focused on two important techniques: the conventional InSAR analysis, which evaluates interferogram by interferogram, and the Persistent Scatterer Interferometry (PSI), which evaluates the phase time series at distinct points. The disadvantage of the conventional InSAR analysis is that it is only based on interferograms, which works well for high quality data but fails completely when the noise is high due to e.g. poorly reflecting surfaces and atmospheric distortions. PSI only evaluates the phase at points of high quality. Both methods are described and similarities and differences between spaceborne SAR and GB-SAR analysis are pointed out.

In contrary to the InSAR analysis, PSI is usually not directly real-time capable due to the analysis of time series. Chapter 4 introduces a new PSI approach, especially designed for GB-SAR, which is capable of deriving

displacements in near-real-time, i.e. with the least delay possible. This technique combines the benefits of the conventional PSI approach with Multi Model Adaptive Estimation (MMAE) (Marinkovic et al., 2005; Brown and Hwang, 1997).

In chapter 5, the results of four measurement campaigns carried out with IBIS-L are presented: monitoring of an active quarry in Dieburg, Germany, monitoring of a mountain side in Bad Reichenhall, Germany, monitoring of a caldera wall on island Sao Miguel, Azores and monitoring of a landslide in the Austrian Alps in Gries im Sellrain. These four campaigns show the flexibility of the instrument and the real-time analysis technique.

Chapter 6 summarizes the findings and gives a short conclusion and outlook.

# 2 Principles of GB-SAR

Ground based Synthetic Aperture Radar (GB-SAR) is a novel technique based on microwave interferometry designed for monitoring displacements due to natural hazards and man-made structures. It provides two dimensional displacement maps with high spatial resolution (several meters) and high accuracy (i.e. standard deviation 1/10 mm to 1 mm). As an active remote sensing technology, it does not depend on external illumination and can therefore operate day and night under all weather conditions.

GB-SAR makes use of three basic techniques:

- Stepped Frequency Continuous Wave (SFCW): for obtaining range resolution;
- Synthetic Aperture Radar (SAR): for obtaining azimuth or cross-range resolution;
- Interferometry: for the determination of object displacements with high precision and accuracy.

The principles of the SFCW and SAR technique are described in section 2.1, while the interferometric technique is discussed in section 2.2.

The first proposal concerning the possibility of increasing the spatial resolution of radar observations using the SAR technique was made by Carl Wiley in the year 1951 (Curlander and McDonough, 1991). After several successful airborne SAR missions, the first civil spaceborne SAR mission (Seasat) was launched in 1978 by NASA. Since then, many SAR missions have been flown by various space agencies. The first European spaceborne mission was launched by ESA with ERS-1 in 1991 and later ERS-2 in 1995.

Up to now SAR has proven to be a valuable tool for all kinds of applications as

- Military tasks, e.g. reconnaissance and surveillance (Leachtenauer and Driggers, 2001);
- Ocean monitoring, e.g. tracking of sea ice (Rothrock et al., 1992), monitoring of oil spills (Brekke and Solberg, 2005) and measurement of wave properties (Schuler et al., 2004);
- Monitoring and characterization of ice, snow and glaciers (König et al., 2001);
- Monitoring mass movements (displacements) with interferometric SAR, e.g. earthquakes (Wright et al., 2001) and landslides (Strozzi et al., 2005);
- Thematic mapping, e.g. biomass mapping (Bergen and Dobson, 1999);
- Generation of Digital Elevation Models (DEMs) (Moreira et al., 2004), e.g. Shuttle Radar Topography Mission (SRTM) (Rabus et al., 2003).

The use of the SAR technique on the ground was proposed by the Joint Research Center (JRC) of the European Commission in the late 90s and the device named LiSA (Linear Synthetic Aperture Radar) was developed (Rudolf et al., 1999; Tarchi et al., 2000). At the beginning, test measurements were performed in a controlled environment until in 1998 the first outdoor measurement campaigns were carried out. In the following years, the main application was displacement monitoring of landslides and slopes (e.g. Antonello et al., 2004; Tarchi et al., 2003). The results were validated by means of conventional measurements with e.g. extensometers, distometers and GPS. The successful tests led to the foundation of the JRC spin-off company LiSALab srl in 2003 (http://www.lisalab.com). The company offers mainly monitoring services of natural hazards and man made structures with LiSA.

The first commercially available GB-SAR was developed by the Italian company Ingegneria dei Sistemi S.p.A. (IDS) in collaboration with the Department of Electronics and Telecommunication of the Florence University. It is named IBIS-L (Image By Interferometric Survey) and is being manufactured and sold by IDS (http://www.idscompany.it). All measurements presented in this study are carried out with this instrument. The specifications of IBIS-L are described in details in section 2.3.

## 2.1 GB-SAR Technique

SAR is an abbreviation for Synthetic Aperture Radar. While in Real Aperture Radar (RAR), image resolution is limited by the physical dimension of the antenna, in SAR the antenna is synthetically elongated by moving the sensor perpendicular to the look direction (Curlander and McDonough, 1991).

Radar stands for RAdio Detection And Ranging. An imaging radar system emits and receives electromagnetic waves in the radio spectrum to obtain information about distant objects. Typical frequency bands used for SAR are between L- and Ku-band (see Table 2.1). As it is an active remote sensing system, it provides its own illumination and can therefore operate day and night and penetrate clouds. Furthermore, it is a coherent

imaging technology which gathers amplitude and phase information of the reflected signal.

| Band name | Wavelength | Frequency |
|---|---|---|
| P-band | $30 - 75$ cm | $1 - 0.4$ GHz |
| L-band | $15 - 30$ cm | $2 - 1$ GHz |
| S-band | $7.5 - 15$ cm | $4 - 2$ GHz |
| C-band | $3.75 - 7.5$ cm | $8 - 4$ GHz |
| X-band | $2.5 - 3.75$ cm | $12 - 8$ GHz |
| Ku-band | $1.67 - 2.5$ cm | $18 - 12$ GHz |
| K-band | $1.11 - 1.67$ cm | $27 - 18$ GHz |
| Ka-band | $0.75 - 1.11$ cm | $40 - 27$ GHz |

Table 2.1: Microwave bands after Klausing and Holpp (2000).

The result of one SAR acquisition is a two-dimensional image with range and cross-range resolution. Each resolution cell contains amplitude and phase information. In the GB-SAR case, range resolution is obtained by the SFCW technique and cross-range resolution by the SAR technique. The two techniques are described in sections 2.1.1 and 2.1.2, respectively. In both cases, the sampling is done in the frequency domain instead of the spatial domain. Thus, the resulting raw image must be transformed from the frequency domain into the spatial domain by an Inverse Fourier transform. This step is called focusing. Details are shown in section 2.1.3. The geometric and radiometric properties of SAR images are not comparable to optical images. They mainly depend on the geometry of the structure but also on material and roughness. A short introduction into the properties of SAR images are given in sections 2.1.4 and 2.1.5.

### 2.1.1 Range Resolution

In case of an impulse radar, two targets illuminated by the instrument can be distinguished if the travel time of the pulse between the two targets is greater than the pulse width $\tau$. Shortening the pulse width will lead to a higher range resolution. This pulse can be fully synthesized by using the Stepped Frequency Continuous Wave (SFCW) technique (Paulose, 1994). The instrument transmits continuously a set of sweeps containing a stepped frequency signal with bandwidth $B$ and frequency step size $\Delta f$ (see Figure 2.1). The maximum resolution in range $\delta_r$ then depends on the bandwidth $B$ of the transmitted signal

$$\delta_r = \frac{c\tau}{2} = \frac{c}{2B},$$ (2.1)

whereas $c = 3 \times 10^8$ m/s is the speed of light (Bamler, 2000).
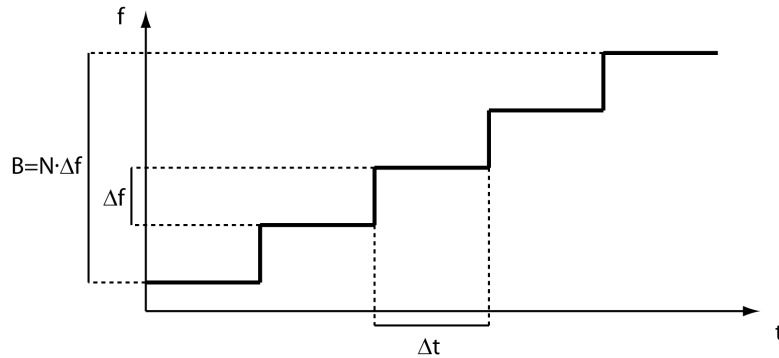


Figure 2.1: Transmitted SFCW signal.

The number of frequency steps must at least equal the number of resolution cells to avoid undersampling. It is important to note that increasing the number of frequency steps, while the bandwidth remains constant, does not improve the range resolution as it only depends on the bandwidth. The number of frequency steps $N$ necessary is related to the range resolution $\delta_r$ and maximum range $r_{max}$ by

$$N = \frac{2r_{max}}{\delta_r}.$$ (2.2)

With bandwidth $B = N\Delta f$ and equation 2.1, the frequency step $\Delta f$ is

$$\Delta f = \frac{c}{4 r_{max}}. \tag{2.3}$$

The duration $\Delta t$ of one frequency sample must be long enough to receive the echo from the furthest target:

$$\Delta t = \frac{2 r_{max}}{c}. \tag{2.4}$$

### 2.1.2 Cross Range Resolution

The azimuth or cross-range resolution $\delta_{rc}$ of a Real Aperture Radar equals the beam width of the antenna and is defined by

$$\delta_{rc} = \frac{\lambda}{L} r, \tag{2.5}$$

with $r$ being the distance between instrument and target, $L$ the physical length of the antenna (real aperture) and $\lambda$ the wavelength of the transmitted signal (Curlander and McDonough, 1991).

When the real antenna is moved perpendicular to the look direction, one single target is contained in all echoes along the rail. In this way, a synthetic antenna array is created. At each sensor position along the rail, one single target contributes with about the same amplitude but the distance between antenna and target, thus the phase, is slightly altered (see Figure 2.2). This function of phase $\varphi$ versus position of the antenna on the linear rail $x$ is called phase history of a target at an orthogonal distance $y$:

$$\varphi(x) = 2\frac{2\pi}{\lambda}\sqrt{x^2 + y^2}. \tag{2.6}$$
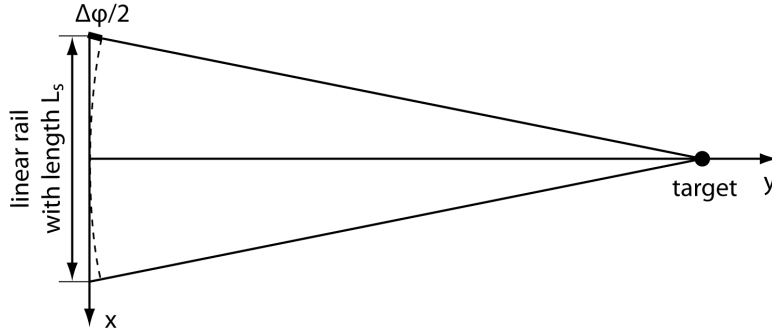


Figure 2.2: Relation between phase $\varphi$ of one single target at orthogonal distance $y$ and position on the rail $x$.

Angular wavenumber $k$ and spatial frequency $\nu$ are the spatial analog of angular velocity $\omega$ and frequency $f$ in the time domain of a signal. The spatial frequency $\nu$ is related to the phase $\varphi$ by

$$\nu(x) = \frac{k(x)}{2\pi} = \frac{1}{2\pi}\frac{d\varphi(x)}{dx}. \tag{2.7}$$

The derivative of phase $\varphi$ can be obtained by differentiation of equation 2.6:

$$\frac{d\varphi(x)}{dx} = \frac{4\pi}{\lambda}\frac{x}{\sqrt{x^2 + y^2}}. \tag{2.8}$$

Since the length of the rail is much smaller than the distance $(x \ll y)$, the derivative can be approximated by

$$\frac{d\varphi(x)}{dx} \approx \frac{4\pi}{\lambda}\frac{x}{y}. \tag{2.9}$$

Inserting equation 2.9 into equation 2.7 gives

$$\nu(x) = \frac{2}{\lambda}\frac{x}{y}. \tag{2.10}$$

Thus, frequency $\nu$ increases linearly with antenna position $x$ as shown in Figure 2.3. The total frequency shift $B_f$ of one single target at a distance $y = r$ is computed by inserting the length of the rail $L_s$ (i.e. the length of the synthetic antenna) into equation 2.10:

$$B_f = \nu(L_s/2) - \nu(-L_s/2) = \frac{2L_s}{\lambda r}.$$ 

(2.11)

The cross-range resolution $\delta_c$ is defined by

$$\delta_c = \frac{1}{B_f} = \frac{\lambda}{2L_s} r.$$ 

(2.12)

This equals the cross-range resolution of a Real Aperture Radar (see equation 2.5) except for the factor 2. The factor 2 comes from the fact that the phase difference between two synthetic antenna elements is two times the phase difference of two real antenna elements (Massonnet and Souyris, 2008).
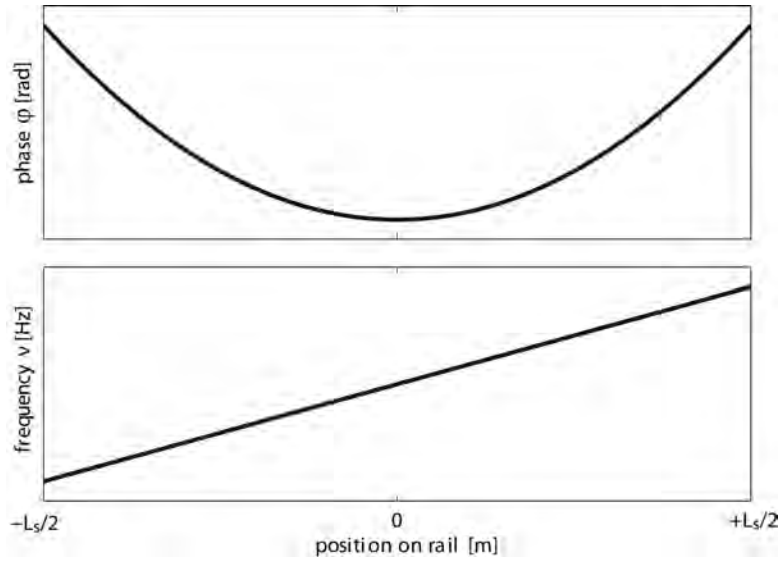


Figure 2.3: Phase history of one target: the upper and lower graph show the relation between position on the rail and phase $\varphi$ and frequency $\nu$, respectively.

### 2.1.3 Focusing

The echo of one single target inside the antenna beam is present in all transmitted frequencies and at each position on the linear rail and is therefore defocused. An ideal point target contributes to each pixel of the recorded raw image with the same amplitude while the phase is a function of transmitted frequency and sensor position on the rail. The observed amplitude and phase values must be transformed into a grid with spatial resolution. The necessary steps are shown in Figure 2.4. The focusing can be divided into range and cross-range focusing leading to an image with range and azimuth / cross-range resolution. Finally, the image can be transformed into a local $x$-$y$-grid for easier interpretation (see Figure 2.2), whereas $x = r \sin\alpha$ and $y = r \cos\alpha$ with $r$ being range and $\alpha$ azimuth with respect to the look direction of the GB-SAR.



Figure 2.4: Image resolution of unfocused and focused SAR data.

As shown in section 2.1.1, the sampling in range is done in the frequency domain using the SFCW technique. Thus, the sampled data of one column of the raw image can be transformed into the spatial domain by a discrete inverse Fourier transform. The discrete Fourier transform is defined by

$$
\begin{aligned}
F_k &= \sum_{l=0}^{N-1} f_l \cdot e^{\frac{2\pi i}{N} kl}, \qquad 0 \le k \le N-1, \\
f_l &= \sum_{k=0}^{N-1} F_k \cdot e^{-\frac{2\pi i}{N} kl}, \qquad 0 \le l \le N-1,
\end{aligned}
\tag{2.13}
$$
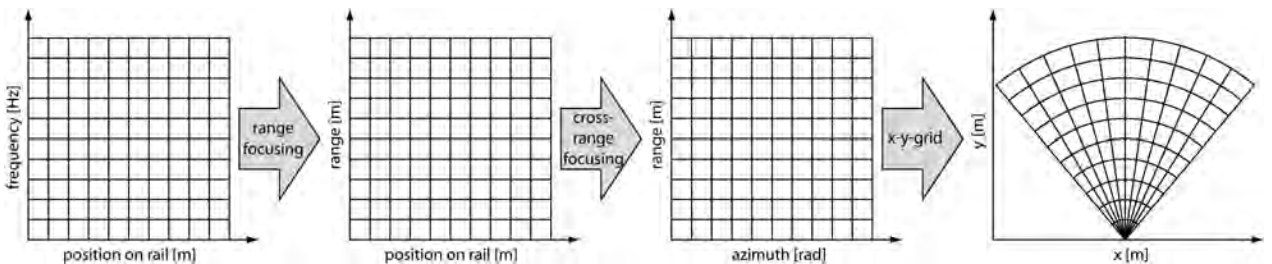
whereas the latter is the inverse transform. $f$ and $F$ are the function in space and frequency domain, respectively and $N$ is the number of frequency steps (Curlander and McDonough, 1991).

In section 2.1.2, it was derived that the sampling from different view points along the linear rail can be regarded as sampling in the frequency domain with a linear frequency shift. This leads to the conclusion that the cross-range focusing can be done by a discrete inverse Fourier transform as well.

Figure 2.5 shows an example of the focusing of a GB-SAR image. The unfocused raw image is given in Figure 2.5a. By applying the inverse Fourier transform to each column, the image is focused in range (see Figure 2.5b). Doing the same for the rows results in a fully focused image (see Figure 2.5c) with range and cross-range resolution. In Figure 2.5d the focused image is shown in a $x$-$y$-grid.



(a) Unfocused image

(b) Range focused image

(c) Focused image

(d) Focused image (x-y grid)
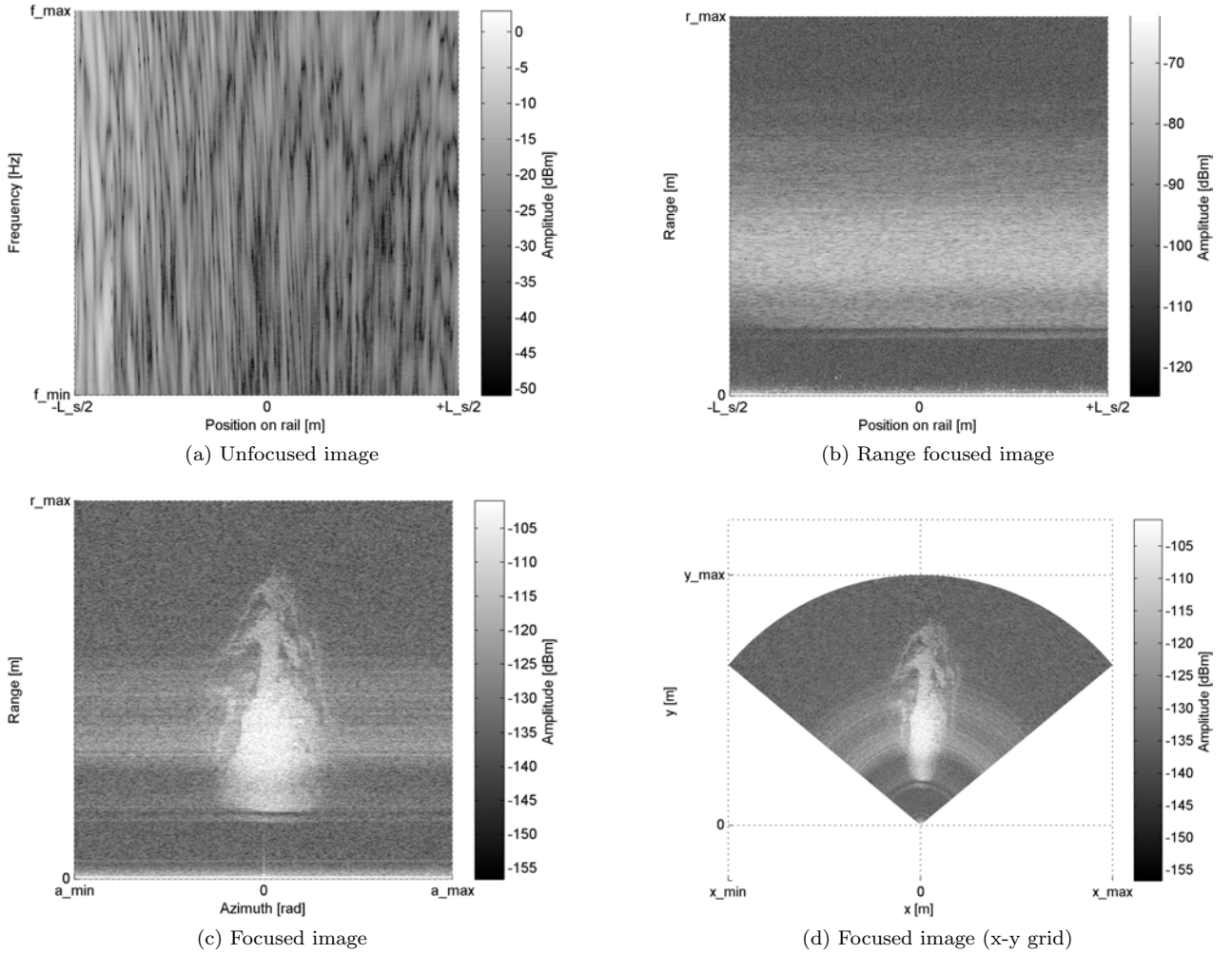
Figure 2.5: Example for the different stages of GB-SAR focusing (Amplitude only).

Due to the fact that the length of the synthetic aperture as well as the transmitted sweep are finite (i.e. band limited), the focusing of an ideal point target produces side lobes which can interfere with the signal of other targets (see Figure 2.7a). This is especially a problem when highly reflective targets are present in the observed scene. To reduce the side lobes, a window function can be applied before focusing (Curlander and McDonough,

1991). Optimal window functions are e.g. the Hamming window, Hann window or the Kaiser window (Harris, 1978):

$$w_{\text{Hamming}}(n) = 0.54 - 0.46 \cos\left(2\pi \frac{n}{N-1}\right),$$

$$w_{\text{Hann}}(n) = 0.5 - 0.5 \cos\left(2\pi \frac{n}{N-1}\right),$$

$$w_{\text{Kaiser}}(n) = \frac{I_0\left(\pi\beta\sqrt{1-\left(\frac{2n}{N-1}-1\right)^2}\right)}{I_0\left(\pi\beta\right)},$$

(2.14)

with $N$ being the window length, $\beta$ Kaiser window shaping parameter and $I_0$ the zeroth order modified Bessel function of the first kind. Exemplary, the Hann and Kaiser window functions are displayed in Figure 2.6 as function of transmitted frequency and sensor position. For $\beta = 6.0$, the Kaiser window is very similar to the Hann window. The larger $\beta$, the narrower the Kaiser function becomes and the better is the side lobe suppression. The disadvantages are the increasing loss of peak power and the decreasing resolution (i.e. broadening of the main lobe). The optimal window function must therefore be a trade-off between side lobe suppression and specified disadvantages.



Figure 2.6: Different window functions for sidelobe suppression in range and cross-range focusing.
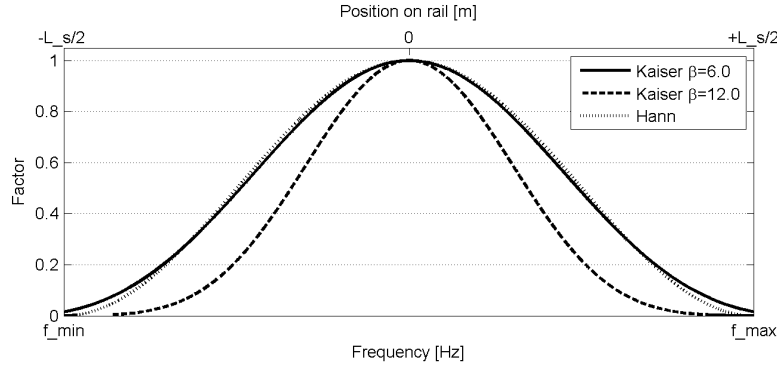
Figure 2.7 shows the focused image of an ideal point target without and with different window functions. The power of the sidelobes decreases considerably, which shows the necessity for using a window function to improve focusing. Without the window function, Figure 2.7a still appears to be out of focus. The side lobe suppression is best in Figure 2.7c with $\beta = 12.0$ but the broadening of the main lobe is clearly visible.

### 2.1.4 Geometric Properties

The geometry of a SAR image cannot be compared to optical remote sensing technologies. The range resolution concept produces geometric distortions in terrain with irregular topography because the resolution on the ground is different to the slant range resolution (see Figure 2.8). The most important consequence of this concept is that all targets in one azimuth and range resolution cell but with different elevation are mapped indistinguishably to the same pixel. This should be considered when choosing the sensor position.

The ground range resolution $\delta_{gr}$ is always worse than the resolution in slant range $\delta_r$. It depends on the elevation angle $\beta$ and slope inclination $\theta$ and can be approximated by

$$\delta_{gr} = \frac{\delta_r}{\cos\gamma}.$$

(2.15)

whereas $\gamma = \beta - \theta$ is the local incidence angle. The larger $\gamma$, the worse the ground range resolution becomes. For $\gamma = 0°$, the ground range resolution is theoretically equal to the slant range resolution. However, no energy will be scattered back due to specular scattering (see section 2.1.5).

To determine the ground range resolution and for geocoding a GB-SAR image, a DEM is necessary. The local two-dimensional image coordinate system $(x, y)$ as introduced in Figure 2.2 is defined by its origin being located in the center of the GB-SAR rail, its $x$-axis coinciding with the direction of sensor movement along the linear rail and its $y$-axis being perpendicular to the $x$-axis along the line of sight (see Figure 2.10a). For geocoding,

(a) No window

(b) Kaiser window ($\beta = 6.0$)

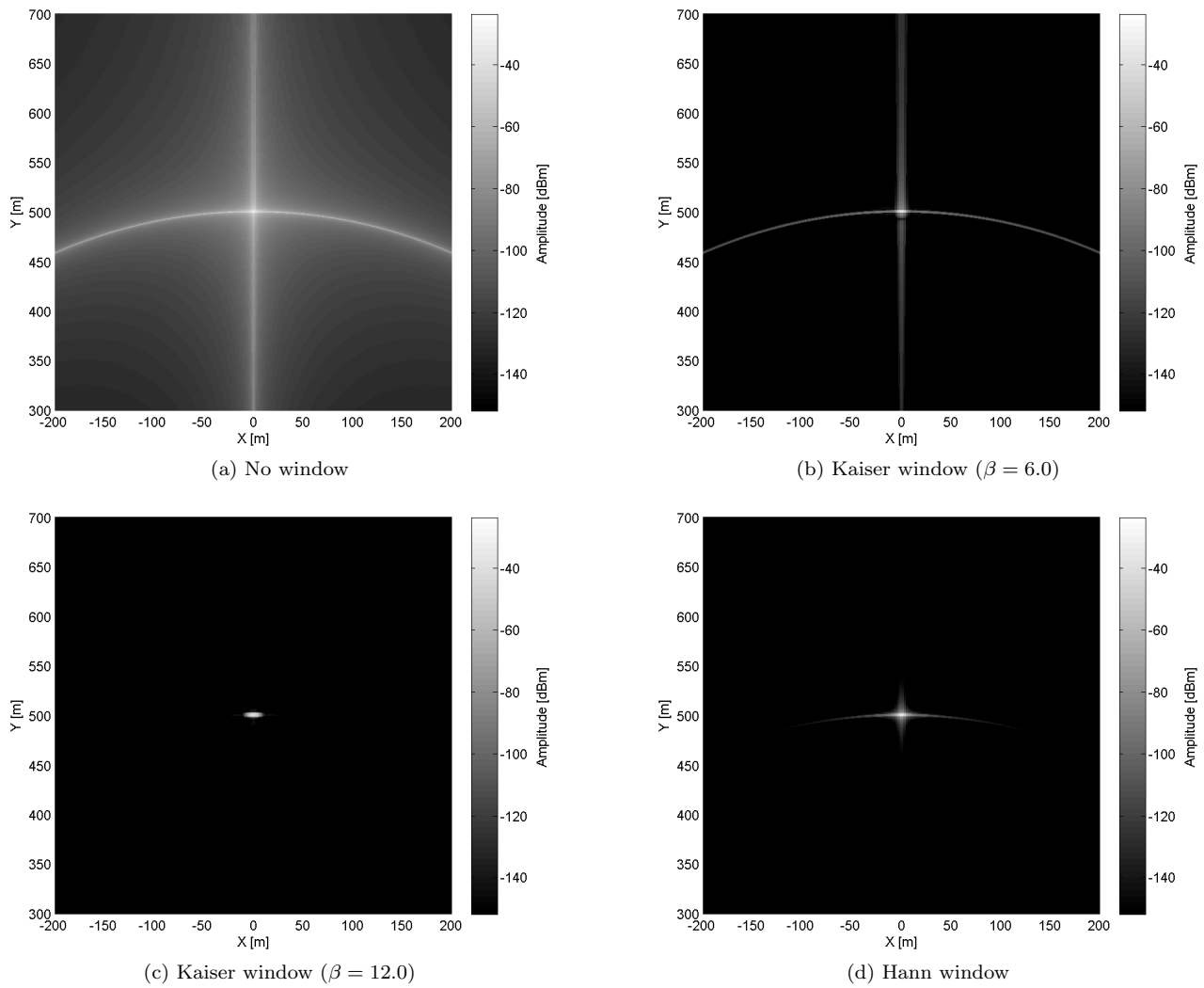(c) Kaiser window ($\beta = 12.0$)

(d) Hann window

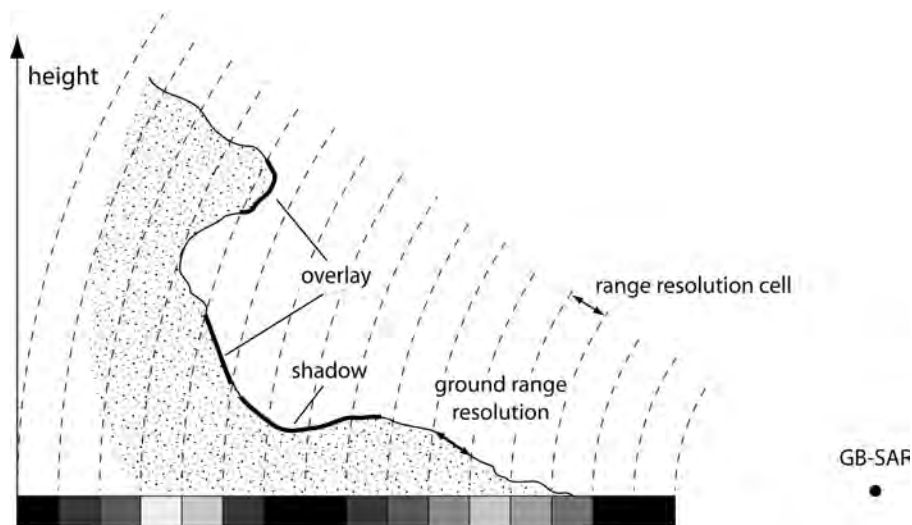Figure 2.7: Influence of different window functions on focusing of an ideal point target.



Figure 2.8: Concept of range resolution with GB-SAR at a complex slope. The azimuth is constant. The row of pixels at the bottom represents the intensity of the backscattered signal in the different resolution cells whereas white is the highest intensity.
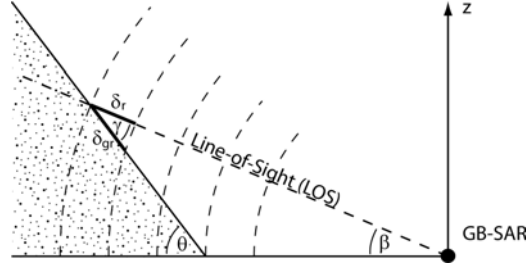
Figure 2.9: Relation between slant range resolution $\delta_r$ and ground range resolution $\delta_{gr}$ of a GB-SAR.

a local three-dimensional coordinate system $(X, Y, Z)$ is introduced which can be transformed into any global coordinate system. Its origin is located in the center of the GB-SAR rail, its $X$-axis coincides with the $x$-axis of the local two dimensional system, its $Z$-axis is the vertical axis pointing to the zenith and its $Y$ axis completes the right-hand coordinate system (see Figure 2.10a).

The relation between the $x$-$y$-system and the $X$-$Y$-$Z$-system is given by

$$
\begin{aligned}
r = \sqrt{x^2 + y^2} \quad &= \sqrt{X^2 + Y^2 + Z^2}, \\
\tan\alpha = \frac{x}{y} \quad &= \frac{X}{\sqrt{Y^2 + Z^2}},
\end{aligned}
\tag{2.16}
$$

with $r$ being the distance between sensor and target and $\alpha$ the azimuth with respect to the look direction of the GB-SAR.

The standard deviation of geocoding depends on the standard deviation of the DEM height $\sigma_Z$ as shown in Figure 2.10b. The standard deviation in Line Of Sight (LOS) direction $\sigma_P$ can be approximated by

$$
\sigma_P = \tan\beta\,\sigma_Z \qquad \text{with} \qquad P = \sqrt{X^2 + Y^2}.
\tag{2.17}
$$
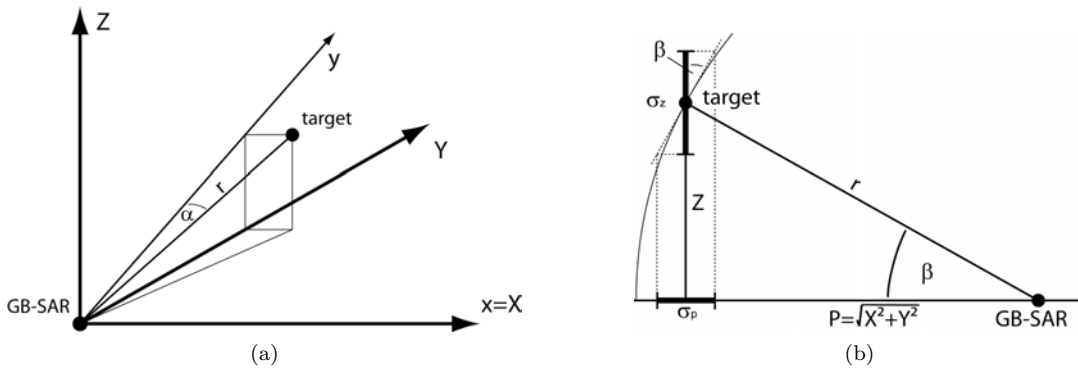


Figure 2.10: Figure (a) shows the relation between the local image coordinate system $(x,y)$ and three-dimensional system $(X,Y,Z)$. Figure (b) illustrates the relation of geocoding standard deviation in LOS $\sigma_P$ with the standard deviation of height $\sigma_Z$.

### 2.1.5 Radiometric Properties

The radar equation describes the relation between transmitted power $P_e$ and received power $P_r$ (Massonnet and Souyris, 2008):

$$
P_r = P_e \frac{\lambda^2}{(4\pi)^3} \frac{G^2}{r^4} \frac{\sigma}{L},
\tag{2.18}
$$

with $\lambda$ being the wavelength, $G$ the antenna gain, $r$ the distance, $L$ the loss due to atmosphere and $\sigma$ the Radar Cross Section (RCS) of the target. The RCS depends on target geometry and material and describes the effective area of an object measured in square meters. A target that radiates perfectly isotropic (e.g. a sphere) has a RCS that equals the target's physical extent. The larger the RCS, the higher is the amount of energy reflected back.

To determine the RCS, it is necessary to distinguish between point targets and extended or distributed targets (Curlander and McDonough, 1991; Massonnet and Souyris, 2008). A resolution cell consists of many individuals scatterers all contributing to the observed amplitude and phase. Point targets are targets that act as dominant scatterer within a resolution cell, i.e. the amplitude is much higher than the amplitude of all other contributors (see Figure 2.11a). Distributed targets are targets where no scatterer dominates (see Figure 2.11b).



(a) Point target

(b) Distributed target
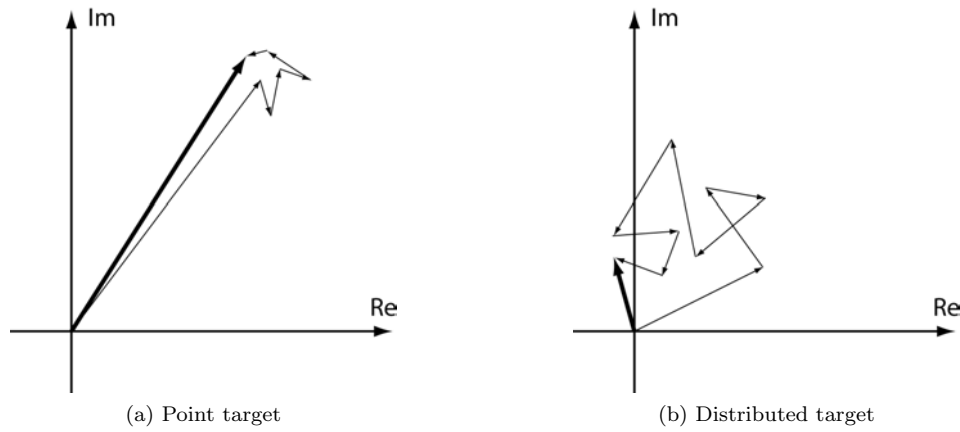
Figure 2.11: Phasor plot of a point target with a dominant scatterer (a) and of an distributed target (b). The thin arrows are the phasors of the individual scatterers within the resolution cell; the bold arrow is the sum of these phasors, i.e. the observed value of this resolution cell.

The RCS of a point target can be calculated analytically for objects with simple shapes. Special radar reflectors (e.g. corner reflectors) made of metal are designed for optimal reflection (see Figure 2.12). Table 2.2 gives the RCS of different radar reflectors as well as the physical extent to obtain a RCS of $\sigma = 1000$ m$^2$. For a wavelength of $\lambda = 17.4$ mm, the RCS of a square trihedral corner reflector with edge length $a = 0.3$ m is $\sigma = 1000$ m$^2$, which equals the RCS of a sphere with radius $r = 17.8$ m.



(a) Plate          (b) Dihedral          (c) Trihedral          (d) Trihedral (square)          (e) Trihedral (round)
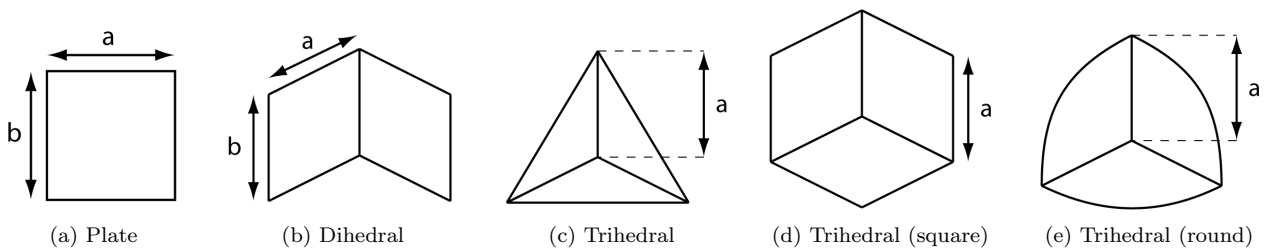
Figure 2.12: Different types of radar reflectors.

The simplest radar reflectors are metallic plates and dihedral reflectors. Their disadvantage is that the RCS depends highly on the aspect angle and thus they need to be adjusted exactly. For the most applications, trihedral corner reflectors are best because of their stability and their tolerance for inaccurate adjustment.

The backscatter coefficient $\sigma^0$ describes the relation between the RCS of a target $\sigma$ and its physical area $S$

$$\sigma^0 = \frac{\sigma}{S} \qquad \text{or} \qquad \sigma^0_{[dB]} = 10 \cdot (\log \sigma - \log S). \qquad (2.19)$$

It can be used to describe the target properties of distributed targets. Most natural surfaces can be regarded as distributed targets with backscatter coefficients of $\sigma^0 < 1$. The backscattering coefficient depends highly on the scattering mechanism involved. Scattering mechanisms can be classified into surface and volume scattering (Curlander and McDonough, 1991). The amount of energy reflected back due to surface scattering depends on

| Reflector type | RCS | $\sigma = 1000 \text{ m}^2$ |
|---|---|---|
| Sphere | $\sigma = \pi r^2$ | $r = 17.8$ m |
| Plate | $\sigma = 4 \frac{\pi a^2 b^2}{\lambda^2}$ | $a = b = 0.39$ m |
| Dihedral | $\sigma = 8 \frac{\pi a^2 b^2}{\lambda^2}$ | $a = b = 0.33$ m |
| Trihedral | $\sigma = \frac{4}{3} \frac{\pi a^4}{\lambda^2}$ | $a = 0.52$ m |
| Trihedral (square) | $\sigma = 12 \frac{\pi a^4}{\lambda^2}$ | $a = 0.30$ m |
| Trihedral (round) | $\sigma = \frac{16}{3} \frac{\pi a^4}{\lambda^2}$ | $a = 0.37$ m |

Table 2.2: RCS for different radar reflector types after Klausing and Holpp (2000) and size of reflectors to obtain a RCS of $\sigma = 1000$ m$^2$

surface roughness, wavelength and incidence angle. The smoother the surface, the less power is backscattered because the surface behaves like a mirror. Surfaces appear smooth when the Rayleigh roughness criterion is satisfied (Massonnet and Souyris, 2008)

$$h < \frac{\lambda}{8 \sin \gamma}. \tag{2.20}$$

whereas $h$ is the root mean square variation in surface height, $\gamma$ the incidence angle and $\lambda$ the wavelength.

Volume scattering occurs when the radar wave penetrates the objects surface. The penetration depth depends on wavelength and surface characteristics. It increases with higher wavelengths and decreases with an increase of water content.

## 2.2 Interferometric SAR

Up to now, only the amplitude of a GB-SAR image was considered. The phase $\varphi$ is a function of distance $r$ between sensor and target:

$$2r = -\frac{\lambda}{2\pi}\varphi \implies \varphi = -\frac{4\pi}{\lambda}r. \tag{2.21}$$

The observed phase $\varphi^w$ (i.e. wrapped phase) is a relative phase, as it is always wrapped into the interval $[-\pi, \pi)$. The relation between absolute phase $\varphi$ (i.e. unwrapped phase) and observed phase $\varphi^w$ is given by

$$\varphi^w = \mathcal{W}\{\varphi\} = \text{mod}\{\varphi + \pi, 2\pi\} - \pi = \varphi - 2\pi n, \tag{2.22}$$

with $\mathcal{W}\{\cdot\}$ being the wrapping operator. The phase ambiguity $n$ (i.e. integer number of full phase cycles) is unknown. Thus the absolute distance $r$ cannot be determined.

Comparing two SAR images of the same area, either collected at different time periods and/or from different sensor positions, the phase difference $\phi^w$, i.e interferometric phase, is related to the changes in distance between sensor and target $\Delta r = r_2 - r_1$ by

$$\phi^w = \mathcal{W}\{\varphi_1^w - \varphi_2^w\} = \mathcal{W}\left\{-\frac{4\pi}{\lambda}(r_1 - r_2)\right\} = \mathcal{W}\left\{\frac{4\pi}{\lambda}\Delta r\right\}. \tag{2.23}$$

This technique is referred to as Interferometric Synthetic Aperture Radar (InSAR) (Hanssen, 2002). The maximum unambiguous change of distance $\Delta r_{max}$ is restricted by the wavelength $\lambda$:

$$\Delta r_{max} = \pm\lambda/4. \tag{2.24}$$

If amplitude $a$ and phase $\varphi$ are represented as complex value $z$ with

$$z = a \cdot e^{i\varphi} = a \cdot (\cos\varphi + i\sin\varphi), \tag{2.25}$$

an interferogram is formed by

$$z_1 z_2^* = a_1 a_2 \cdot e^{i(\varphi_1 - \varphi_2)}, \tag{2.26}$$

whereas $z^*$ is the complex conjugated of $z$.

If an interferogram is formed using two SAR images collected at different time periods but from the same sensor position, the resulting phase difference is related to temporal changes of the distance between sensor and target (e.g. displacements). The difference between the two time periods is referred to as the temporal baseline $B_t$.

If the two SAR images are collected at the same time period but from different sensor positions, the resulting phase difference depends on the topography of the illuminated area. The effective distance between the two sensors is referred to as spatial baseline $B_s$. In conventional spaceborne InSAR, a temporal and spatial baseline are present whereas in GB-SAR the spatial baseline is usually zero, if it is not introduced intentionally.

Depending on the type of baseline, the interferometric phase $\phi^w$ is the sum of several effects:

$$\phi^w = \underbrace{\phi_{topo}}_{f(B_s)} + \underbrace{\phi_{disp} + \phi_{atm}}_{f(B_t)} + \phi_{noise} - 2\pi n. \tag{2.27}$$

$\phi_{topo}$ is the phase difference due the topography in case of a spatial baseline, $\phi_{disp}$ and $\phi_{atm}$ are temporal phase changes due to displacement and atmospheric effects, $\phi_{noise}$ is noise and $n$ is the integer phase ambiguity. The different components of the interferometric phase equation are described in detail in the following sections 2.2.1, 2.2.2 and 2.2.3. Its stochastic properties are discussed in sections 2.2.4 and 2.2.5.

The left side of equation 2.27 is the observed phase difference while the right side contains the unknown parameters. In case the application is to determine a DEM, equation 2.27 can be rearranged to solve for $\phi_{topo}$:

$$\phi_{topo} = \phi^w - \phi_{disp} - \phi_{atm} - \phi_{noise} + 2\pi n. \tag{2.28}$$

If the spatial baseline is produced by shifting the sensor vertically in-between two acquisitions also a temporal baseline exists. Thus, the time-dependent components are still part of the equation. The equation could be simplified considerably by using two vertically displaced antennas receiving at the same time. Then all time-dependent components of the functional model ($\phi_{disp}$ and $\phi_{atm}$) would be eliminated.

For displacement monitoring applications, $\phi_{disp}$ can be determined by

$$\phi_{disp} = \phi^w - \phi_{atm} - \phi_{noise} + 2\pi n, \tag{2.29}$$

whereas it is assumed that the spatial baseline is zero. The phase unwrapping, i.e. the determination of integer ambiguity $n$ of equations 2.28 and 2.29 is the key of InSAR processing. As it is a non-linear and non-unique problem, it is also the most difficult task (Ghiglia and Pritt, 1998), which cannot be solved without additional assumptions. If the sampling interval is $\Delta t$, the linear displacement rate $v$ of a single target is limited to $v < \frac{\lambda}{4\Delta t}$ to avoid phase ambiguities. Phase unwrapping algorithms will be briefly discussed in section 3.1.

### 2.2.1 Atmosphere

The propagation of the radar wave through the atmosphere is influenced by the variation of atmospheric properties. In the used frequency band, the atmospheric delay is independent of frequency. The atmospheric effect of the interferometric phase is a function of changes of the refractive index $\Delta n$ (Luzi et al., 2004)

$$\phi_{atm} = \frac{4\pi}{\lambda} \Delta n r, \tag{2.30}$$

where $\Delta n$ can be computed from temperature, humidity and pressure differences. As proposed in Zebker et al. (1997), the atmospheric phase can be expressed by

$$\phi_{atm} = \frac{4\pi}{\lambda} \left( 7.76 \times 10^{-5} \int_0^R \frac{P}{T} dr + 3.73 \times 10^{-1} \int_0^R \frac{e}{T^2} dr \right), \tag{2.31}$$

with $P$ being the atmospheric pressure in hPa, $T$ the temperature in Kelvin, $e$ the partial pressure of the water vapour in hPa and $R$ is the distance between target and instrument. The first part of the equation is the hydrostatic or dry component and the second part the wet component. Generally, not the partial pressure of the water vapour is observed by weather stations but relative humidity $h$. The relation between $e$ and $h$ is given by (Kraus, 2004)

$$e = \frac{hE}{100} \quad \text{with} \quad E = 6.107 \cdot \exp\left( \frac{17.27 \cdot (T - 273)}{T - 35.86} \right). \tag{2.32}$$

Microwaves are most sensitive to humidity changes. At a distance of 1000 m, the atmospheric effect induced by a humidity change of 1 % along the propagation path at a temperature of 20 °C and a pressure of 1013 hPa amounts to almost $\phi_{atm} = 42° \approx \pi/4$ for Ku-band radar ($\lambda = 17.4$ mm). To account for the atmospheric effect, meteorological observations can be used. Typical standard deviations of weather station measurements are 0.3 K for temperature, 0.8 hPa for pressure and 2 % for humidity (e.g. Reinhardt, 2009). Figure 2.13 gives an

idea of the associated errors of atmospheric phase $\phi_{atm}$ following from the standard deviation of meteorological observations assuming constant conditions along the propagation path. The necessary equations are derived in appendix section A.1 by applying the error propagation law. Temperature and especially humidity measurement are the most critical values which determine the accuracy of the atmospheric phase. Since the atmospheric properties can only be observed at distinct points, the true atmospheric properties along the propagation path of the radar wave may differ considerably during difficult weather situations, e.g. high temporal and spatial variability of atmosphere due to deep clouds in mountainous regions. Further studies of possibilities to correct interferograms for the atmospheric effect are done in section 3.2.2.
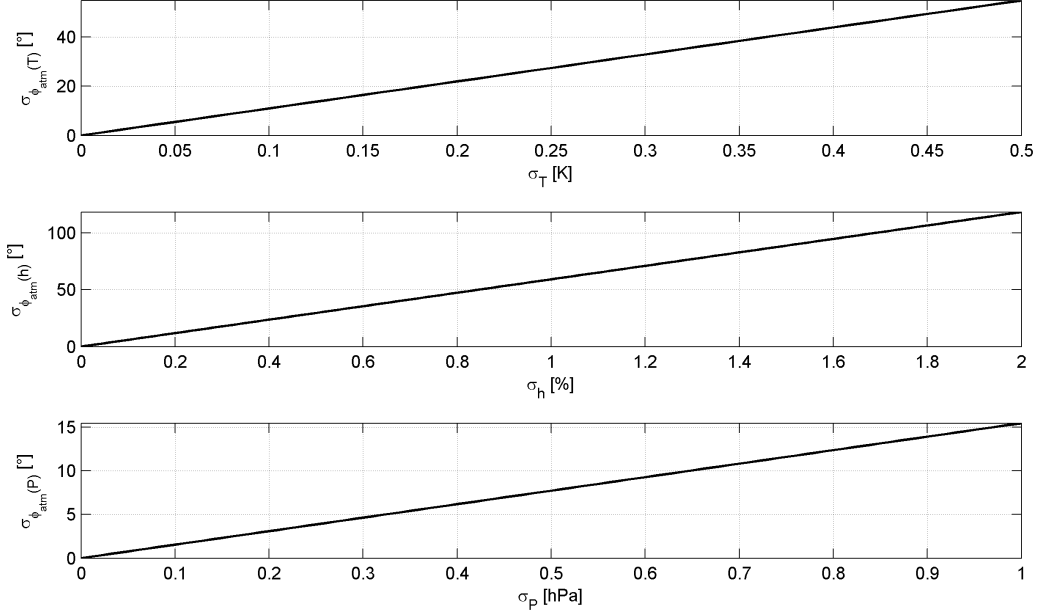


Figure 2.13: Standard deviation of atmospheric phase $\phi_{atm}$ estimated from weather data with respect to standard deviations of temperature $\sigma_T$, humidity $\sigma_h$ and pressure $\sigma_P$ at a temperature of 20 °C, a humidity of 50 % and a pressure of 1013 hPa. The total standard deviation $\sigma_{\phi_{atm}}$ can be computed by applying the error propagation law: $\sigma^2_{\phi_{atm}} = \sigma^2_{\phi_{atm}(T)} + \sigma^2_{\phi_{atm}(h)} + \sigma^2_{\phi_{atm}(P)}$. Please note the different scaling of the axes.

### 2.2.2 Topography

In general, topographic phase $\phi_{topo}$ is zero for GB-SAR. If a spatial baseline is deliberately introduced in-between two acquisitions, the height difference between sensor and target can be determined due to the different path length $r_1$ and $r_2$ of the two acquisitions (see Figure 2.14a). In case the radar sensor is shifted perfectly vertical, the interferometric phase $\phi_{topo}$ is related to height $\bar{z}$ of the target by (Noferini et al., 2007)

$$\phi_{topo} = \frac{4\pi}{\lambda}(r_2 - r_1),$$

$$\text{with} \qquad r_2 = \sqrt{B_s^2 + r_1^2 - 2B_s r_1 \cos\theta}, \tag{2.33}$$

$$\text{and} \qquad \cos\theta = \frac{\bar{z}}{r_1}.$$

The height $\bar{z}$ can be determined by

$$\bar{z} = \frac{B_s}{2} + \frac{\lambda}{4\pi}\frac{r_1}{B_s}\phi_{topo} - \left(\frac{\lambda}{4\pi}\right)^2 \frac{1}{2B_s}\phi_{topo}^2. \tag{2.34}$$

Since $r_1 \gg B_s$ and $r_1 \gg r_1 - r_2$, equation 2.34 can be approximated by

$$\bar{z} = \frac{\lambda}{4\pi}\frac{r_1}{B_s}\phi_{topo}. \tag{2.35}$$

If the spatial baseline is not vertical, height $\overline{z}$ has to be corrected for the baseline angle $\beta_s$ (see Figure 2.14b):

$$z = \overline{z} \cos \beta_s + r_0 \sin \beta_s \qquad \text{with} \qquad r_0 = \sqrt{r_1^2 - \overline{z}^2}. \qquad (2.36)$$



(a) Vertical spatial baseline              (b) Non-vertical spatial baseline
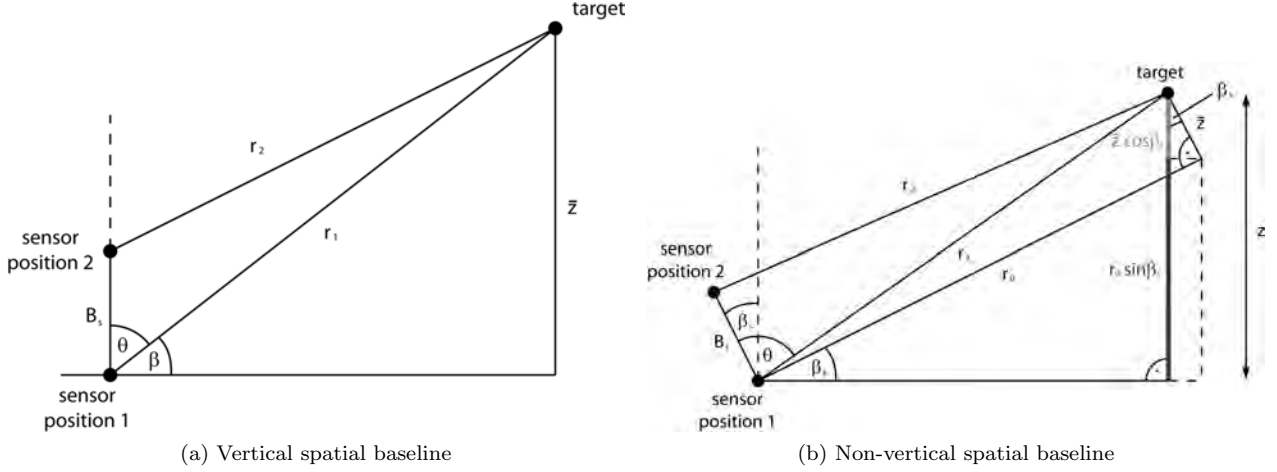
Figure 2.14: Topographic effect on the interferometric phase with a vertical and non-vertical spatial baseline.

Figure 2.15 shows the standard deviation of height $z$ following from the standard deviation of baseline angle $\sigma_{\beta_s}$, spatial baseline $\sigma_{B_s}$ and topographic phase $\sigma_{\phi_{topo}}$. The necessary equations are derived in appendix section A.2 by applying the error propagation law. For Ku-band radar ($\lambda = 17.4$ mm) with a vertical baseline ($B_s = 0.1$ m, $\sigma_{B_s} = 0.5$ mm, $\beta_s = 0.0°$, $\sigma_{\beta_s} = 0.1°$) and a phase change of one fringe ($\phi_{topo} = 2\pi$, $\sigma_{\phi_{topo}} = 20°$), the topographic height is $z = 87$ m with a standard deviation of $\sigma_z = 5.1$ m at a distance of 1000 m. Basically, the ability to correct the atmospheric effect determines the accuracy of the topographic phase.
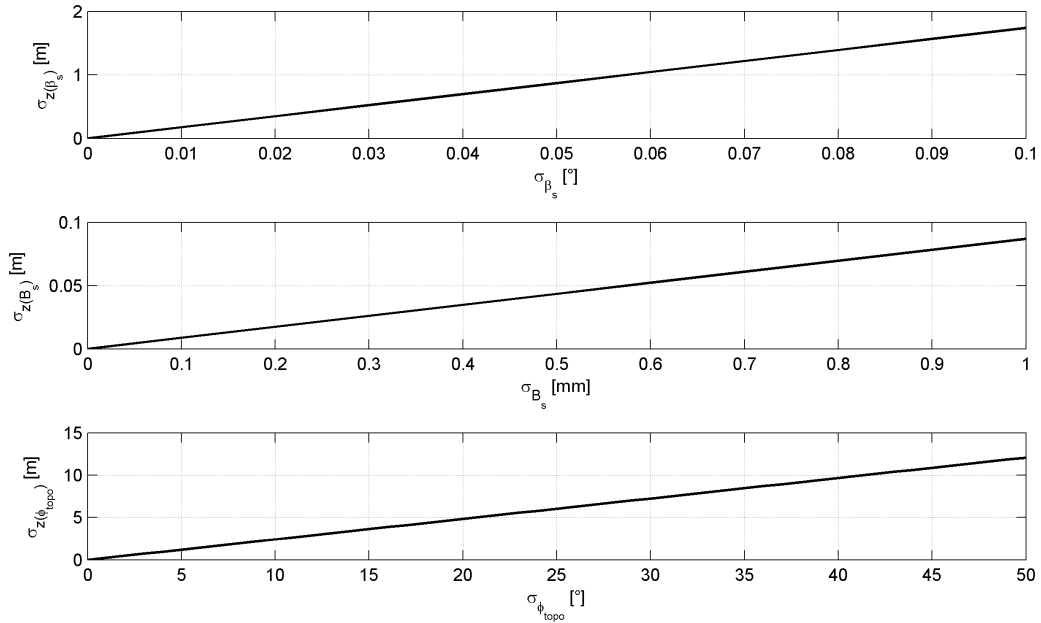


Figure 2.15: Standard deviation of height $z$ with respect to standard deviations of baseline angle $\sigma_{\beta_s}$, spatial baseline $\sigma_{B_s}$ and topographic phase $\sigma_{\phi_{topo}}$ for a vertical spatial baseline of 0.1 m and a topographic phase of $2\pi$. The total standard deviation $\sigma_z$ can be computed by applying the error propagation law: $\sigma_z^2 = \sigma_{z(\beta_s)}^2 + \sigma_{z(B_s)}^2 + \sigma_{z(\phi_{topo})}^2$. Please note the different scaling of the axes.

### 2.2.3 Displacement

Displacements can be measured in form of relative changes in distance between target and sensor. Thus, only one component in Line Of Sight (LOS) $d$ of a three dimensional displacement vector $\mathbf{d}_{xyz}$ can be observed. The relation between displacement and interferometric phase $\phi_{disp}$ is given by

$$\phi_{disp} = \frac{4\pi}{\lambda}d = \frac{4\pi}{\lambda} \cdot \mathbf{d}_{xyz} \cdot \mathbf{s}, \tag{2.37}$$

whereas $\mathbf{s}$ is the unit vector of the LOS direction.

The standard deviation of displacement is linked to the standard deviation of phase measurement simply by

$$\sigma_d = \frac{\lambda}{4\pi}\sigma_{\phi_{disp}}. \tag{2.38}$$

For Ku-band radar ($\lambda = 17.4$ mm) and a phase standard deviation of $\sigma_{\phi_{disp}} = 20°$, the standard deviation of displacement measurement is $\sigma_d = 0.5$ mm. The smaller the wavelength $\lambda$, the better is the standard deviation for displacement $\sigma_d$ but the phase unwrapping will become more difficult as the unambiguous displacement (see equation 2.24) decreases as well.

### 2.2.4 Signal to Noise Ratio and Coherence

The observed wrapped phase $\phi^w$ is disturbed by noise. The Signal to Noise Ratio (SNR) is the relation between received power and noise (e.g. Massonnet and Souyris, 2008). Noise is composed of system noise (e.g. thermal noise) and environmental noise caused by changes of the target properties (e.g. dielectric constant) and atmosphere (e.g. rain). The thermal SNR of point targets is defined as

$$SNR^{thermal} = \frac{P_r}{P_n} \cdot G_r \cdot G_c \qquad \text{or} \qquad SNR^{thermal}_{[dB]} = 10 \cdot (\log P_r - \log P_n + \log G_r + \log G_c), \tag{2.39}$$

where $P_r$ is the received power and $P_n$ is thermal noise (personal communication, IDS). Due to the SAR focusing, the SNR is improved by $G_r = n_r$, the number of independent range observations and $G_c = n_c$, the number of independent cross-range observations. In practice, the SNR including environmental noise can be estimated from the observed amplitude variation of a time series of each pixel (Adam et al., 2004; Ferretti et al., 2001):

$$S\hat{N}R = \frac{m_a^2}{2\sigma_a^2} \qquad \text{or} \qquad S\hat{N}R_{[dB]} = 20 \cdot (\log m_a - \log \sigma_a) - 3 \text{ dB}, \tag{2.40}$$

with $m_a$ being the mean amplitude and $\sigma_a$ the standard deviation of amplitude.

Another parameter to assess the quality of an interferogram $z_1 z_2^*$ is coherence (e.g. Bamler and Hartl, 1998). Coherence $\gamma$ is defined by

$$|\gamma| = \left| \frac{E\{z_1 z_2^*\}}{\sqrt{E\{|z_1|^2\} E\{|z_2|^2\}}} \right|, \qquad 0 \le |\gamma| \le 1, \tag{2.41}$$

with $E\{\cdot\}$ being the mathematical expectation. A coherence of $\gamma = 1$ means perfect coherence (i.e. the interaction of radar wave with the target is equal in both images that form the interferogram) while $\gamma = 0$ means no coherence. The relation between coherence and SNR is given by (Hanssen, 2002)

$$|\gamma| = \frac{SNR}{SNR + 1}. \tag{2.42}$$

Expressed in logarithmic scale, a SNR of 0 dB equals a coherence of $\gamma = 0.5$. Theoretically, a coherence of $\gamma = 1.0$ implies an infinite SNR. In appendix section A.3 a table is given for the conversion of SNR and coherence.

The coherence is influenced by a variety of factors and thus the total coherence of a interferogram pixel can be expressed as

$$\gamma = \gamma^{thermal}\gamma^{spatial}\gamma^{temporal}. \tag{2.43}$$

The thermal coherence is directly related to the thermal noise by equation 2.42. In case of zero-baseline observations, the spatial coherence is 1. The temporal coherence depends on environmental conditions and is generally decreasing with increasing temporal baseline. Thus, the temporal baseline should be as short as possible to avoid temporal decorrelation (i.e. loss of coherence with time).

 In practise, the coherence can be estimated for each pixel by obtaining the expected values in equation 2.41 by a 2D moving average of $n$ observations (Hanssen, 2002; Bamler and Hartl, 1998):

$$|\hat{\gamma}| = \left| \frac{\sum_{i=1}^{n}(z_1 z_2^*)}{\sqrt{\sum_{i=1}^{n} |z_1|^2 \sum_{i=1}^{n} |z_2|^2}} \right| \tag{2.44}$$

### 2.2.5 Statistics of Phase Observation

The interferometric phase $\phi$ of a distributed target can by described by the Probability Density Function (PDF) (Hanssen, 2002; Just and Bamler, 1994)

$$\text{pdf}(\phi; \gamma, \phi_0) = \frac{1 - |\gamma|^2}{2\pi} \frac{1}{1 - \beta^2} \left( \frac{\beta \arccos(-\beta)}{\sqrt{1 - \beta^2} + 1} \right), \tag{2.45}$$

with $\beta = |\gamma| \cos(\phi - \phi_0)$, $\phi_0 = E\{\phi\}$. For total decorrelation ($|\gamma| = 0$), the PDF of $\phi$ becomes a uniform distribution and for total coherence ($|\gamma| = 1$), it becomes a Dirac delta function (see Figure 2.16).
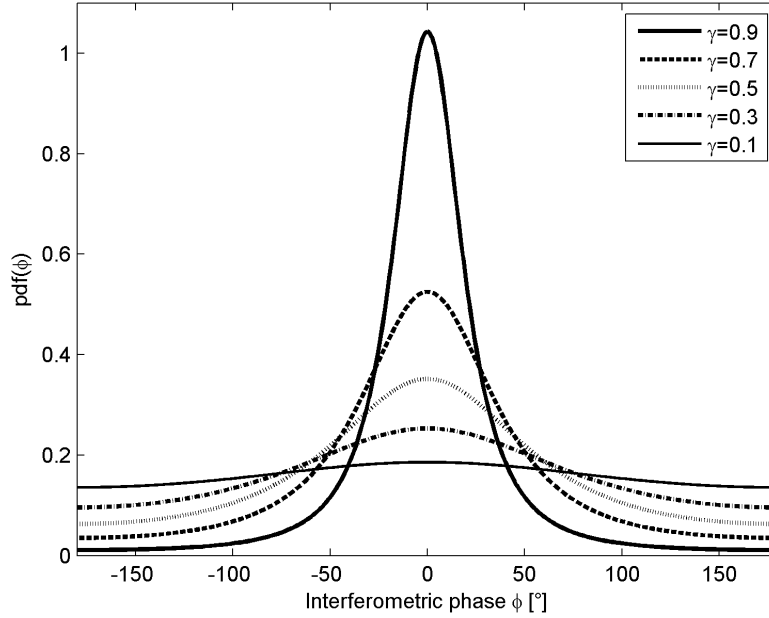


Figure 2.16: Probability density function of interferometric phase $\phi$ for different coherence levels.

 The phase variance of distributed targets can be obtained by computing the second momentum of equation 2.45 (Hanssen, 2002; Just and Bamler, 1994)

$$\sigma_\phi^2 = \frac{\pi^2}{3} - \pi \arcsin(|\gamma|) + \arcsin^2(|\gamma|) - \frac{Li_2(|\gamma|^2)}{2}, \tag{2.46}$$

with the Euler dilogarithm $Li_2(|\gamma|^2) = \sum_{k=1}^{\infty} |\gamma|^{2k}/k^2$.

 Targets with high SNR can be regarded as point targets dominated by one scatterer with high amplitude. In this case, the phase variance determined by equation 2.46 is overestimated and the variance can be determined by (Hanssen, 2002; Just and Bamler, 1994)

$$\sigma_\phi^2 = \frac{1 - \gamma^2}{2\gamma^2}. \tag{2.47}$$

Figure 2.17 shows a plot of interferometric phase standard deviation of point targets and distributed targets versus coherence.

 To estimate the phase standard deviation from SAR observations, properties of the amplitude time series can be related to the phase standard deviation. For targets where $\sigma_\phi$ is small, i.e. targets with a high SNR, the phase variance can be approximated by

$$\hat{\sigma}_\phi = \frac{\sigma_a}{m_a} = \frac{1}{2S\hat{N}R}, \tag{2.48}$$

whereas $m_a$ and $\sigma_a$ are mean and standard deviation of the amplitude, respectively (Ferretti et al., 2001).

Figure 2.17: Relation of interferometric phase standard deviation of point targets and distributed targets with coherence.
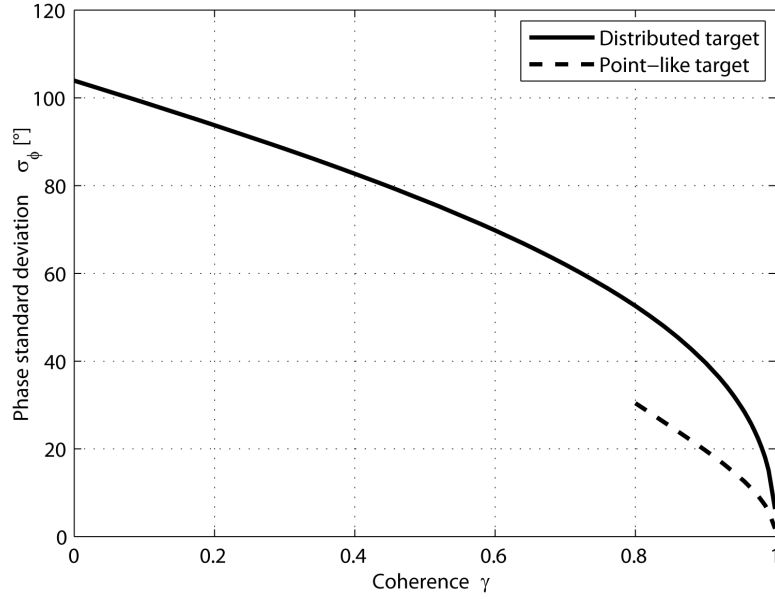
## 2.3 IBIS-L

IBIS-L stands for Image By Interferometric Survey and is a GB-SAR developed by IDS (Ingegneria dei Sistemi S.p.A., Pisa). Two different IBIS versions exist: IBIS-S, specifically developed for the monitoring of engineering structures and IBIS-L, specifically developed for the monitoring of landslides and related objects. In contrary to IBIS-L, IBIS-S is no GB-SAR. The radar sensor with transmitting and receiving antennas is mounted on a tripod. By that, only range resolution is obtained but a higher sampling rate is possible (up to 200 Hz). Thus, the applications of IBIS-S are mainly

- Monitoring of man made structures as bridges, towers, buildings, etc.;
- Determination of eigenfrequencies and eigenmodes of structures.

Applications of IBIS-L can be summarized as

- Monitoring of large-scale man made structures as buildings, dams, etc. (Alba et al., 2008);
- Monitoring of mining activities, subsidence, etc;
- Monitoring of natural hazards as landslides, glaciers, volcanoes (Tarchi et al., 2003; Noferini et al., 2006);
- Snow cover and avalanche monitoring (Martinez-Vazquez and Fortuny-Guash, 2006);
- Generation of Digital Elevation Model (Pieraccini et al., 2001; Rödelsperger et al., 2010a).

Detailed descriptions and application examples on IBIS-S and IBIS-L can be found in Rödelsperger et al. (2010b,c). This work is only concerned with the GB-SAR IBIS-L. The synthetic aperture is realized by moving the sensor along a rail. The radar head is equal in both IBIS versions, only the mounting is different. Figure 2.18 shows a photo of IBIS-L installed on a concrete basement. In the following, the configuration of IBIS-L used in this work is presented. Generally, the instrument can be operated in other configurations.

The total length of the rail is 2.5 m with an effective path length of 2 m for the movement of the sled. The rail can be mounted on a concrete basement or solid rock by thread rods. A reference sphere and a positioning fork ensure the accurate repositioning of the instrument in case of discontinuous measurements.

The sensor head is mounted on a sled, which can be moved along the rail. Two pyramidal horn antennas with a gain of 20 dB transmit and receive vertical polarized radar waves with a frequency of 17.2 GHz. The −3 dB beamwidth is 17° horizontal by 15° vertical. The sensor can be tilted along the antenna axis to direct the antenna beam to the object under observation.

The power supply unit contains two batteries (each 12 V, 70 Ah) which can supply the instrument for 24 h. External power can either be provided by AC mains power, a generator or solar modules.

The instrument is controlled by a PC via USB interface and the IBIS Controller software operating under Windows. After starting the acquisition, the software automatically repeats the measurements with a given delay
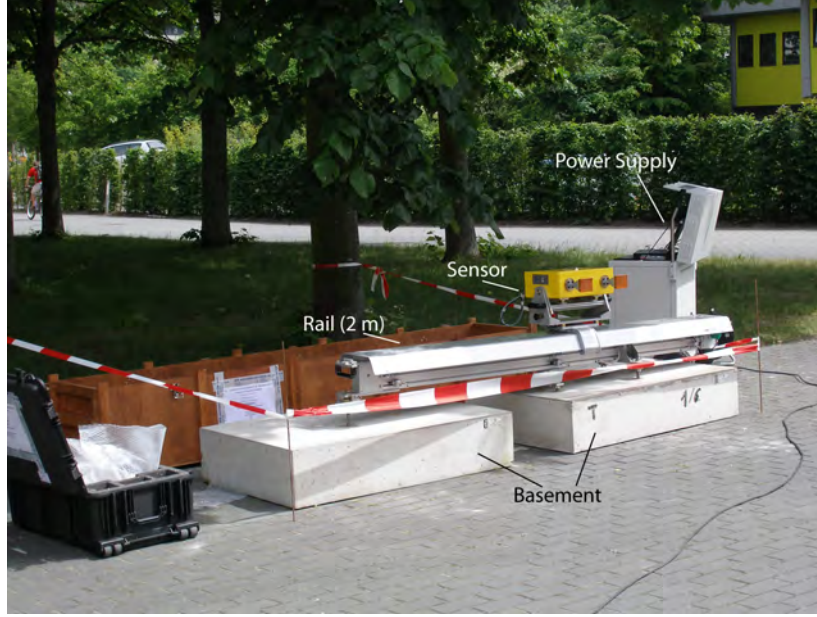
Figure 2.18: Photo of IBIS-L.

time. The generation of one radar image with range and cross-range resolution takes 5 to 10 min (depending on the maximum range). The raw data (unfocused) is stored on the PC as file with the extension *gbd* (one file per acquisition). The file size depends on the chosen resolution and maximum range. With full resolution (0.75 m in range by 4.4 mrad in cross-range), the file size is about 32 MB for a distance of 4 km. The file size of the focused image (extension *gbf*) is half the size of a raw image file.

A summary of the instrument specifications is listed in Table 2.3.

| Parameter | Value |
|---|---|
| Central frequency $f$ | 17.2 GHz |
| Central wavelength $\lambda$ | 17.44 mm |
| Bandwidth $B$ | 200 MHz |
| Scan length $L_s$ | 2 m |
| Scan time $\Delta t$ | $5 - 10$ min |
| Maximum distance $R_{max}$ | 4000 m |
| Range resolution $\delta_r$ | 0.75 m |
| Cross-range resolution $\delta_c$ | 4.4 mrad (4.4 m at 1000 m range) |

Table 2.3: IBIS-L specifications

### 2.3.1 Advantages and Disadvantages

The advantages (+) and disadvantages (-) of IBIS-L versus spaceborne SAR can be summarized as follows:

+ Zero-baseline: A major advantage of IBIS-L versus spaceborne SAR is the full control of spatial baseline. For displacement monitoring, the zero-baseline interferometry is best because no DEM is necessary to retrieve displacements.

+ Accurate "orbit" control: The position of the rail can be determined and monitored accurately and thus interferograms by IBIS-L are free of orbit-errors.

+ High sampling rate: The sampling interval of IBIS-L is 5 to 10 minutes while the revisit time of spaceborne SAR is usually several days. The high sampling rate simplifies the phase unwrapping considerably.

– Limitation to local monitoring: Spaceborne SAR can monitor a large area at any place on Earth, while IBIS-L is limited to a certain location. The installation time of IBIS-L depends on the infrastructure available (e.g. basement, power supply, instrument shipment) and access.

+/– Incidence angle: Depending on the object to be monitored, either spaceborne SAR or GB-SAR may have
    an advantage: e.g. for monitoring subsidences, spaceborne SAR has a optimal view angle; for monitoring
    steep slopes, GB-SAR is better suited.

The advantages and disadvantages of IBIS-L versus conventional monitoring techniques (e.g. tiltmeter, exten-
someter, GPS, tachymeter, laser scanner) can be summarized as follows:

+ Remote sensing instrument: The remote sensing capability is clearly an advantage over a variety of common
  monitoring equipments which necessitate access to the monitored structure. Especially when monitoring
  natural hazards (e.g. landslides, volcanoes), entering the endangered zone is often impossible. With a
  maximum distance of 4 km, even inaccessible parts of a structure as large towers, dams or landslides can
  be monitored.

+ Independence of daylight and weather: Due to the use of radar waves, the monitoring can continue during
  night and when visibility is limited due to fog, clouds or rain.

+ Simultaneous monitoring of all targets within the beam with high accuracy and spatial resolution: Most
  monitoring equipment is limited to either high accuracy or high spatial resolution while IBIS-L provides
  both. Due to cost limitations, it is often not possible to cover the whole structure with high-accuracy
  instrumentation while IBIS-L can monitor the surface displacements at all targets within the antenna
  beam simultaneously with an accuracy of 0.1 to 1 mm depending on distance to the target and target
  conditions.

+ Undisturbed by passing objects: If in case of a laser scanner or tachymeter a person is passing by and
  covers the direct line of sight for a short time period, some measurements at distinct points are lost. In
  case of IBIS-L short disturbances do not matter due to the sampling being done in the frequency domain.

– Accuracy depends on target reflectivity: Slopes and surfaces entirely covered with vegetation or structures
  without well reflecting points cannot be monitored without additional artificial reflectors. At Ku-band,
  the radar waves do not penetrate ground vegetation and mainly the vegetation surface is observed, which
  leads to a loss of coherence. The installation of passive radar reflectors however requires access to the
  structure.

– Atmospheric delay: The most limiting factor for accuracy is the atmosphere. In long-term monitoring
  the atmospheric delay has to be corrected which makes either additional weather sensors and/or stable
  targets in the monitored area necessary.

– LOS displacements: The monitoring of displacements is limited to one-dimensional displacements. Thus,
  some knowledge or assumptions must exist if horizontal or vertical displacements shall be derived from
  the LOS displacements.

– Ambiguous displacements: Since no absolute phase is determined, the obtained displacement is ambiguous.
  The ambiguities can only be determined with certain assumptions, e.g. that the movement is below $\lambda/4$
  per image.

– Difficult point localization: The point localization in radar images is more difficult than in other areal
  observation techniques as e.g. laser scanning. To map the radar image into a global reference system,
  a DEM is necessary. Targets at equal distance and azimuth but with different heights are mapped to
  the same resolution cell. If the monitored structure has a complex appearance, this can become a major
  problem as different displacement behaviours of two targets might be indistinguishable. This effect can
  be compensated by choosing the position of the instrument carefully.

### 2.3.2 Monitoring Requirements and Concepts

How suitable a structure or slope is for monitoring its displacements with IBIS-L depends on object properties as
e.g. expected displacement rate, object dimension and appearance. The maximum unambiguous displacement
rate of a target follows from equation 2.24 and is limited by wavelength $\lambda$ and sampling rate $\Delta t$

$$|v_{max}| = \frac{\lambda}{4\Delta t}. \tag{2.49}$$

For wavelengths between Ku- and L-band, the maximum unambiguous velocity is between 0.6 m/day and
10 m/day at a 10 min sampling interval. Using the velocity scale for landslides of IUGS-WGL (1995), landslides
between class 1 (extremely slow) and class 4 (moderate) can be monitored unambiguously. Table 2.4 shows the
time until the displacement of $\Delta r = \lambda/4$ is reached for wavelengths between Ku and L-band. If this time is below
the sampling interval, the phase ambiguities cannot be resolved without additional information or assumptions.
If this time exceeds several months and no increase of velocity is expected, a continuous monitoring is not

reasonable. In such a case, monitoring campaigns of several days with time spans of several months in-between the campaigns are more efficient. It has to be made sure that the instrument can be reinstalled accurately to avoid spatial decorrelation. Further information on discontinuous measurements with GB-SAR can be found in Noferini et al. (2008b) and Pieraccini et al. (2006). This thesis deals with continuous monitoring campaigns.

| Velocity [mm/d] | Class | Time to reach $\Delta r = \lambda/4$ | | |
| --- | --- | --- | --- | --- |
| | | **Ku-band** ($\lambda = 17$ mm) | **C-band** ($\lambda = 56$ mm) | **L-band** ($\lambda = 235$ mm) |
| 10000 | 4 | 0.6 min | 2 min | 8 min |
| 2000 | 4 | 3 min | 10 min | 42 min |
| 400 | 3 | 15 min | 50 min | 3.5 h |
| 80 | 3 | 1.2 h | 4 h | 18 h |
| 16 | 3 | 6 h | 21 h | 3.7 d |
| 3.2 | 2 | 1.3 d | 4.4 d | 18 d |
| 0.6 | 2 | 7 d | 23 d | 98 d |
| 0.1 | 2 | 43 d | 140 d | 1.6 y |
| 0.03 | 1 | 142 d | 1.3 y | 5 y |

Table 2.4: Time to reach a displacement of $\Delta r = \lambda/4$ with wavelengths between Ku and L-band for different object velocities.

The maximum dimension of the object to be monitored is restricted by the distance of the instrument and the beam width. The beam width of IBIS-L depends on the used antenna. In this work, an antenna with horizontal $-3$ dB beam width of $17°$ was used. This results in maximum horizontal dimension of about 300 m at a distance of 1000 m and accordingly a horizontal dimension of about 1200 m at a distance of 4000 m. The maximum object dimension is a smooth boundary and also depends on the object reflectivity. A good reflecting target may still be monitored with high accuracy outside the main beam but the SNR is dropping rapidly with increasing azimuth. Generally, IBIS-L can be operated with different antennas but it must be considered that a wider main beam results in a lower SNR.

A key to successful monitoring is the selection of the installation side which must fulfill certain requirements:

- The most important requirement is the stability, i.e. the instrument must not move during the measurements.
- In case of hazard monitoring, the safety of the instrument must be assured. The instrument should not be mounted in the endangered zone.
- The expected displacements must be considered as only LOS displacements can be observed. The instrument should positioned such that the line of sight coincides as best as possible with the expected direction of displacement.
- The choice of the incidence angle is a trade off between ground range resolution and power of the backscattered signal. For decreasing incidence angles, the ground range resolution is improving but the power of backscattered signal is decreasing (see also Figure 2.9 and section 2.1.4).
- Overlays (i.e. targets at different heights that are mapped into one image pixel) should be avoided because the displacement signal of the individual targets cannot be reconstructed.

In the following section, the state of the art of data post processing is presented. In chapter 4, a real-time approach is described.

# 3 Analysis of GB-SAR Data

In last chapter, the properties of GB-SAR images and interferograms were described. From now on, when talking about GB-SAR, it is assumed that the spatial baseline is zero, as this is usually the case for displacement monitoring applications. As illustrated in section 2.2, the observed interferometric phase is wrapped into the interval $[-\pi, \pi)$ and is a sum of several effects (displacement, atmosphere and noise). The goal of data analysis is the phase unwrapping, i.e. the determination of phase ambiguities to retrieve the absolute interferometric phase, and the separation of the different effects. In the following sections, the state of the art of relevant techniques for processing and analysing SAR data for displacement monitoring applications is described. A brief summary of phase unwrapping methods is given in section 3.1.

The conventional InSAR analysis is based on the processing and analysis of interferograms. The different steps necessary to retrieve geocoded displacement maps out of a set of raw images are described in section 3.2.

In spaceborne SAR, the conventional InSAR analysis suffers from temporal and spatial decorrelation. Temporal decorrelation (i.e. loss of coherence with time) increases with temporal baseline and is worst in vegetated areas. Spatial decorrelation increases with spatial baseline. Thus, only a limited number of interferograms is usable and the analysis is limited to high coherent areas. Especially in densely vegetated areas, the conventional analysis fails whereas, even if within decorrelated areas, single targets with good coherence may exist.

As a result, the Permanent Scatterers Technique was developed and patented by A. Ferretti, C. Prati and F. Rocca (EU patent 1 183 551 B1) to overcome these difficulties (Ferretti et al., 2000, 2001). The technique selects so-called permanent scatterers (i.e. pixels with high coherence) and performs an estimation of displacement, topography and atmospheric delay using the phase time series. Diverse algorithms exist, similar to the Permanent Scatterers Technique, which are all summarized by the term Persistent Scatterer Interferometry (PSI) (Kampes, 2006). A short summary of the Permanent Scatterers Technique, as well as other PSI algorithms, is given in section 3.3.

## 3.1 Phase Unwrapping

Phase unwrapping is an essential part of all analysis techniques. The interferometric phase $\phi^w$ is wrapped into the interval $[-\pi, \pi)$ and related to the true phase $\phi$ by $\phi^w = \phi - 2\pi n$. The correct determination of phase ambiguity $n$ is the key to successful displacement monitoring and is called phase unwrapping. Generally, phase unwrapping is a three-dimensional problem (2D spatial and 1D temporal).

Many papers on all kinds of unwrapping methods exist for 1D up to 3D unwrapping techniques (Itoh, 1982; Goldstein et al., 1988; Cusack et al., 1995; Ghiglia and Pritt, 1998; Huntley, 2001). The simplest method of unwrapping a sampled signal in 1D space is described by e.g. Itoh (1982). Considering a sequence of $m$ discrete wrapped phase measurements $[\varphi_1^w, \varphi_2^w, ..., \varphi_m^w]$, the unwrapped interferometric phase $\phi_k = \varphi_1 - \varphi_k$ can be obtained by summing all wrapped phase differences

$$
\begin{aligned}
\phi_k &= \mathcal{W}\left\{\varphi_1^w - \varphi_2^w\right\} + \mathcal{W}\left\{\varphi_2^w - \varphi_3^w\right\} + \cdots + \mathcal{W}\left\{\varphi_{k-1}^w - \varphi_k^w\right\} \\
&= \varphi_1^w - \varphi_2^w - 2\pi n_{12} + \varphi_2^w - \varphi_3^w - 2\pi n_{23} + \cdots + \varphi_{k-1}^w - \varphi_k^w - 2\pi n_{k-1,k} \\
&= \varphi_1^w - \varphi_k^w - 2\pi(n_{12} + n_{23} + \cdots + n_{k-1,k}).
\end{aligned}
\tag{3.1}
$$

This algorithm produced correct results as long as the sampling rate of the signal is high enough to detect phase jumps (i.e. the Nyquist criteria is satisfied) and noise is limited. In Figure 3.1, an example is given for 1D unwrapping. With a sampling rate of $\Delta t = 100$, the signal is undersampled and cannot be recovered without further assumptions on the original structure of the phase signal.

In 2D space, this undersampling leads to the unwrapped signal being path dependent when using path following methods, i.e. the result of unwrapping is dependent on the chosen path through the 2D image. The phase gradient between neighbouring pixels determines if an ambiguity is introduced: if the phase gradient exceeds $\pi$, one phase cycle is subtracted; if it is less then $\pi$, one phase cycle is added. One single "hole" within a fringe pattern may suffice for the path integration to slip through without detecting the phase jump and corrupt the whole image. To determine the path dependency, so-called residues of each pixel can be determined by summing the wrapped phase of $2 \times 2$ neighbouring pixels:

$$
r = \mathcal{W}\left\{\phi_{i+1,j} - \phi_{i,j}\right\} + \mathcal{W}\left\{\phi_{i+1,j+1} - \phi_{i+1,j}\right\} + \mathcal{W}\left\{\phi_{i,j+1} - \phi_{i+1,j+1}\right\} + \mathcal{W}\left\{\phi_{i,j} - \phi_{i,j+1}\right\}.
\tag{3.2}
$$

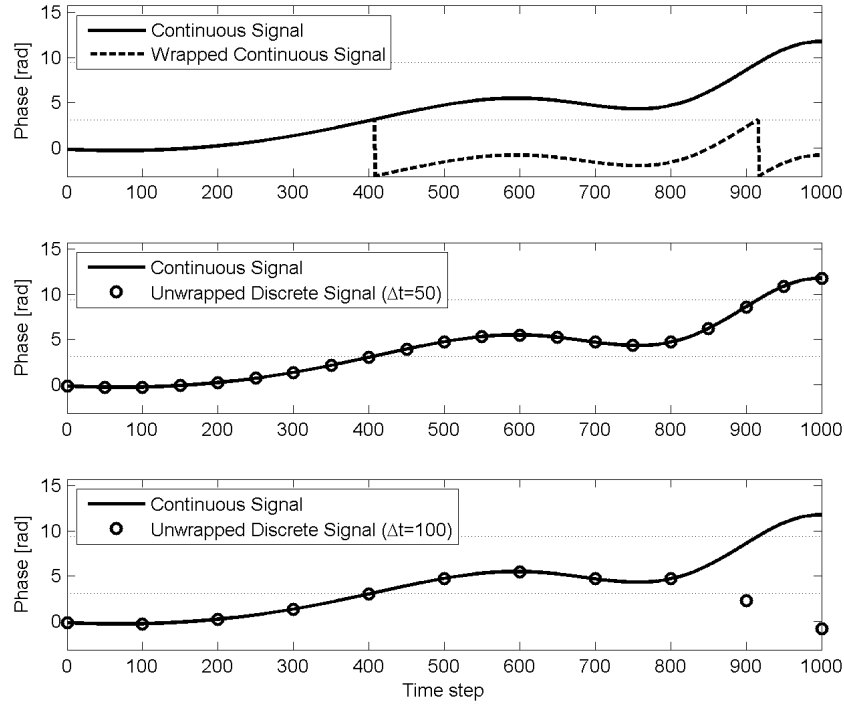A residue of $r = 2\pi$ or $r = -2\pi$ is an indication for inconsistency.

Figure 3.1: 1D phase unwrapping of a signal sampled with different sampling rates. With $\Delta t = 100$ the signal is undersampled and phase unwrapping produces wrong results.

Many different algorithms have been developed to deal with this problem as e.g. Goldstein's branch cut algorithm (Goldstein et al., 1988), Flynn's minimum discontinuity algorithm (Flynn, 1997) or Constantini's network flow algorithm (Constantini, 2002). Goldstein's branch cut algorithm introduces so-called branch-cuts connecting positive and negative residues in such a way that the total length of all branch cuts is minimized. The objective of the branch cuts is to prevent the path following integration from choosing this specific path.

The success rate of all unwrapping techniques depends strongly on the phase image quality. Unwrapping errors propagate through all pixels and time steps which makes the phase unwrapping to the most important and time intensive processing step.

## 3.2 Conventional InSAR Analysis

The basic concept of conventional InSAR analysis of GB-SAR images is similar to spaceborne SAR, whereas the processing chain of the latter is more complicated. Figure 3.2 gives an overview of the different steps necessary (e.g. Bamler and Hartl, 1998; Hanssen, 2002) for analysing GB-SAR images.
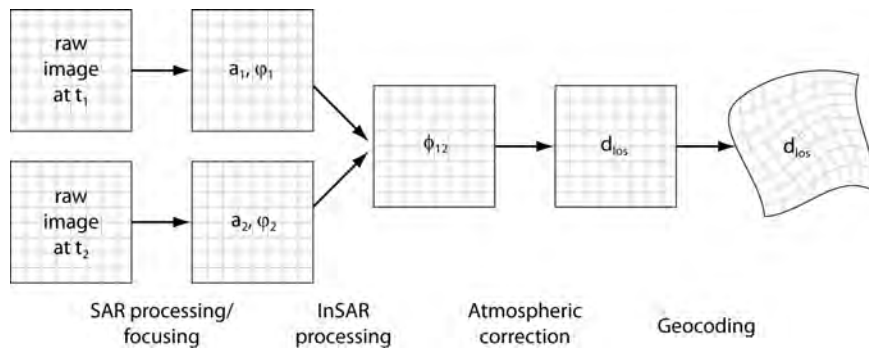


Figure 3.2: InSAR processing chain.

The processing chain can be divided into four major steps:

- SAR processing / focusing: The first step is the focusing, described in section 2.1.3. The result is a set of focused SAR images containing amplitude $a$ and phase $\varphi$.

- InSAR processing: The goal of InSAR processing is to form interferograms and retrieve the unwrapped interferometric phase $\phi$. In section 3.2.1, necessary steps are described and similarities and differences between spaceborne and GB-SAR are illustrated.

- Atmospheric correction: The unwrapped interferometric phase still contains contributions from displacement, atmosphere and noise. In section 3.2.2, several algorithms for removing the atmospheric effect are presented. Noise can be accounted for by spatial low pass filtering. The result of atmospheric correction and filtering is the unwrapped interferometric phase $\phi_{disp}$, which is related to the LOS displacements by $d = \frac{\lambda}{4\pi}\phi_{disp}$.

- Geocoding: To display the observed displacements in a global reference system and for comparing them with observations from other sources, geocoding is necessary. The relation between the local GB-SAR coordinate system and a global reference system is described in section 2.1.4.

### 3.2.1 InSAR processing

In GB-SAR, the formation of wrapped interferograms is simply done by selecting two images and applying equation 2.26. In spaceborne SAR, however, the interferogram formation is more complicated. The most important steps are the image selection and coregistration (Hanssen, 2002). Depending on the application, suitable SAR images must be selected. For displacement monitoring, the spatial baseline should be as short as possible to avoid spatial decorrelation and to minimize the topographic phase. Before generating interferograms, both images need to be coregistered to bring them into the same coordinate system. By applying equation 2.26 on the coregistered images, an interferogram can be formed.

Spaceborne SAR interferograms usually have a temporal and spatial baseline and thus, also contain topographic phase. The topographic phase can either be subtracted by using an external DEM or by using differential interferometry (DInSAR) where the DEM is determined from a second interferogram. By that, zero-baseline interferograms are simulated.

The resulting interferograms now contain the wrapped phase which, is a sum of displacement, atmospheric disturbances and noise. In case of spaceborne SAR, also a residual topographic phase may be included due to orbit and DEM errors. The amount of noise can be assessed by estimating the coherence using equation 2.44. Figure 3.3 shows coherence and wrapped phase of two interferograms with a temporal baseline of 9 min observed with IBIS-L in Bad Reichenhall, Germany in September 2008. The quality difference is obvious in coherence and interferometric phase image. The interferogram of images 14 and 15 appears much noisier.

The interferometric phase is still wrapped. Under the assumption that the temporal phase function is not undersampled, i.e. that in-between two consecutive images the absolute phase change is below the ambiguous phase change of $\pi$, an unwrapped absolute phase of a set of images can be computed by cumulating all consecutive wrapped interferograms, i.e. applying 1D temporal unwrapping based on Itoh (1982) (see section 3.1). An example is given in Figure 3.4. Figure 3.4a is the wrapped interferogram of image 770 and 840 observed in Bad Reichenhall. The wrapped interferometric phase $\phi_{770,840}^w$ is computed by subtracting and wrap the phase observation at image 770 and 840: $\phi_{770,840}^w = \mathcal{W}\{\varphi_{770}^w - \varphi_{840}^w\}$. A clear fringe pattern with a full phase cycle is visible, thus the phase needs to be unwrapped to determine the correct absolute phase. By computing the sum of all wrapped consecutive interferograms between image 770 and 840 (see equation 3.1), the absolute phase can be determined (see Figure 3.4b).

If the initial assumption, that the temporal phase function is not undersampled, is not true, this unwrapping method will produce wrong results. In that case the interferograms need to be spatially unwrapped as well, as described in section 3.1. As already stated, the success rate is strongly dependent on image quality. Due to the bad error propagation properties of phase unwrapping, noise will increase with every time step. One solution of this problem is to cancel images with high noise. However, even in extremely noisy interferograms, single scatterers with high coherence can be identified. By cancelling these interferograms completely, the phase information of these scatterers is lost.

### 3.2.2 Atmospheric Correction

The formed interferograms still contain atmospheric distortions. Three different ways of atmospheric correction are presented here:

- Determination of atmospheric effect through meteorological observations (temperature, humidity and pressure);

- Determination of atmospheric effect by estimation at stable targets (ground control points);

(a) Interferogram 104-105
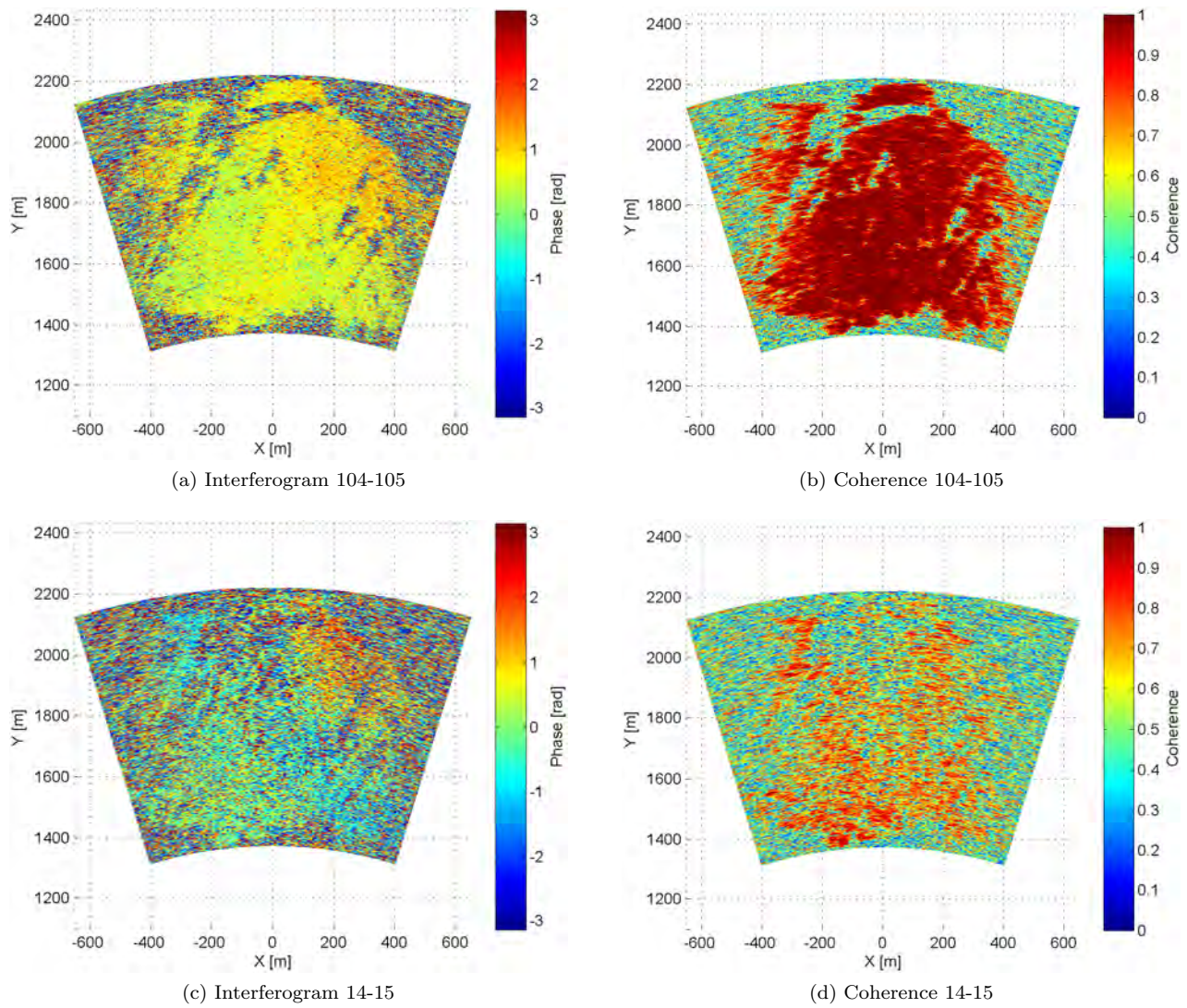
(b) Coherence 104-105

(c) Interferogram 14-15

(d) Coherence 14-15

Figure 3.3: Coherence and wrapped phase of two interferograms observed in Bad Reichenhall, September 2008.

(a) Wrapped interferogram 770-840
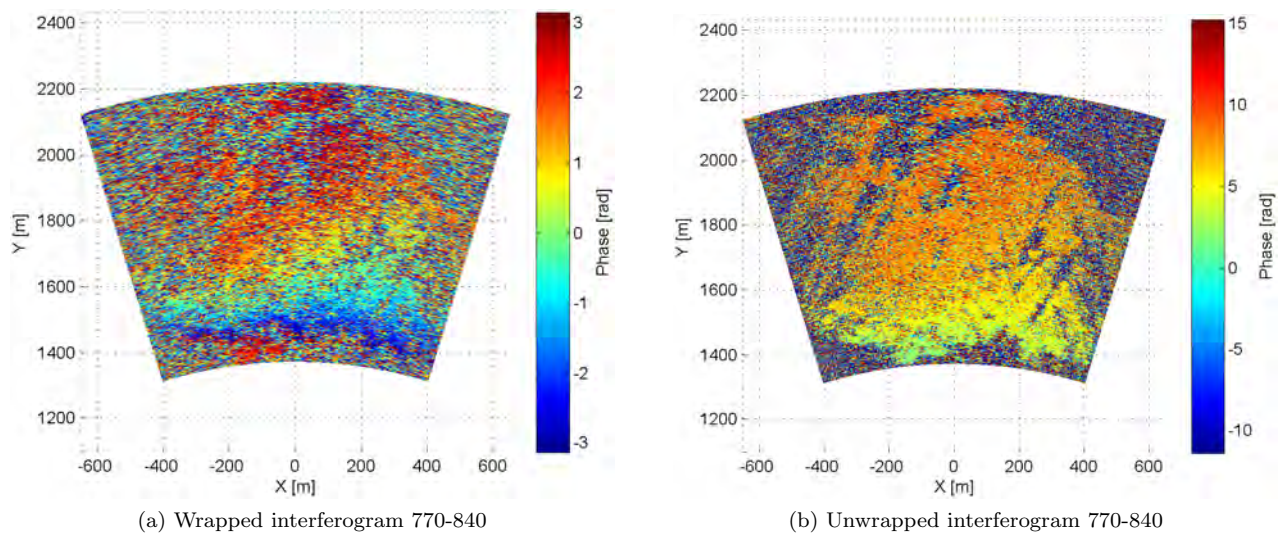
(b) Unwrapped interferogram 770-840

Figure 3.4: Wrapped and temporally unwrapped phase of interferogram of image 770 to 840 observed in Bad Reichenhall, September 2008.

- Spatial interpolation or filtering.

The relation between path delay and atmospheric parameters is given in equation 2.31. Assuming a uniform atmosphere (i.e. constant atmospheric parameters), the equation can be simplified to

$$\phi_{atm} = \frac{4\pi}{\lambda} ar \qquad \text{with} \qquad a = 7.76 \times 10^{-5} \frac{P}{T} + 3.73 \times 10^{-1} \frac{e}{T^2}, \qquad (3.3)$$

with $r$ being the distance between sensor and target. The achievable standard deviation of this approach was already discussed in section 2.2.1. The larger the distance between weather station and target, the larger will the errors be induced by the assumption of constant atmospheric conditions.

Instead of determining $a$ in equation 3.3 from observed weather data, it can be estimated for each time step using phase observations of stable targets (i.e targets with $\phi_{disp} = 0$) (e.g. Luzi et al., 2004; Noferini et al., 2005). For these stable targets equation 2.27 can be simplified to

$$\phi = \phi_{atm} + \phi_{noise}. \qquad (3.4)$$

Also higher order models can be used for modelling the variations of atmospheric properties along the path:

$$\phi_{atm} = \frac{4\pi}{\lambda} \sum_{i=0}^{m} a_i r^i, \qquad (3.5)$$

where $m$ is the polynomial degree. A drawback of these models is that the phase delay only depends on range. Atmospheric variations in cross-range are not modelled.

To overcome these limitations, two-dimensional interpolation or filtering methods can be applied (Crosetto et al., 2002; Meyer et al., 2005). The spatial low frequency component is regarded as atmospheric signal. The advantage is that this method can easily be adopted to work with wrapped phase data by filtering the real and imaginary part, $\cos\phi$ and $i\sin\phi$, respectively. The disadvantage of all methods using the GB-SAR data itself to determine the atmosphere is that they rely on the stable targets being correctly identified. If the selected scatterers are indeed not stable, the part of the low frequency component of the displacement signal will be regarded as atmosphere and discarded. Furthermore, it is important to have a number of stable targets distributed evenly throughout the interferogram. Otherwise the atmospheric signal may be biased in regions were less or no stable scatterers could be found.

Figures 3.5 and 3.6 show four correction techniques (weather data, polynom degree 1, polynom degree 2, spatial interpolation) applied on two different scenes. The interferogram shown in Figure 3.5a is a typical interferogram observed in a quarry in Dieburg, Germany with a maximum distance of about 300 m. In Figure 3.5b, the coherence and the selected stable targets are plotted. About 200 pixels were identified by thresholding on the coherence. They were used to estimate the atmospheric correction. The residuals for the different correction techniques can be seen in Figure 3.5c to 3.5f. The differences between the different atmospheric corrections is small. Only little improvement can be gained by spatial interpolation. The histogram in Figure 3.5h was created by analysing about 2000 pixels, which were again selected by thresholding on the coherence. The histograms of the residuals of all techniques are quite similar.

Figure 3.6 shows the same figures of interferograms observed at a mountain side in Bad Reichenhall. The maximum distance is about 2200 m. The radar instrument and weather sensor were positioned at a height of 650 m above sea level, while the furthest target is at about 1700 m height. Due to this, the correction using the weather data fails. The assumption of a uniform atmosphere is also not valid and non-linearities have to be accounted for. The best result can be obtained with spatial interpolation.

For both scenarios, 500 interferograms were corrected with the four techniques and the residuals at 2000 selected pixels were analyzed. Assuming that the displacements are zero at these pixels, the true value of the residuals is zero. Especially the correction using weather data has a systematic offset from this true value. Table 3.1 gives the mean and standard deviation of this bias as well as the standard deviation of the residuals.

## 3.3 Persistent Scatterer Interferometry

As stated previously, the classic InSAR processing approach suffers from temporal and spatial decorrelation as well as from atmospheric distortions. Nevertheless, even in noisy interferograms, single high coherent scatterers may exist and their valuable phase information may be lost in conventional InSAR processing. As a result, the Permanent Scatterers Technique was developed and patented by A. Ferretti, C. Prati and F. Rocca (EU patent 1 183 551 B1) exploiting all available phase information of these high coherent scatterers (i.e. permanent

(a) Wrapped interferogram


(b) Coherence


(c) Correction applied (weather data)


(d) Correction applied (polynom degree 1)


(e) Correction applied (polynom degree 2)


(f) Correction applied (spatial interpolation)


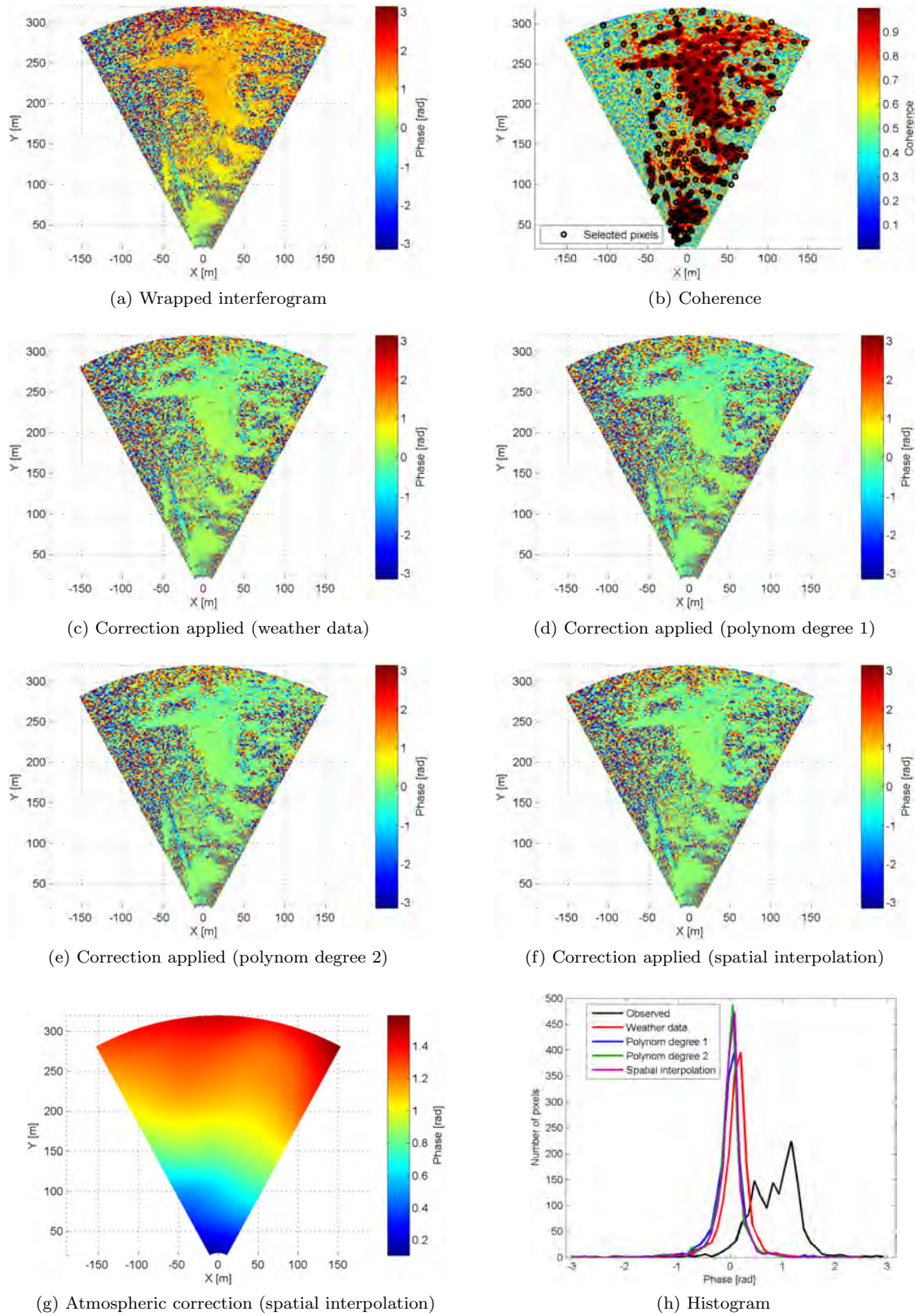(g) Atmospheric correction (spatial interpolation)


(h) Histogram

Figure 3.5: Figures (a) and (b) are the wrapped interferogram and coherence of images 102 and 112 observed with IBIS-L in Dieburg. Figures (c) to (f) are the same interferograms with different atmospheric corrections applied. The selected pixels in figure (b) are used for the estimation of the atmospheric signal. Figure (g) is the estimated atmospheric correction applied to figure (f) and figure (h) is a histogram of the corrected phase.

(a) Wrapped interferogram



(b) Coherence



(c) Correction applied (weather data)



(d) Correction applied (polynom degree 1)



(e) Correction applied (polynom degree 2)



(f) Correction applied (spatial interpolation)



(g) Atmospheric correction (spatial interpolation)
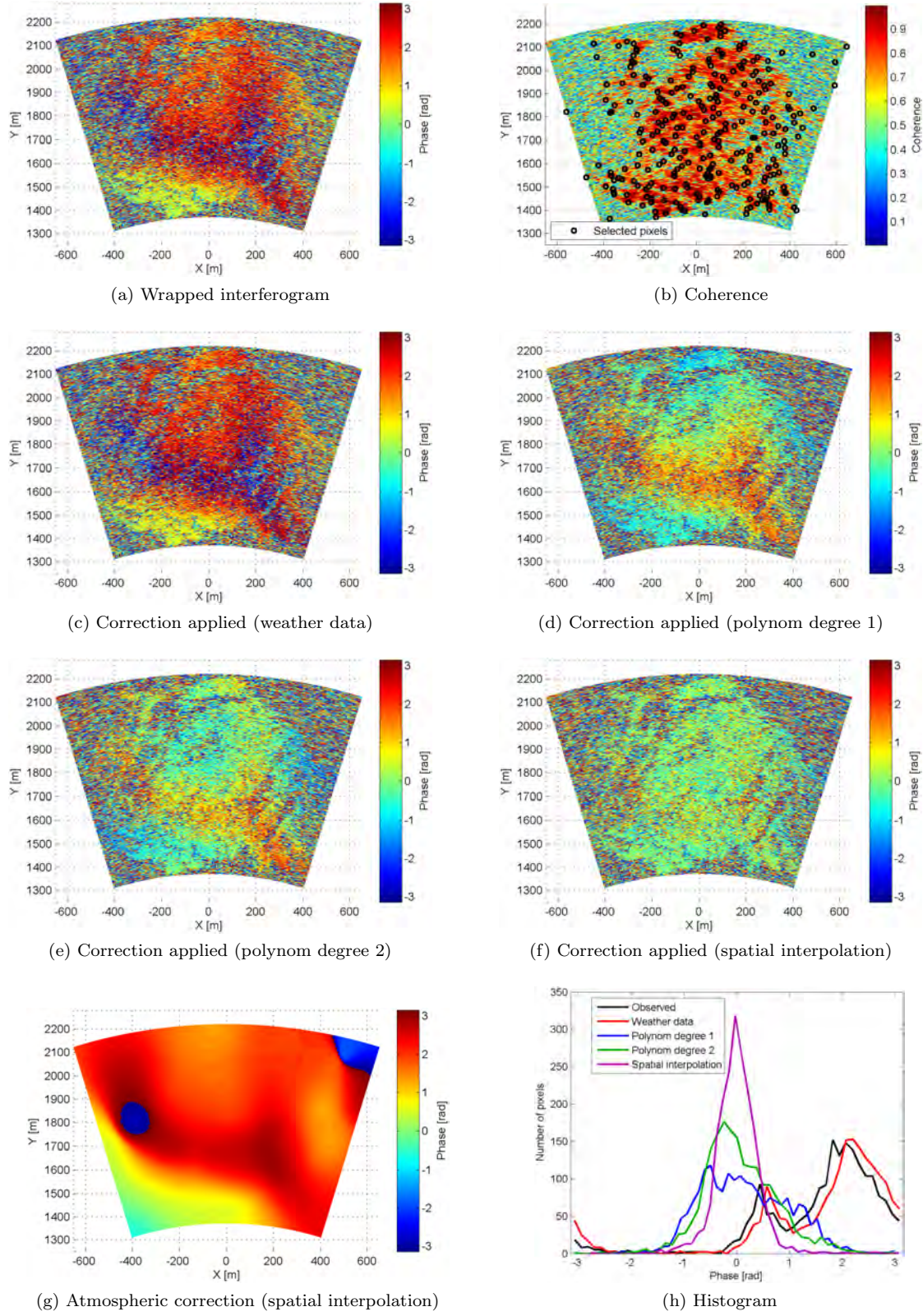


(h) Histogram

Figure 3.6: Figures (a) and (b) are the wrapped interferogram and coherence of images 520 and 521 observed with IBIS-L in Bad Reichenhall. Figures (c) to (f) are the same interferograms with different atmospheric corrections applied. The selected pixels in figure (b) are used for the estimation of the atmospheric signal. Figure (g) is the estimated atmospheric correction applied to figure (f) and figure (h) is a histogram of the corrected phase.

|  | Dieburg | | | Bad Reichenhall | | |
|---|---|---|---|---|---|---|
|  | $m_{bias}$ [rad] | $\sigma_{bias}$ [rad] | $\sigma_{res}$ [rad] | $m_{bias}$ [rad] | $\sigma_{bias}$ [rad] | $\sigma_{res}$ [rad] |
| **Weather data** | -0.0027 | 0.126 | 0.33 | -0.0197 | 1.060 | 0.50 |
| **Polynom degree 1** | -0.0033 | 0.018 | 0.32 | 0.0116 | 0.161 | 0.48 |
| **Polynom degree 2** | -0.0031 | 0.018 | 0.32 | 0.0090 | 0.153 | 0.47 |
| **Spatial interpolation** | -0.0008 | 0.016 | 0.32 | 0.0057 | 0.071 | 0.43 |

Table 3.1: Accuracy of different atmospheric correction techniques. $m_{bias}$ and $\sigma_{bias}$ are mean and standard deviation of the bias of the residues and $\sigma_{res}$ is the standard deviation of the residues.

scatterers) (Ferretti et al., 2000, 2001). In section 3.3.1, the basic principles of the Permanent Scatterers Technique are described.

Shortly after, a number of techniques have been developed using similar approaches as the Permanent Scatterers Technique summarized by the term Persistent Scatterer Interferometry (PSI) (Kampes, 2006). The basic idea of all PSI methods is the same: instead of analyzing interferograms, they estimate displacement rate, topography, atmosphere, orbit error and other parameters using the phase time series at selected permanent/persistent scatterers. The difference of the diverse algorithms lies mainly in the used assumptions, estimation methods and implementation. Exemplary, the Stanford Method for Persistent Scatterers (StaMPS) and the Delft PS-InSAR Processing Package (DePSI) and their differences with respect to the Permanent Scatterers Technique are described shortly.

Although the conditions for GB-SAR are much better than for spaceborne SAR (short temporal baseline, no spatial baseline), the conventional InSAR processing approach still suffers from temporal decorrelation and atmospheric artefacts. Thus, PSI techniques can increase the quality and reliability of the results. Since the conditions for GB-SAR differ somewhat from spaceborne SAR, the developed PSI techniques cannot be directly applied. In the next chapter, the assumptions of the reviewed PSI techniques are compared to the requirements and conditions of GB-SAR observations and a real-time approach for PSI is described.

### 3.3.1 Permanent Scatterers Technique

The main steps of the Permanent Scatterers Technique for spaceborne SAR are illustrated in the following (Ferretti et al., 2000, 2001; Kampes, 2006). One master image is selected and interferograms are formed with respect to this master image. By means of a DEM, differential interferograms are formed, which simulate zero-baseline interferograms. Due to orbit and DEM errors, these interferograms still contain a residual topographic phase.

The technique distinguishes between Permanent Scatterers (PSs) and Permanent Scatterer Candidates (PSCs), whereas the latter are used to estimate the Atmospheric Phase Screen (APS). The PSC are selected by analyzing the amplitude time series and thresholding on the Amplitude Dispersion Index (ADI) $D_a$, which equals the phase standard deviation for targets with high coherence (see equation 2.48)

$$D_a = \hat{\sigma}_\phi = \frac{\sigma_a}{m_a}, \tag{3.6}$$

whereas $m_a$ and $\sigma_a$ are mean and standard deviation of the amplitude. For estimation of the different signal contributions, the phase differences $\psi_{ij}^w = \mathcal{W}\left\{\phi_j^w - \phi_i^w\right\}$ at all neighbouring PSCs $(i, j)$ (i.e. double differenced phase observations) within a certain radius are formed. The unwrapped phase difference is the sum of the residual topographic phase, atmospheric artefacts, displacement and noise

$$\psi = \psi_{topo} + \psi_{disp} + \psi_{atm} + \psi_{noise}. \tag{3.7}$$

The phase model can be divided into a deterministic and stochastic part. The deterministic part models the residual topographic phase and linear displacement ($\psi_{lin} = \psi_{topo} + \psi_{lindisp}$) whereas $\psi_{topo}$ is a linear function of spatial baseline and $\psi_{lindisp}$ a linear function of time. The stochastic part contains the contributions from atmosphere, non-linear displacement and noise ($\psi_{nonlin} = \psi_{atm} + \psi_{nonlindisp} + \psi_{noise}$). The standard deviation of $\psi_{nonlin}$ is expected to be small due to the fact that the selected PSs have a high coherence (i.e. $\psi_{noise}$ is small) and that the phase difference between neighbouring pixels due to atmosphere ($\psi_{atm}$) and nonlinear motion ($\psi_{nonlindisp}$) will be rather small, assuming a spatial correlation of displacement and atmosphere.

With these assumptions, $\psi_{topo}$ and $\psi_{lindisp}$ can be determined from the wrapped data by means of spectral analysis of the two-dimensional complex signal representation. Since $|\psi_{nonlin}| < \pi$, the unwrapped phase

difference $\psi$ can directly be determined. If all estimations were correct, the interferometric phase $\phi$ at each PS could be directly computed with respect to a reference PS. Since this assumption is usually not correct, a weighted least-square integration algorithm is used whereas the weights are computed from the residual phase $\psi_{nonlin}$. For estimating the APS, the spatio-temporal correlation characteristic of the atmospheric distortions is exploited, i.e. that atmospheric artefacts are a spatially low frequency signal and uncorrelated in time. Atmospheric artefacts can be considered uncorrelated in time because of the low sampling rate of spaceborne SAR. In two consecutive acquisitions the atmospheric properties are totally different. Thus, the APS can be determined by temporal high pass and spatial low pass filtering $\psi_{nonlin}$. After the APS is estimated, more PSs can be identified by analysing the phase time series and the estimates for $\psi_{topo}$ and $\psi_{lindisp}$ are improved.

The advantage of this technique is that even interferograms with large spatial baselines can be used and displacements of single coherent scatterers in vegetated areas can be estimated. The disadvantage is that a least about 30 images are needed before this estimation technique can be used.

### 3.3.2 Stanford Method for Persistent Scatterers

The Stanford Method for Persistent Scatterers (StaMPS) (Hooper et al., 2004, 2007) assumes that no prior knowledge about the temporal behaviour of the object displacement exists. It is rather assumed that the displacement is spatially smooth. The Persistent Scatterer (PS) selection is done based on the spatial phase stability. By that, a single stable scatterer that behaves different to its surroundings might not be detected as PS. After the selection, similar to Ferretti et al. (2000), the residual topographic phase is estimated as a linear function of spatial baseline. The 3D phase unwrapping is regarded as a series of 2D problems as, due to the spatial smoothness assumption, the differences between neighbouring PSs are expected to be small. The 2D unwrapping is solved using an iterative least square technique. The temporal phase signal can be obtained by summing all spatially unwrapped values with respect to a reference PS. The spatially correlated error (atmosphere, orbit, residual topographic error) can be estimated by temporal high pass and spatial low pass filtering.

### 3.3.3 Delft PS-InSAR Processing Package

Similar to Ferretti et al. (2000), the Delft PS-InSAR Processing Package (DePSI) (Kampes and Hanssen, 2004; Kampes, 2006) selects PSs based on the ADI. According to Sousa et al. (2009), this leads to a lower PS density in non-urban areas compared to StaMPS because low ADI can mainly be found in urban areas. A subset of the selected PSs is used as reference network to estimate the APS. Displacements can be modeled as linear with time (or higher order models). Thus, some knowledge about the temporal behaviour must exist beforehand. The temporal unwrapping and estimation of residual topographic phase and displacement is done with the Integer Least Squares (ILS) and the APS is determined by filtering the residuals similar to Ferretti et al. (2000). After that, the unknown parameters of the remaining PS are determined using ILS.

# 4 Real-time Monitoring Concept

Different approaches must be considered in the monitoring of object displacements with GB-SAR depending on the expected rate of movement. In case of fast movements ($v > 0.5$ mm/day), the object should be monitored continuously with sampling rates of 5 to 10 min. Even for velocities $v < 0.5$ mm/day a continuous monitoring with a high sampling rate should be considered, to be able to assess the atmospheric effects and avoid phase unwrapping problems as best as possible. For velocities $< 20$ mm/year the monitoring can be done in campaigns with a duration of several days and a time span of several weeks to month in-between the campaigns. This work is concerned with continuous monitoring of displacements.

The real-time evaluation of displacement monitoring can act as basis for making rapid decisions in terms of countermeasures and evacuation. Here, real-time evaluation means the creation of displacement maps with the shortest delay possible. Generally, the InSAR analysis described in section 3.2 can be done in real-time, due to the analysis being done interferogram by interferogram. However, from the interferogram examples shown in section 3.2.1, it can be seen that even for GB-SAR with short time intervals, temporal decorrelation can prevent the successful InSAR analysis. Thus, PSI can increase quality and reliability of the estimated displacements. The described PSI techniques in section 3.3 were developed for spaceborne SAR and therefore use some assumptions which have to be reviewed carefully for GB-SAR.

The most profound difference between spaceborne and GB-SAR is the zero-baseline condition and therefore no residual topographic phase exists. Another difference is the observation period and sampling rate. While the sampling rate of spaceborne SAR is usually several days or weeks, it is several minutes for GB-SAR. Thus, the observation period might be limited to a few hours, days or weeks. The assumption of all PSI techniques, that the atmospheric phase is temporally uncorrelated, is therefore not true. Furthermore, the displacement monitoring should not be limited to a linear displacement model only. The algorithm should rather be flexible in the choice of displacement model and even be able to operate when almost no prior information about the expected displacements exist.

Since PSI operates on time series, the algorithms are only partly real-time capable. If one observation is added, the whole analysis must be repeated, which is not efficient. To avoid this, the analysis could be done on a moving window (i.e. use only the last $n$ samples), but nevertheless the computational effort is immense. Here, a concept for a true real-time PSI algorithm using Kalman Filtering is presented, particularly trying to fulfill all conditions and requirements for GB-SAR.

The processing concept is based on the PSI techniques described in section 3.3. According to Ferretti et al. (2000) and Kampes (2006), it is distinguished between PS and Persistent Scatterer Candidate (PSC). Here, PSs are all scatterers matching a certain selection criteria, while the PSCs are a subset of this selection. The PSCs are used to initially estimate phase ambiguity, atmosphere and displacement by using temporal and spatial unwrapping techniques. The PSs are integrated later.

The goal is to determine the displacement for each time step at each PS in near-real-time, i.e. with the least delay possible after the measurement at this time step is finished. The displacement $d$ is connected to the observed wrapped interferometric phase $\phi^w$ by

$$\phi^w = \frac{\lambda}{4\pi}d + \phi_{atm} + \phi_{noise} - 2\pi n. \tag{4.1}$$

Since part of the phase signal (e.g. atmosphere) is assumed to be spatially low frequent, the phase unwrapping, i.e. determination of $n$, can be simplified by considering the double differenced phase of two neighbouring PSCs (Ferretti et al., 2000; Kampes, 2006). The neighbouring PSCs are determined by triangulation such that the distance between the neighbours is as small as possible. A directed network basically consists of a set of nodes $N$ (here PSCs), arcs $A$ and triangles (Ahuja et al., 1993). An arc $(i, j)$ is defined by tail node $i$ and head node $j$ with $i, j \in N$ (see Figure 4.1). For simplicity, arc $(i, j)$ is defined such that $i < j$. A triangle $(i, j, k)$ is defined by three arcs $(i, j)$, $(j, k)$ and $(i, k)$ with $i < j < k$. Every arc must be part of at least one triangle. Details of the selection criteria for the PSs and PSCs and of the triangulation are given in section 4.1.

The wrapped double differenced phase at each arc $(i, j)$ is then computed by

$$\psi_{ij}^w = \mathcal{W}\left\{\phi_j - \phi_i\right\}, \tag{4.2}$$

whereas $\phi_i$ and $\phi_j$ is the interferometric phase at PSCs $i$ and $j$ with respect to a master image. The functional model of the double differenced phase is given by

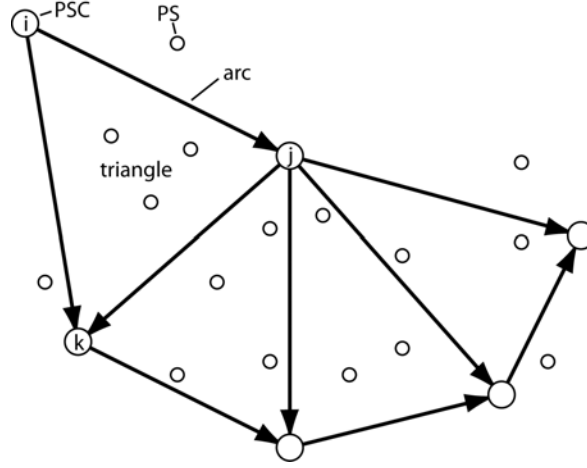$$\psi = \psi_{disp} + \psi_{atm} + \psi_{noise}. \tag{4.3}$$

Figure 4.1: PS and PSC network.

Both, the atmospheric component $\psi_{atm}$ and noise $\psi_{noise}$, are excepted to be small since only scatterers with good phase standard deviation are selected as PSC and the arc should be as short as possible. Due to the high sampling rate of GB-SAR, phase unwrapping could be performed by temporally unwrapping the double differenced phase at each arc with the Itoh-method (see section 3.1). However, atmospheric disturbances and temporarily increasing noise due to e.g. rain can cause unwrapping difficulties at certain time steps, which will propagate through time. Thus, greater effort must be made to avoid unwrapping errors at these critical time steps. The concept of a real-time approach for temporally unwrapping the double differenced phase is given in section 4.2.

The result of the temporal unwrapping at each arc can be verified and corrected by the spatial condition, that the sum of the unwrapped phase at each arc within a triangle $(i, j, k)$ must be zero

$$\psi_{ij} + \psi_{jk} - \psi_{ik} = 0. \tag{4.4}$$

Details are given in section 4.3. The remaining PSs are then integrated into the network by spatial unwrapping only.

After unwrapping, the atmosphere has to be corrected for. Different methods are given in section 4.4. The complete real-time processing chain is presented in section 4.5.

## 4.1 Network Configuration

PSs are defined as pixels within a SAR image, that are temporally stable point targets with a low phase variance (less then about 0.3 rad, see also section 2.1.5). According to Kampes (2006) it is distinguished between PS and PSC, whereas his definition differs somewhat from the definition of Ferretti et al. (2001). PSs are selected by thresholding on a selection criteria and the PSCs are a subset of this selection. Details on the PS and PSC selection are given in section 4.1.1 and 4.1.2, respectively. The temporal unwrapping is not performed at the PSCs itself but rather at arcs each of which connects two neighbouring PSCs. To determine the neighbouring PSCs, a triangulation is performed which is described in section 4.1.3.

The stability of the PSs can vary with time. PSs could be totally lost, due to e.g. sudden fast movements, snow, etc. The temporal variability of the PS selection is discussed in section 4.1.4.

### 4.1.1 PS Selection

Many different selection criteria are thinkable for selecting a set of PSs. Kampes (2006) discussed three different selection methods: based on amplitude, Signal to Clutter Ratio (SCR) and Amplitude Dispersion Index (ADI). The three selection methods are shortly reviewed with respect to GB-SAR and real-time evaluation.

Using directly the amplitude as selection criteria has the advantage that it is very fast and simple. Generally, the PS selection can be done with only one image available. Nevertheless, the availability of a set of images increases the probability of finding true PSs. The disadvantage is that a selection threshold is difficult to define, as the amplitude depends on instrument parameters and distance. Furthermore, a high amplitude does not guarantee that this pixel is a PS.

 The SCR is defined as the ratio between signal and clutter power, i.e. the unwanted backscattering of the background. In a SAR image, it can be estimated by forming the ratio between the power of the signal itself (i.e. the pixel under consideration) and the power of the clutter (i.e. the surrounding pixels) (e.g. Freeman, 1992; Adam et al., 2004). The advantage is that this selection criteria is also available with the first image. The disadvantage is that when the PS density is very high, the estimation of the clutter power is biased and actual PSs are not identified as such. Experimental data acquired with IBIS-L showed that only a very low number of stable targets could be identified by this method, because the PS density at a natural surface (e.g. rock faces or bedrock) is usually very high.

 As stated in section 3.3.1, the ADI defined by $D_a = \frac{\sigma_a}{m_a}$ equals the phase standard deviation of targets with high SNR (see section 3.3.1 and 2.2.5). Figure 4.2 shows the relation between ADI and true phase standard deviation (Ferretti et al., 2001). The graph was created by simulating signals with amplitude 1 with different noise levels. For low phase standard deviation, the ADI agrees well with the phase standard deviation. For higher deviations, the ADI tends to a value of 0.5. This is because the amplitude of low SNR signals is Rayleigh distributed (Ferretti et al., 2001; Papoulis, 1965).
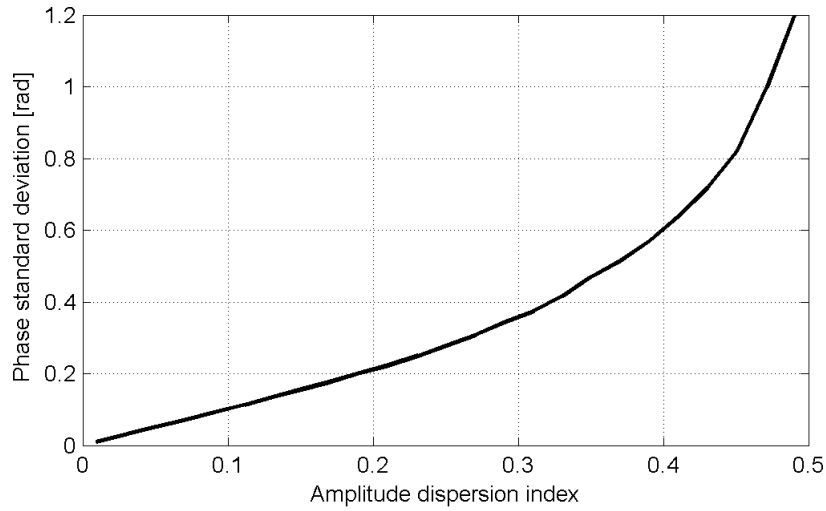


Figure 4.2: Relation between ADI and phase standard deviation derived by simulation after Ferretti et al. (2001).

 Since for the PS selection only targets with a high SNR are of interest, the ADI approximates well the phase standard deviation. The disadvantage of this method is that at least 20 images are needed until the estimate of the ADI is reliable (Adam et al., 2004). Due to that, an initial set of images is required for real-time applications to compute a reliable PS selection criteria. The temporal variability of ADI and possible ways to handle this are discussed in section 4.1.4. The selection threshold for the PS should not be too limiting and range between 0.2 and 0.35.

### 4.1.2 PSC Selection

The selection of PSCs as a subset of the PSs can be done by dividing the 2D image into segments of equal size and selecting in each segment the PS with a best ADI (Kampes, 2006). By that, the PS selection is basically thinned out. Figure 4.3 shows a simulated PS selection. 1831 PSs were selected by thresholding on the ADI. The 189 PSCs were selected using segments of size $5 \times 5$ m$^2$. In each segment only one PS is marked as PSC.

 The choice of the size of the segments to thin out the PS selection depends on the maximum range and spatial resolution of the image. Furthermore, the expected spatial distribution of the displacements should be considered in the decision e.g. if it is known that only a small area is moving, the spatial density of the PSC should be high enough to cover this area. Thus, it is recommended that the size of the segments ranges between a few square meters up to $30 \times 30$ m$^2$. The larger the distance between the PSC, the higher is the danger of unwrapping errors due to atmospheric artefacts, since the atmospheric effect at the arcs connecting the neighbouring PSC is assumed to be small.
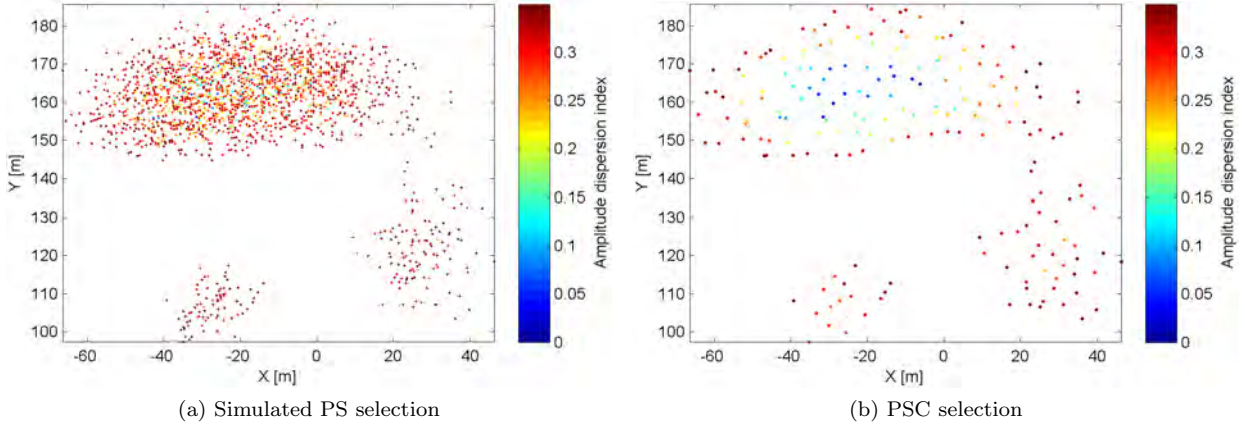
(a) Simulated PS selection                                                        (b) PSC selection

Figure 4.3: Simulated PS/PSC network. The PSC selection was done by dividing the grid into segments of size 5 x 5 m.

### 4.1.3 Triangulation

For triangulation of the PSCs, the Delaunay triangulation is used as basis (Delaunay, 1934; Lee and Schachter, 1980). It finds a set of triangles by maximizing the minimum angles of all triangles. The condition, that the atmospheric phase is small, is only valid if the arc length is small. Thus, triangles where the maximum arc length exceeds a certain threshold are deleted. The maximum arc length should at least be $2 \times$ the edge length of segments used for the PSC selection to avoid too many poorly connected PSC. To reconnect unconnected PSCs and to fill gaps in the network, few longer arcs are allowed to connect the different network parts. By that, it is assured that the maximum arc length is limited but all PSCs of the network are connected to each other and each PSC is part of more than one triangle if possible. Nevertheless, arcs exceeding a few hundred meters should be only used if there is no other possibility as they are very likely to cause unwrapping difficulties during difficult weather situations or when the difference of the rate of movement between the two PSC is large.

Figure 4.4 shows the different steps necessary to create the network. Here, the arc length was limited to 15 m. For connecting different network parts and adding redundancy, arc lengths up to 40 m are allowed.

### 4.1.4 Temporal Variability of PS/PSC Selection

The determination of the ADI for selecting PSs is made based on an initial set of images (e.g. the first 20 or 30 images). Thus, the PS selection depends on the initial situation. Atmospheric disturbances, rockfalls or rain and snow can considerably alter the character of a PS or even totally destroy it. Atmospheric disturbances are normal fluctuations of the signal power, which more or less affect all PSs in a similar way. Due to rain or snow, PSs can be lost temporally and reappear later. Rock falls or fast moving landslides can totally change the structure of the observed area and cause the permanent loss of a PS. Thus, the PS and PSC network is constantly changing in shape.

For simplification, the PS selection can be regarded temporally stable and only the PSC subset is changing. The PSs are selected based on the condition $D_a \leq D_{a,PS}$, whereas the ADI $D_a$ is computed from the initial 20 to 30 images. The threshold $D_{a,PS}$ should be not be too limiting (usually between 0.2 and 0.35) as the PS selection is regarded fixed with time.

The initial PSC subset is determined as described in section 4.1.2 by dividing the image into segments of equal size and determining the scatterer with the minimum ADI $D_{a,min}$ in each segment. Additionally a PSC has to fulfill the condition $D_a \leq D_{a,PSC}$ whereas $D_{a,PSC} < D_{a,PS}$ (usually between 0.1 and 0.2). Thus, in some segments which only contain PSs with $D_a > D_{a,PSC}$ no PSC might be identified.

In each time step, the ADI is updated, e.g. by always computing the ADI of the last 30 images. A PSC is defined as "to be deleted" when the new ADI of this scatterer does not fulfill the PS selection criteria anymore, i.e. if $D_a > D_{a,PS}$. In each segment, which now contains no PSC, it is checked if a new PSC can be identified in the PS selection, which fulfills the condition $D_a \leq D_{a,PSC}$.

Figure 4.5 shows the variation of the mean ADI of selected pixels with time. In this case, every 30 images the ADI was updated. In the upper graph, it can be seen that there is a daily variation, which comes from atmospheric fluctuations. The ADI is usually lower during night than during day. A factor can be determined

(a) Delaunay triangulation

(b) Long arcs removed

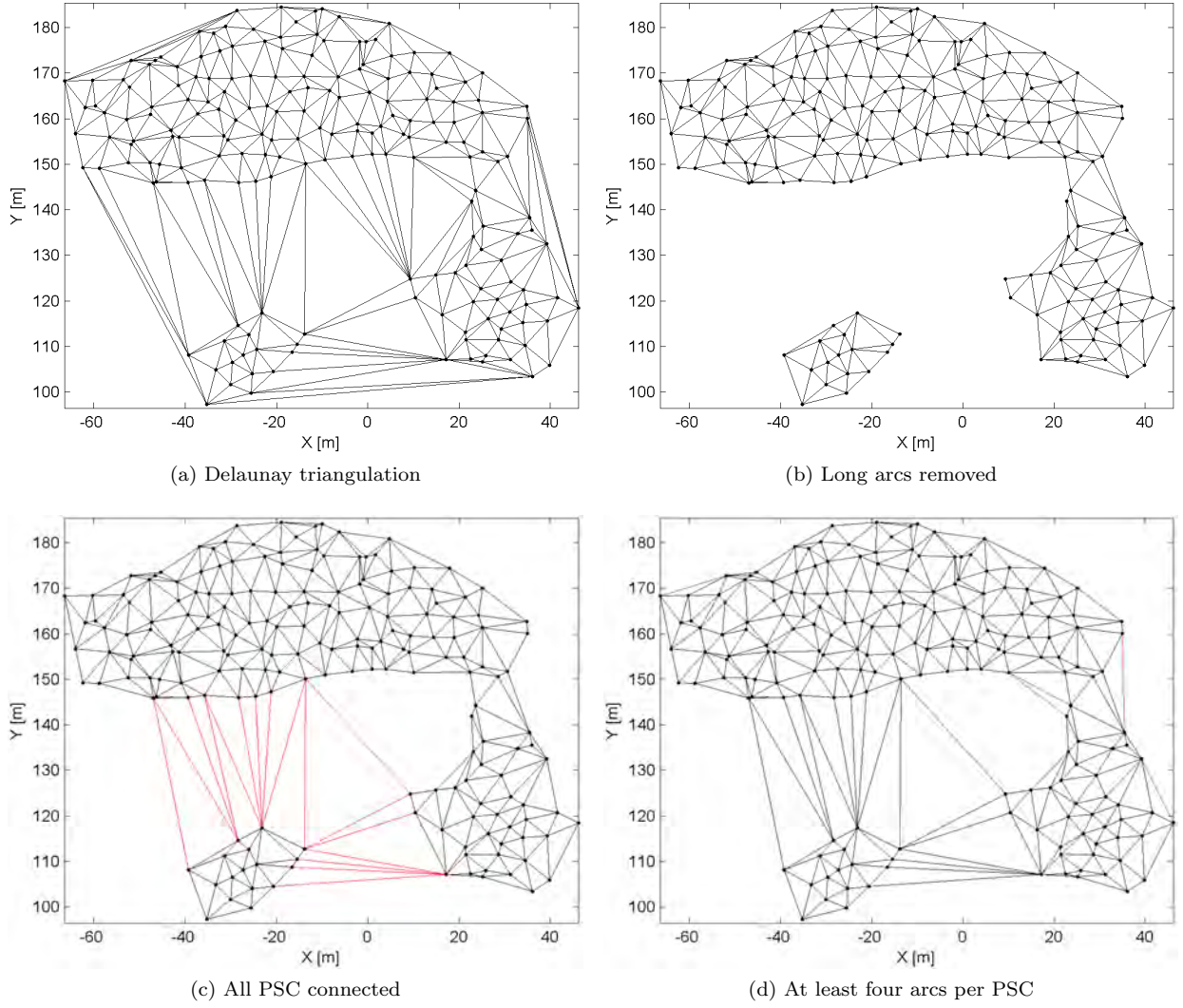(c) All PSC connected

(d) At least four arcs per PSC

Figure 4.4: Creation of the triangulated network by limiting the arc length to 15 m. For closing gaps and assuring redundancy arc lengths up to 40 m are allowed.

to account for these variations. The calibration factor $c$ is defined as the factor which relates the determined ADI to the initial ADI

$$c = \frac{\sum(D_a - D_{a,0})}{\sum D_{a,0}}, \tag{4.5}$$

whereas $D_{a,0}$ is the initial ADI, determined from the first 30 images, and $D_a$ is current ADI. The calibrated ADI $D_{a,cal}$ can be determined by

$$D_{a,cal} = D_a - cD_{a,0}. \tag{4.6}$$

The lower graph in Figure 4.5 shows a smaller daily variation, but the increase of ADI during snow (around day 11) is still visible.

Due to the temporally variability of the PS and PSC selection, the triangulation of the PSC, described in section 4.1.3, is also time-dependent. Figure 4.6 shows the concept of adding and removing a PSC and its corresponding arcs.

## 4.2 Temporal Unwrapping

The concept of the real-time temporal unwrapping for GB-SAR is based on the work of Marinkovic et al. (2005) who describe the use of Multiple Model Adaptive Estimation (MMAE) for recursive temporal unwrapping of spaceborne InSAR data.
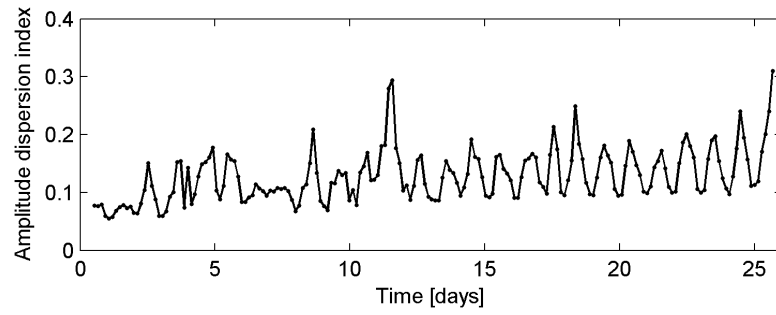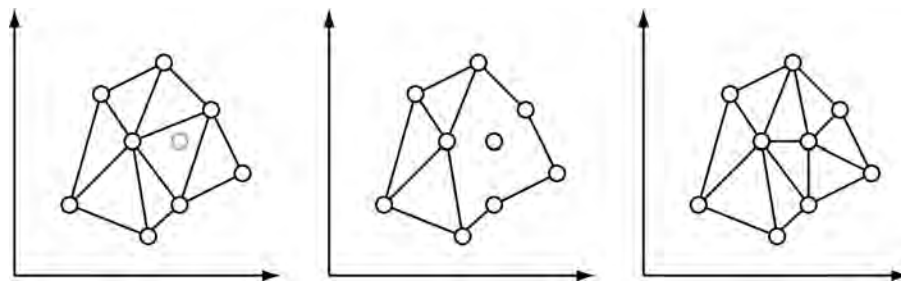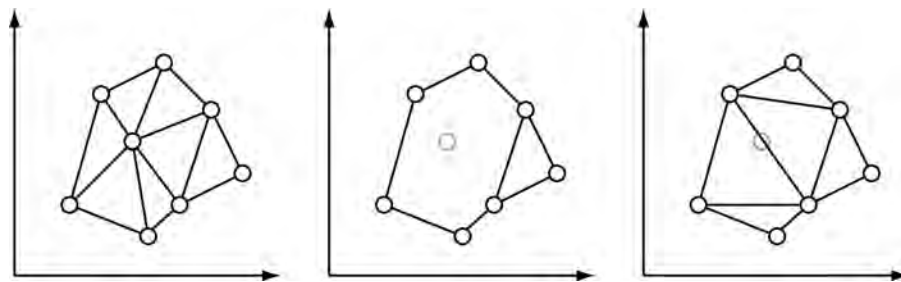
(a) Determined ADI
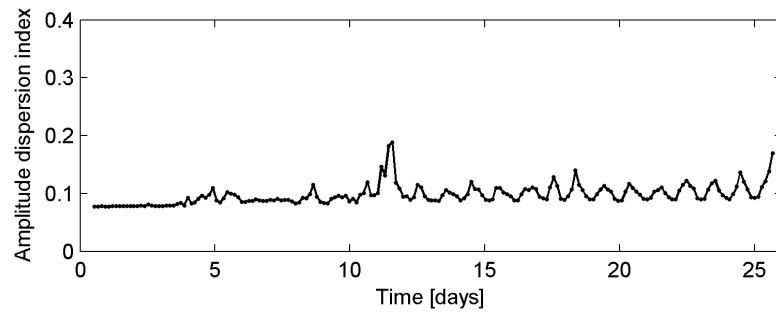


(b) Calibrated ADI

Figure 4.5: The ADI is varying over time due to daily atmospheric variations and changing weather conditions.



(a) Adding a PSC



(b) Deleting a PSC

Figure 4.6: Concept of adding and removing PSCs due to changes in the ADI.

For each arc and each ambiguity set, one Kalman filter exists. A Kalman filter is a recursive filter to estimate the state of a linear dynamic process by minimizing the mean squared error (Brown and Hwang, 1997; Kalman, 1960). It consists of the set of equations for predicting the future state of a process and updating this prediction with new measurements. The Kalman filter equations and some selected models are described in section 4.2.1 and 4.2.2, respectively. The concept of the MMAE is described in section 4.2.3.

### 4.2.1 Kalman Filter Equations

The Kalman filter equations can be divided into two groups: the time-update equations and measurement-update equations: in the time-update the future state of the process is predicted (a priori estimation); in the measurement-update the estimation of the predicted state is updated with a new measurement (a posteriori estimation) (Brown and Hwang, 1997; Grewal and Andrews, 2001).

The goal of the discrete Kalman filter is to estimate the state vector $\mathbf{x}_k$ ($m \times 1$) with $m$ state parameters at time step $k$ defined by

$$\mathbf{x}_k = \mathbf{T}_{k-1} \cdot \mathbf{x}_{k-1} + \mathbf{w}_{k-1}, \tag{4.7}$$

where $\mathbf{T}_{k-1}$ ($m \times m$) is the state transition matrix relating the state at time $t_k$ to the state of the past at time $t_{k-1}$. The process noise $\mathbf{w}_k$ ($m \times 1$) is normal distributed with $\mathbf{w}_k \sim \mathcal{N}(0, \mathbf{Q}_k)$. The observation vector $\mathbf{z}$ ($l \times 1$) with $l$ observations is defined by

$$\mathbf{z}_k = \mathbf{H}_k \cdot \mathbf{x}_k + \mathbf{v}_k, \tag{4.8}$$

whereas $\mathbf{H}_k$ ($l \times l$) is the measurement matrix relating the state of the process to the measurements and $\mathbf{v}_k$ ($l \times 1$) is measurement noise defined by $\mathbf{v}_k \sim \mathcal{N}(0, \mathbf{R}_k)$.

Starting from the a priori estimate for the state vector $\hat{\mathbf{x}}_k^-$ with covariance matrix $\mathbf{P}_k^-$ at time step $k$, the innovations $\mathbf{d}_k$ (i.e. difference between measurement $\mathbf{z}_k$ and a priori estimation) with covariance matrix $\mathbf{D}_k$ are computed by

$$\mathbf{d}_k = \mathbf{z}_k - \mathbf{H}_k \cdot \hat{\mathbf{x}}_k^-, \qquad \text{and} \qquad \mathbf{D}_k = \mathbf{H}_k \cdot \mathbf{P}_k^- \cdot \mathbf{H}_k^{\mathrm{T}} + \mathbf{R}_k. \tag{4.9}$$

The a posteriori estimate of the state vector $\hat{\mathbf{x}}_k^+$ and its covariance matrix $\mathbf{P}_k^+$ are computed by

$$\hat{\mathbf{x}}_k^+ = \hat{\mathbf{x}}_k^- + \mathbf{K}_k \cdot \mathbf{d}_k, \qquad \text{and} \qquad \mathbf{P}_k^+ = \mathbf{P}_k^- - \mathbf{K}_k \cdot \mathbf{H}_k \cdot \mathbf{P}_k^-, \tag{4.10}$$

with $\mathbf{K}_k$ being the Kalman gain matrix

$$\mathbf{K}_k = \mathbf{P}_k^- \cdot \mathbf{H}_k^{\mathrm{T}} \cdot \mathbf{D}_k^{-1}. \tag{4.11}$$

The state of the following time step $k + 1$ can be predicted by

$$\hat{\mathbf{x}}_{k+1}^- = \mathbf{T}_k \cdot \hat{\mathbf{x}}_k^+, \qquad \text{and} \qquad \mathbf{P}_{k+1}^- = \mathbf{T}_k \cdot \mathbf{P}_k^+ \cdot \mathbf{T}_k^{\mathrm{T}} + \mathbf{Q}_k. \tag{4.12}$$

With that the loop is closed as shown in Figure 4.7: the predicted state can be updated with new measurements using equation 4.9 and following. The a priori estimate of state vector $\hat{\mathbf{x}}_k^-$ with $\mathbf{P}_k^-$ at time step $k = 0$ must be determined from initial assumptions.
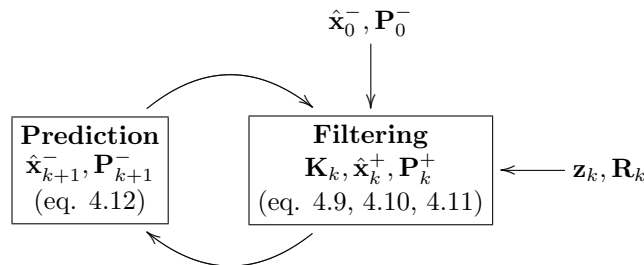


Figure 4.7: Kalman filter loop.

### 4.2.2 Process Model

The key to successful Kalman filtering is the determination of underlying model. The choice of model depends on the characteristics of displacements that are expected (e.g. linear, periodic, ...). If no detailed information on the expected displacements are available, the phase can be modelled as stochastic or kinematic process.

Kinematic models describe the movement of an object based on the equations of motion (Bar-Shalom et al., 2001). In contrary to dynamic models, the reason for this motion is not analysed. A discrete second-order kinematic model (white noise acceleration) assumes that the acceleration is a piecewise constant white noise sequence, i.e. the acceleration is constant during one sampling period. In a third-order model (Wiener process acceleration), the same is true for the acceleration increment. The process and measurement equation for these two processes is given in Table 4.1. The standard deviation $\sigma$ of acceleration or acceleration increment has to be chosen according to the maximum displacements that are expected.

| Model | Process equation $\mathbf{x}_k = \mathbf{T}_{k-1} \cdot \mathbf{x}_{k-1} + \mathbf{w}_{k-1}$ | Measurement equation $\mathbf{z}_k = \mathbf{H}_k \cdot \mathbf{x}_k + \mathbf{v}_k$ |
|---|---|---|
| **White noise acceleration** ($\sigma^2$) | $\mathbf{T} = \begin{bmatrix} 1 & \Delta t \\ 0 & 1 \end{bmatrix}$, $\mathbf{Q} = \sigma^2 \begin{bmatrix} \frac{1}{4}\Delta t^4 & \frac{1}{2}\Delta t^3 \\ \frac{1}{2}\Delta t^3 & \Delta t^2 \end{bmatrix}$ | $\mathbf{H} = \begin{bmatrix} 1 & 0 \end{bmatrix}$ |
| **Wiener process acceleration** ($\sigma^2$) | $\mathbf{T} = \begin{bmatrix} 1 & \Delta t & \frac{1}{2}\Delta t^2 \\ 0 & 1 & \Delta t \\ 0 & 0 & 1 \end{bmatrix}$, $\mathbf{Q} = \sigma^2 \begin{bmatrix} \frac{1}{4}\Delta t^4 & \frac{1}{2}\Delta t^3 & \frac{1}{2}\Delta t^2 \\ \frac{1}{2}\Delta t^3 & \Delta t^2 & \Delta t \\ \frac{1}{2}\Delta t^2 & \Delta t & 1 \end{bmatrix}$ | $\mathbf{H} = \begin{bmatrix} 1 & 0 & 0 \end{bmatrix}$ |

Table 4.1: Kinematic models for Kalman filtering.

### 4.2.3 Multiple Model Adaptive Estimation (MMAE)

The MMAE uses a number of parallel Kalman filters, implementing different models (Brown and Hwang, 1997). Generally, the bank of Kalman filters can differ completely in terms of process and measurement models, covariance matrix, etc. Here, the observations that are added to the filter are different, because of different ambiguities. Thus, every filter within a bank stands for a different ambiguity set (Marinkovic et al., 2005). Starting from an observation vector $\mathbf{l}^w = [\psi_1^w, \psi_2^w, \cdots, \psi_K^w]^{\mathrm{T}}$ containing a wrapped double differenced phase time series at one arc, the basic solution, i.e. the most probable unwrapping solution without any assumptions on object behaviour, is $\mathbf{l}^u = [\psi_1^u, \psi_2^u, \cdots, \psi_K^u]^{\mathrm{T}}$, which is obtained by Itoh's method (see section 3.1). $K$ is the number of time steps. Based on this solution, possible ambiguity vectors can be defined. If the possible ambiguities of the phase increment are limited by $n \in \{-1, 0, 1\}$, the number of all possible ambiguity vectors is $3^K$. In Figure 4.8 all 27 possible solutions for a time series with $K = 3$ are shown. The black line is the basic unwrapping solution $\mathbf{l}^u$.

In Figure 4.9, the concept of the MMAE is shown. Each box represents a Kalman filter. At time index $k = 1$, the number of filters is 3: one filter for each ambiguity $n \in \{-1, 0, 1\}$. At time index $k = 2$, each filter is split into three filters and so on.

To find the best Kalman filter, i.e. the correct ambiguity vector, the probability for each ambiguity set to be the true one is computed. The posterior probability $p_{k,i}$ at time index $k$ with the hypothesis that the ambiguity vector $\mathbf{n}_i$ is the true one can be computed recursively by (Brown and Hwang, 1997; Marinkovic et al., 2005)

$$p_{k,i} = \frac{f_{k,i} \cdot p_{k-1,i}}{\sum\limits_{j=1}^{N} f_{k,j} \cdot p_{k-1,j}} \tag{4.13}$$

whereas $i = 1, 2, \cdots, N$ with $N$, the number of Kalman filters. The conditional density $f_{k,i}$ is defined by

$$f_{k,i} = \frac{1}{\sqrt{2\pi|\mathbf{D}_{k,i}|}} \exp\left(-\frac{1}{2}\mathbf{d}_{k,i}^{\mathrm{T}} \cdot \mathbf{D}_{k,i}^{-1} \cdot \mathbf{d}_{k,i}\right), \tag{4.14}$$

with $\mathbf{d}_{k,i}$ being the innovation at time index $k$, i.e. the difference between measurement and prediction, and $\mathbf{D}_{k,i}$ being the covariance matrix of the innovation. The unwrapped observations $\mathbf{l} = [\psi_1, \psi_2, \cdots, \psi_K]^{\mathrm{T}}$ can be computed by selecting the ambiguity vector $\mathbf{n}_{max}$ with the maximum probability and adding it to the basic solution $\mathbf{l}^u$:

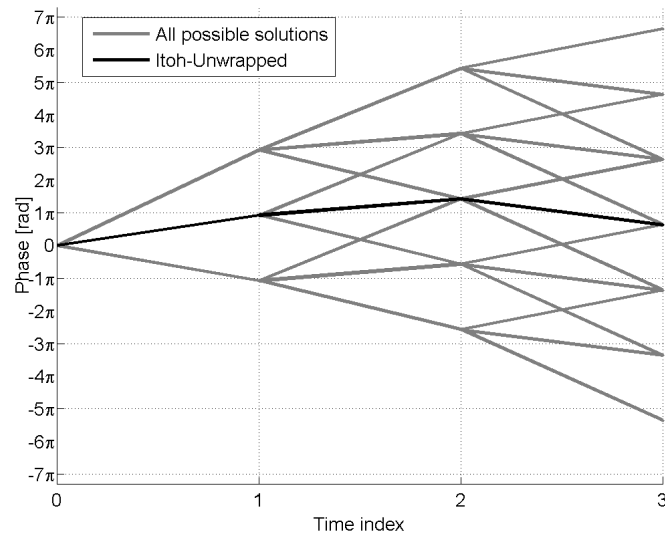$$\mathbf{l} = \mathbf{l}^u + 2\pi\mathbf{n}_{max}. \tag{4.15}$$

Figure 4.8: All 27 possible unwrapping solutions of a time series with $K = 3$ assuming possible ambiguities of $n \in \{-1, 0, 1\}$. The black line is the basic solution using Itoh-unwrapping.
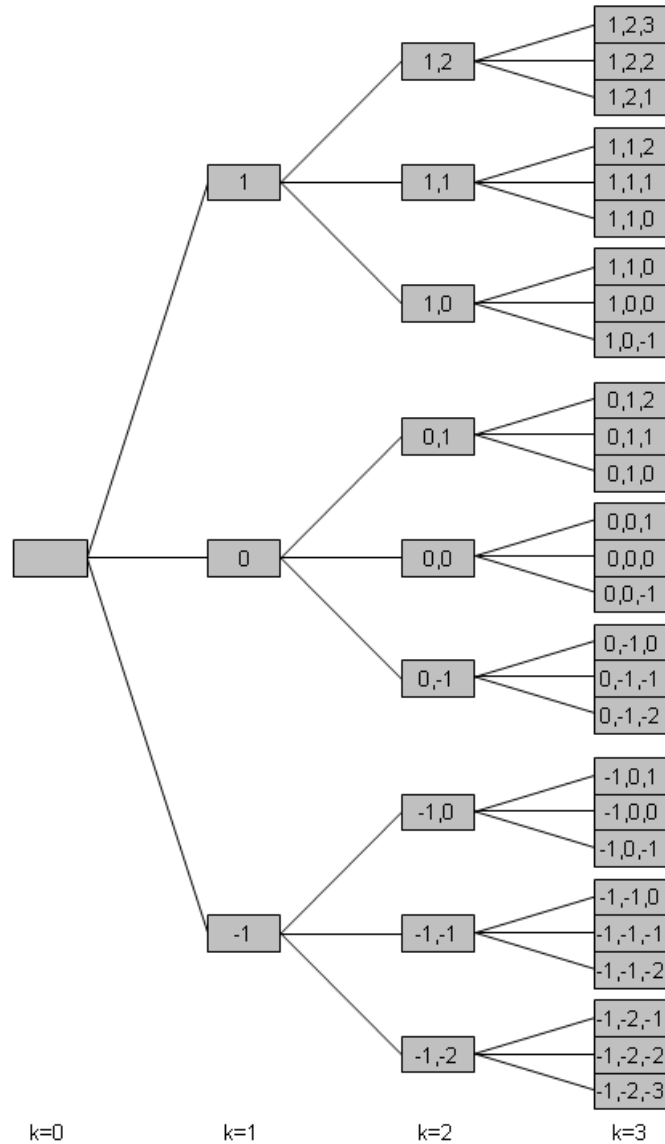


Figure 4.9: Concept of MMAE. Each box is a Kalman filter representing different ambiguity vectors.

The probability distribution is highly sensitive to the choice of process model. Figures 4.10 and 4.11 show
the two most probable solutions for different process models for the time series introduced in Figure 4.8. Fig-
ures 4.10b and 4.10a show the probability distribution and the unwrapped phase of the two best solutions, re-
spectively for a white noise acceleration model with a standard deviation for acceleration of $\sigma = 0.5$ rad/sample$^2$.
Ambiguity vector $\mathbf{n} = [-1, -1, -1]^\mathrm{T}$ is the most probable solution with $p = 0.5$. Figures 4.11b and 4.11a show
probability distribution and unwrapped phase for $\sigma = 5$ rad/sample$^2$. The most probable solution is here
$\mathbf{n} = [0, 0, 1]^\mathrm{T}$ with $p = 0.24$. Here, the probability of the best solution is much lower, which is because a model
with higher variance for the acceleration will adapt more quickly to sudden changes in velocity and also adapt
more quickly to steps induced by unwrapping errors.



(a) Probabilities for each ambiguity vector.

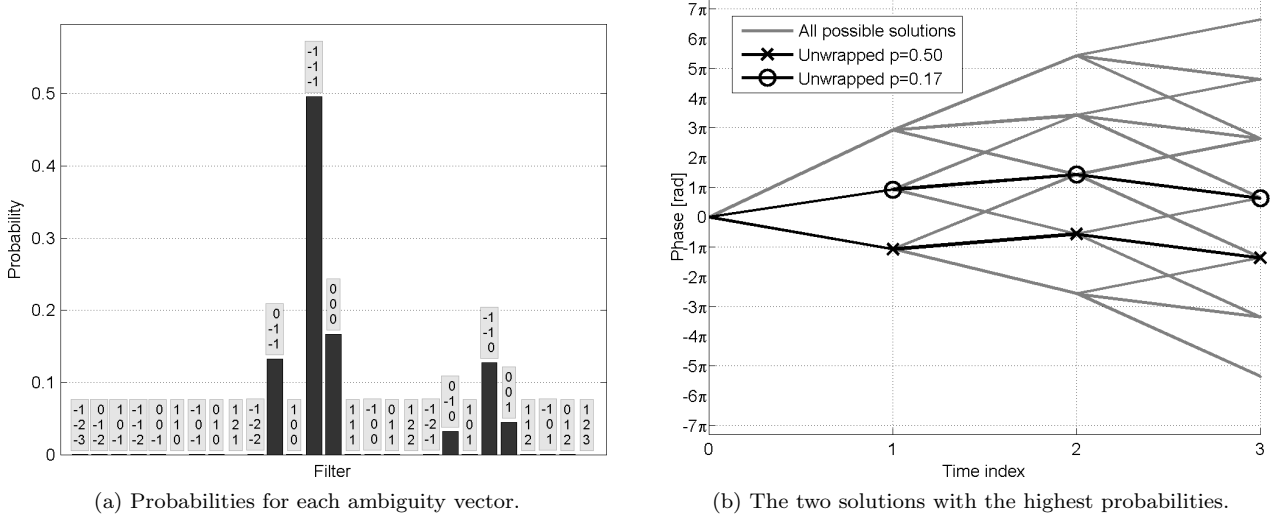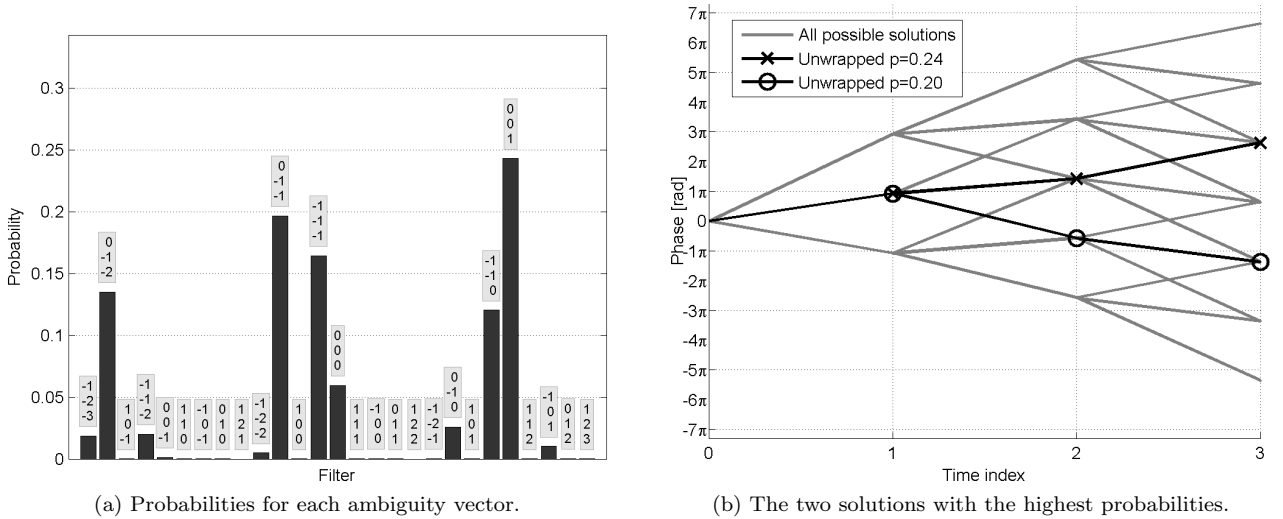(b) The two solutions with the highest probabilities.

Figure 4.10: Probabilities of the 27 different ambiguity vectors and the unwrapped phase of the two best solutions
for a white noise acceleration model with $\sigma = 0.5$ rad/sample$^2$.



(a) Probabilities for each ambiguity vector.

(b) The two solutions with the highest probabilities.

Figure 4.11: Probabilities of the 27 different ambiguity vectors and the unwrapped phase of the two best solutions
for a white noise acceleration model with $\sigma = 5$ rad/sample$^2$.

Due to the exponential increase of the number of Kalman filters, the filter bank could not be handled like this
for long. With three possible ambiguities at every time step, the number of Kalman filter would reach more
than $5^{47}$ after 100 observations. It is impossible and also not reasonable to keep all ambiguity sets even if their
probability is close to zero. As can be seen in Figure 4.10a and 4.11a, the probability of most filters is near
zero. Thus, filters should be deleted when their probability falls below a certain threshold or the number of
filters exceeds a certain limit.

 Furthermore, filters have to be deleted when the correlation between the probability distribution of the filters and the past decision is too low. In Figure 4.12, exemplary the unwrapped and filtered phase of the two most probable solutions after 20 time steps are shown. There is still an unclear situation at time index 5. By adding new observations, the probability ratio between the two best solutions will not change because the filters state is almost identical at time index 20. The ambiguity at time step 5 would never be fixed. To avoid this, a maximum number of time steps has to be defined until an ambiguity must be fixed.
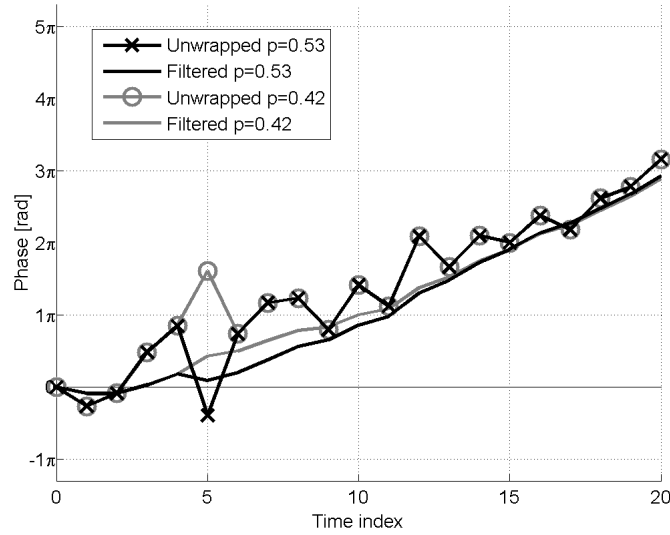
Figure 4.12: Two most probable unwrapping solution of a phase times series with similar probabilities. The ambiguity at time index 5 is still not fixed. At time index 20 the two filtered time series are almost alike.

### 4.2.4 Success Rate

To determine the success rate of the MMAE unwrapping, wrapped phase time series were simulated and unwrapped by Itoh's method and the MMAE. Figure 4.13 shows exemplary the wrapped phase without and with noise. In total, the phase at 625 arcs and 721 time steps was simulated.
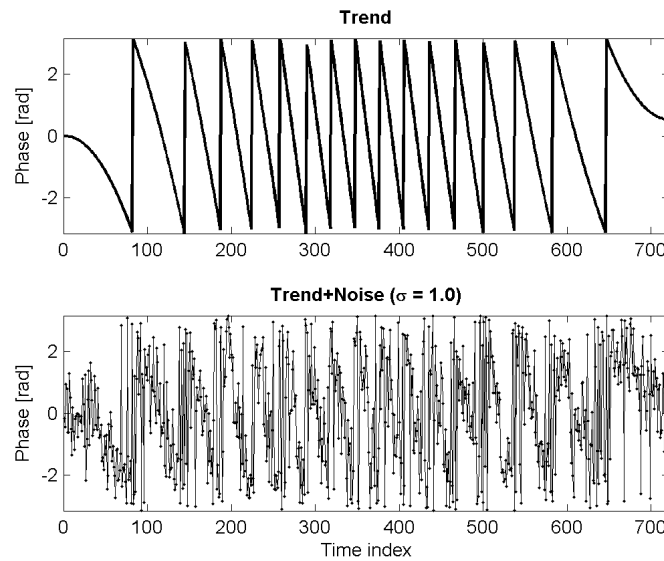
Figure 4.13: Simulated wrapped phase without and with noise.

 Figure 4.14 shows the probability of unwrapping errors for Itoh's unwrapping method and the MMAE approach for different noise levels. An unwrapping error is identified by computing the difference between simulated and unwrapped phase. If the difference is zero, the unwrapping is correct, otherwise false. Thus, a probability of

e.g. 0.2 means that at 20% of all arcs there is a difference between simulated and unwrapped phase at this time index. Up to a noise level of $\sigma_\psi = 0.9$ the probabilities for MMAE do not increase with time, which means that single decisions for ambiguities might be incorrect but the trend of the displacement is estimated correctly. The correct estimation of the displacement trend is much more important than single observations at one time index. At higher noise levels there is a slight increase in unwrapping errors with time. Itoh's method shows this behaviour even at noise levels of $\sigma_\psi = 0.6$.

The advantage of the MMAE is clearly visible. When choosing only PSs with a low ADI (usually below 0.3), one could say that at this noise level there is no benefit of the MMAE. However, the ADI is not temporally stable (see also section 4.1.4). Especially during rain and snow the ADI of PSs can be much higher and the probability for Itoh's method to unwrap incorrect will increase dramatically at these time steps.
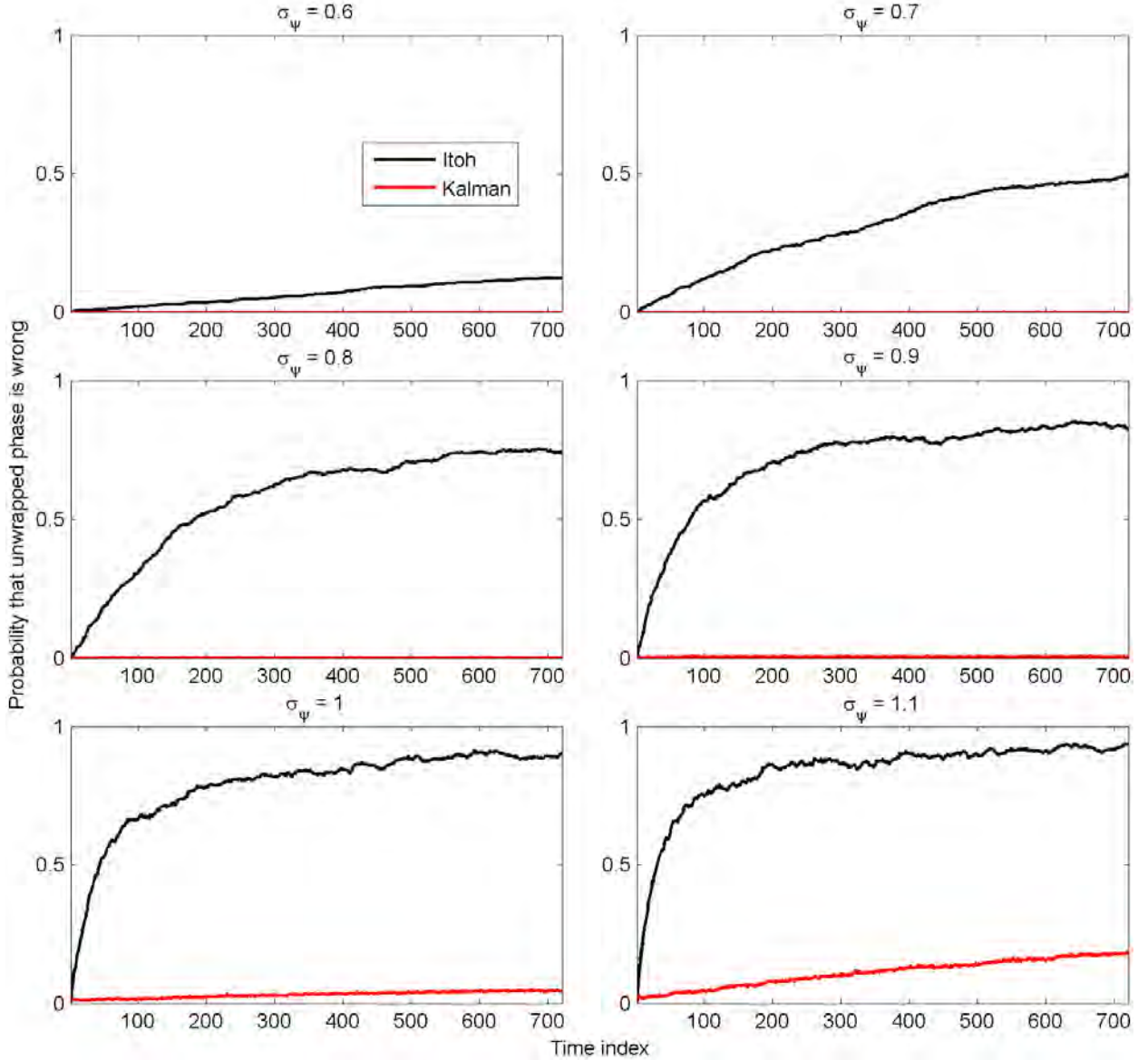


Figure 4.14: Unwrapping error at 625 arcs at 721 time steps with different noise levels unwrapped with Itoh's method and MMAE.

## 4.3 Spatial Unwrapping

The spatial condition for the ambiguity selection is that at each time step the sum of unwrapped phase within each triangle must be zero (see equation 4.4). When only performing temporal unwrapping, this condition may not be fulfilled when selecting the ambiguity set with the highest probability. As the unknown ambiguities $n$ are

integers, Minimum Cost Flow (MCF) algorithms can be used to find a solution for $n$ which minimize the costs (Constantini, 2002). The definition of the MCF problem for spatial unwrapping is given in section 4.3.1. For each arc and time step, the costs for the possible ambiguities are determined by the a-posteriori probabilities of the MMAE. The cost for the ambiguity with the highest probability is always zero. Thus, if the result of the temporal unwrapping is consistent, the result of the spatial unwrapping will be identical with zero costs.

The MCF problem can be solved by linear programming, which is described in section 4.3.2. After the determination of a consistent ambiguity set, the unwrapped phase at the PSC has to be determined by choosing one point as reference point and integrating over space. Further details are given in section 4.3.3.

### 4.3.1 Minimum Cost Flow (MCF)

The MCF model is a fundamental network flow problem which desires to find the cheapest way of shipment through a flow network (Ahuja et al., 1993). Each arc $(i, j)$ within the network has associated with it

- $x_{ij}$ the unit flow on that arc, which is to be determined;
- $c_{ij}$ the costs per unit flow on that arc;
- $u_{ij}$ the capacity which is the maximum amount that can flow on that arc;
- $l_{ij}$ the minimum amount that can flow on that arc.

Each node $i$ has associated with it

- $b_i$ the supply value; if $b_i > 0$ the node is a supply node, if $b_i < 0$ the node is a demand node, if $b_i = 0$ the node is transshipment node.

Flow $x$ is a feasible flow when it satisfies the mass balance constraint

$$\sum_{\{j:(i,j)\in A\}} x_{ij} - \sum_{\{j:(j,i)\in A\}} x_{ji} = b_i, \tag{4.16}$$

with $l_{ij} \leq x_{ij} \leq u_{ij}$ and $\sum_{i \in N} b_i = 0$. The first term is the total outflow of node $i$, the second term is the total inflow. The difference must equal the supply value $b_i$. The costs involved are defined by

$$c(x) = \sum_{(i,j)\in A} c_{ij} x_{ij}. \tag{4.17}$$

The goal of the MCF is to find a feasible flow $x$ with minimum costs $c(x)$

$$\min \sum_{(i,j)\in A} c_{ij} x_{ij}. \tag{4.18}$$

The phase unwrapping problem can be handled as MCF problem (Constantini, 2002; Carballo and Fieguth, 2000). The nodes $N$ are the selected persistent scatterers, arcs $A$ are the connections between the scatterers. Each arc has an unknown ambiguity $n_q$ defined by

$$2\pi n_q = \psi_q - \psi_q^u, \tag{4.19}$$

with $\psi_q - \psi_q^u$ being the difference between unwrapped and Itoh-unwrapped double differenced phase at arc $q$ under the constraint that the sum of the unwrapped phase along each closed loop in the network is zero. For each triangle defined by three nodes $(i, j, k)$ with $i < j < k$ and arcs $(q, r, s)$ with $q = (i, j)$, $r = (j, k)$ and $s = (i, k)$ (see Figure 4.15a), the constraint is given by

$$0 = \psi_q + \psi_r - \psi_s = 2\pi(n_q + n_r - n_s) + \psi_q^u + \psi_r^u - \psi_s^u. \tag{4.20}$$

The minimization problem is defined by

$$\min \sum_{q \in A} c_q |n_q|, \tag{4.21}$$

subject to

$$n_q + n_r - n_s = -\frac{1}{2\pi} \left( \psi_q^u + \psi_r^u - \psi_s^u \right), \tag{4.22}$$

with $l_q \leq n_q \leq u_q$ for each triangle $(q, r, s)$. Due to the fact that $n_q \in \mathbb{Z}$ and that the costs $c_q$ cannot be negative, the minimization problem is nonlinear. To transform the nonlinear problem into a linear problem,
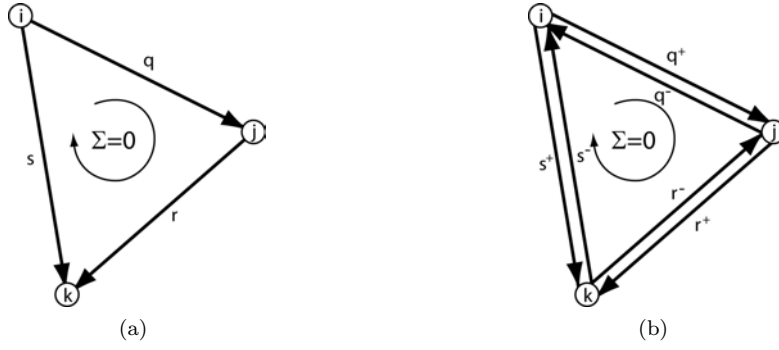
Figure 4.15: Triangle condition for MCF phase unwrapping.

each arc is replaced by two arcs $q^+ = (i,j)$ and $q^- = (j,i)$ with opposite direction (see Figure 4.15b). The flow on arc $q$ is then given by $x_q = |n_q| = n_q^+ + n_q^-$ with $n_q^+ = \max(0, n_q)$ and $n_q^- = \max(0, -n_q)$. The linear minimization problem is then

$$\min \sum_{q \in A} \left( c_q^+ n_q^+ + c_q^- n_q^- \right), \tag{4.23}$$

with $n_q^+, n_q^- \in \mathbb{N}_0$ subject to

$$n_q^+ - n_q^- + n_r^+ - n_r^- - n_s^+ + n_s^- = -\frac{1}{2\pi} \left( \psi_q^u + \psi_r^u - \psi_s^u \right), \tag{4.24}$$

with $0 \le n_q^+ \le u_q$ and $0 \le n_q^- \le -l_q$ for each triangle $(q, r, s)$. The costs $c_q^+$ and $c_q^-$ are the costs involved if $n_q > 0$ and $n_q < 0$, respectively. In that way, different cost functions can be chosen for negative and positive ambiguities. As derived by Carballo and Fieguth (2000), the costs can be expressed by probabilities with

$$c_q^+ = -\ln \frac{p_q^{n=1}}{p_q^{n=0}} \qquad \text{and} \qquad c_q^- = -\ln \frac{p_q^{n=-1}}{p_q^{n=0}}. \tag{4.25}$$

Assuming that only one non-zero ambiguity is considered and the probability of $n_q$ being zero is $p_q^{n=0} = 1 - p_q^{n \ne 0}$, the costs for choosing $n_q \ne 0$ are a function of $p_q^{n \ne 0}$ as shown in Figure 4.16. If the probability of $n_q \ne 0$ exceeded 0.5 (i.e. $n_q \ne 0$ is more probable than $n_q = 0$), the costs would be negative. Thus, $n_q = 0$ must always be the most probable solution to avoid negative costs. If this is not true, the ambiguities must be transformed such that the probability of the transformed ambiguity $\tilde{n} = 0$ is highest which is achieved by $\tilde{n}_q = n_q - n_q^0$ with $n_q^0$ being the ambiguity with the highest probability. The transformed Itoh-unwrapped double differenced phase is $\tilde{\psi}^u = \psi^u + 2\pi n_q^0$.

### 4.3.2 Simplex Method for Solving MCF Problems

One of the most powerful tools for solving linear programming problems is the simplex method. Here, only the general idea of the simplex method is presented. Detailed descriptions and more efficient implementations can be found in (e.g. Ahuja et al., 1993; Dantzig et al., 2003; Luenberger and Ye, 2008).

The MCF problem defined in equations 4.23 and 4.24 can be written in matrix notation as

$$\min \mathbf{c}^{\mathrm{T}} \mathbf{x} \qquad \text{subject to} \qquad \begin{cases} \mathbf{A} \mathbf{x} = \mathbf{b}, \\ 0 \le \mathbf{x} \le \mathbf{u}, \end{cases} \tag{4.26}$$

where cost vector $\mathbf{c}$, flow vector $\mathbf{x}$, upper bound vector $\mathbf{u}$ are $m \times 1$ vectors with $m$ being the number of variables (i.e. two times the number of unique arcs $r$):

$$\mathbf{c} = \begin{bmatrix} \mathbf{c}^+ \\ \mathbf{c}^- \end{bmatrix} = \begin{bmatrix} c_1 \\ c_2 \\ \vdots \\ c_m \end{bmatrix}, \qquad \mathbf{x} = \begin{bmatrix} \mathbf{n}^+ \\ \mathbf{n}^- \end{bmatrix} = \begin{bmatrix} x_1 \\ x_2 \\ \vdots \\ x_m \end{bmatrix}, \qquad \mathbf{u} = \begin{bmatrix} \mathbf{u}^+ \\ \mathbf{u}^- \end{bmatrix} = \begin{bmatrix} u_1 \\ u_2 \\ \vdots \\ u_m \end{bmatrix}. \tag{4.27}$$
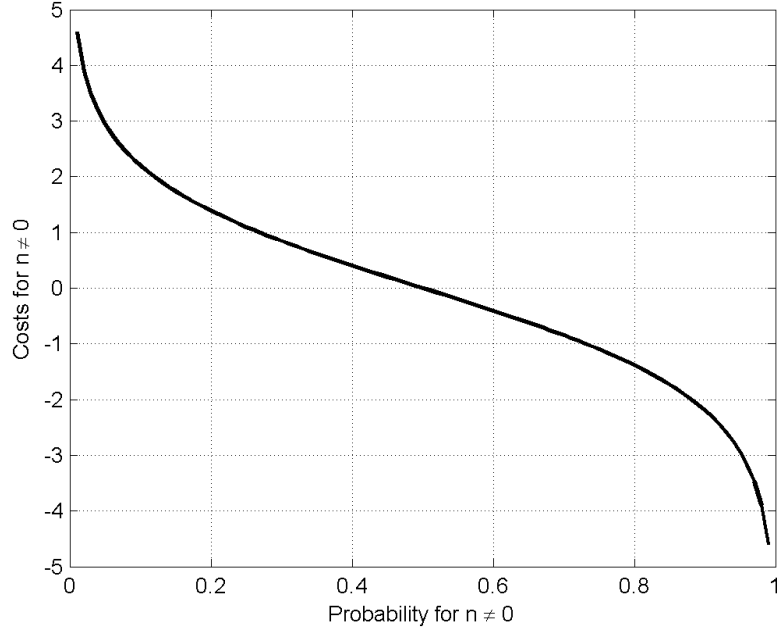
Figure 4.16: Cost function.

$\mathbf{A}$ is a $p \times m$ matrix and $\mathbf{b}$ is a $p \times 1$ vector defining $p$ constraints (i.e. one for each triangle) in form of linear equalities:

$$\mathbf{A} = \begin{bmatrix} \mathbf{A}^+ & \mathbf{A}^- \end{bmatrix} = \begin{bmatrix} a_{11} & a_{12} & \cdots & a_{1m} \\ a_{21} & a_{22} & \cdots & a_{2m} \\ \vdots & \vdots & & \vdots \\ \vdots & \vdots & & \vdots \\ a_{p1} & a_{p2} & \cdots & a_{pm} \end{bmatrix}, \qquad \mathbf{b} = \begin{bmatrix} b_1 \\ b_2 \\ \vdots \\ b_p \end{bmatrix}. \tag{4.28}$$

Matrix $\mathbf{A}^+$ of size $p \times r$ contains the triangle-arc relations and $\mathbf{A}^- = -\mathbf{A}^+$.

The optimization procedure can be divided into phase 1: finding an initial basic feasible solution for flow $\mathbf{x}$ and phase 2: optimize the found solution to minimize the objective function $z(\mathbf{x}) = \mathbf{c}^{\mathrm{T}}\mathbf{x}$. The basic feasible solution can be obtained by isolating one variable in each constraint (i.e. this variable may not appear in any other constraints) because then a solution for the isolated variables that satisfies the equality constraint can be determined by fixing the remaining variables to a specific value. Equation 4.26 with equations 4.27 and 4.28 can be represented as tableau:

$$\begin{array}{cccccccc} \mathbf{a}_1 & \mathbf{a}_2 & \cdots & \mathbf{a}_p & \mathbf{a}_{p+1} & \cdots & \mathbf{a}_m & \mathbf{b} \\ \hline a_{11} & a_{12} & \cdots & a_{1p} & a_{1,p+1} & \cdots & a_{1m} & b_1 \\ a_{21} & a_{22} & \cdots & a_{2p} & a_{2,p+1} & \cdots & a_{2m} & b_2 \\ \vdots & \vdots & & \vdots & \vdots & & \vdots & \vdots \\ a_{p1} & a_{p2} & \cdots & a_{pp} & a_{p,p+1} & \cdots & a_{pm} & b_p \\ \hline c_1 & c_2 & \cdots & c_p & c_{p+1} & \cdots & c_m & z \end{array} \tag{4.29}$$

The number of variables to be isolated equals the number of constraints $p$. The isolation is done by elementary row operations (i.e. multiplication with a constant or adding one row to another). Assuming that the first $p$ variables are isolated, the canonical simplex tableau has the form:

$$\begin{array}{cccccccc} \bar{\mathbf{a}}_1 & \bar{\mathbf{a}}_2 & \cdots & \bar{\mathbf{a}}_p & \bar{\mathbf{a}}_{p+1} & \cdots & \bar{\mathbf{a}}_m & \bar{\mathbf{b}} \\ \hline 1 & 0 & \cdots & 0 & \bar{a}_{1,p+1} & \cdots & \bar{a}_{1m} & \bar{b}_1 \\ 0 & 1 & \cdots & 0 & \bar{a}_{2,p+1} & \cdots & \bar{a}_{2m} & \bar{b}_2 \\ \vdots & \vdots & & \vdots & \vdots & & \vdots & \vdots \\ 0 & 0 & \cdots & 1 & \bar{a}_{p,p+1} & \cdots & \bar{a}_{pm} & \bar{b}_p \\ \hline 0 & 0 & \cdots & 0 & c^{\pi}_{p+1} & \cdots & c^{\pi}_m & z_0 \end{array} \tag{4.30}$$

The isolated variables are named basic variables $\mathbf{x}_B$, the remaining $m - p$ variables are called nonbasic variables $\mathbf{x}_N$. The subset of the transformed matrix $\bar{\mathbf{A}}$ which only contains the columns of the basic variables is referred to a basis matrix $\mathbf{B}$ with size $p \times p$ while the subset of nonbasic variables is referred to as nonbasis matrix $\mathbf{N}$ with size $p \times (m - p)$:

$$\bar{\mathbf{A}}\mathbf{x} = \mathbf{B}\mathbf{x}_B + \mathbf{N}\mathbf{x}_N = \bar{\mathbf{b}}. \tag{4.31}$$

The coefficients of the basic variables in the objective function are zero and vector $\mathbf{c}^{\pi}$ is referred to as reduced cost vector. When the nonbasic variables $\mathbf{x}_N$ are fixed to their lower bound (zero) the basic variables can be determined by

$$\mathbf{x}_B = \mathbf{B}^{-1}\bar{\mathbf{b}} \tag{4.32}$$

The obtained solution for flow $\mathbf{x}$ is feasible if $\mathbf{x}_B$ satisfies the boundary conditions given for $\mathbf{x}$ in equation 4.26. Depending on the variables chosen to be basic variables, the solution is feasible or not.

After the basic feasible solution is obtained, the optimality of the solution is determined. The solution for $\mathbf{x}$ is optimal when the reduced costs of the nonbasic variables are nonnegative. If this is not the case, the optimal solution can be found by iteratively exchanging basic and nonbasic variables by elementary row operations (i.e. pivoting) until the solution is optimal.

In the following, a simple example is discussed. Let $G = (N, A)$ be a directed graph with 4 nodes, 5 arcs and 2 triangles (see Figure 4.17) with $N = \{1,2,3,4\}$ and $A = \{(1,2),(1,3),(2,3),(2,4),(3,4)\}$.
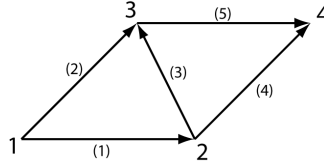


Figure 4.17: Example network.

For simplicity, it is assumed that the ambiguities at each arc are restricted to $n_q \in (0, 1)$ in this example. In the following table, the observed phase, probabilities for $n = 0$ and $n = 1$ and the costs for $n = 1$ are listed:

| $q$ | $i$ | $j$ | $\psi_q^u$ | $p_q^{n=0}$ | $p_q^{n=1}$ | $c_q$ |
|---|---|---|---|---|---|---|
| 1 | 1 | 2 | $-2.0$ | 0.873 | 0.127 | 2 |
| 2 | 1 | 3 | 2.6 | 1.000 | 0.000 | 19 |
| 3 | 2 | 3 | $-1.7$ | 0.928 | 0.072 | 3 |
| 4 | 2 | 4 | 2.4 | 1.000 | 0.000 | 18 |
| 5 | 3 | 4 | $-2.2$ | 0.827 | 0.173 | 2 |

$$(4.33)$$

The costs were computed according to equation 4.25. The minimization problem can be written in matrix form by equation 4.26 with

$$\mathbf{c} = \begin{bmatrix} 2 \\ 19 \\ 3 \\ 18 \\ 2 \end{bmatrix}, \qquad \mathbf{x} = \begin{bmatrix} n_1 \\ n_2 \\ n_3 \\ n_4 \\ n_5 \end{bmatrix}, \qquad \mathbf{u} = \begin{bmatrix} 1 \\ 1 \\ 1 \\ 1 \\ 1 \end{bmatrix}, \qquad \mathbf{A} = \begin{bmatrix} 1 & -1 & 1 & 0 & 0 \\ 0 & 0 & 1 & -1 & 1 \end{bmatrix}, \qquad \mathbf{b} = \begin{bmatrix} 1 \\ 1 \end{bmatrix}. \tag{4.34}$$

In tableau form the minimization problem looks as follows:

| $\mathbf{a}_1$ | $\mathbf{a}_2$ | $\mathbf{a}_3$ | $\mathbf{a}_4$ | $\mathbf{a}_5$ | $\mathbf{b}$ |
|---|---|---|---|---|---|
| 1 | $-1$ | 1 | 0 | 0 | 1 |
| 0 | 0 | 1 | $-1$ | 1 | 1 |
| 2 | 19 | 3 | 18 | 2 | |

$$(4.35)$$

The basic variables to be initially chosen can immediately be identified (variable 1 and 5) and the linear program can be brought into canonical form by adding $-2 \times$ row 1 and $-2 \times$ row 2 to the row containing the costs:

| $\mathbf{a}_1$ | $\mathbf{a}_2$ | $\mathbf{a}_3$ | $\mathbf{a}_4$ | $\mathbf{a}_5$ | $\mathbf{b}$ |
|---|---|---|---|---|---|
| 1 | $-1$ | 1 | 0 | 0 | 1 |
| 0 | 0 | 1 | $-1$ | 1 | 1 |
| 0 | 21 | $-1$ | 20 | 0 | 4 |

$$(4.36)$$

If all nonbasic variables are set to zero ($x_2 = x_3 = x_4 = 0$), the value of the basic variables $x_1$ and $x_5$ can be determined by $\mathbf{Ax} = \mathbf{b}$. Thus, the basic feasible solution is

$$\mathbf{x}^{\mathrm{T}} = \begin{bmatrix} 1 & 0 & 0 & 0 & 1 \end{bmatrix}, \tag{4.37}$$

with objective function $z(\mathbf{x}) = \mathbf{c}^{\mathrm{T}}\mathbf{x} = 4$.

To find the optimal solution, the variable with negative costs is defined as entering variable (i.e. the nonbasic variable to become basic), in this case $x_3$. To identify the corresponding leaving variable (i.e. the basic variable to become nonbasic), it is important that the feasibility of the solution is preserved. Here, $x_3$ is at its lower bound and to find the leaving variable, $x_3$ is set to its upper bound 1. The values $x_1 = 0$ and $x_5 = 0$ can be determined by $\mathbf{Ax} = \mathbf{b}$, which is still a feasible solution as it satisfies the condition $0 \leq \mathbf{x} \leq \mathbf{u}$. Here, one of the two basic variables $x_1$ and $x_5$ can be chosen to become nonbasic as both values are zero. If $x_5$ is defined as the leaving variable, the simplex tableau can be updated to bring it into the canonical form by adding $-1 \times$ row 1 to row 2 and then adding $1 \times$ row 1 to the row containing the costs.

| $\mathbf{a}_1$ | $\mathbf{a}_2$ | $\mathbf{a}_3$ | $\mathbf{a}_4$ | $\mathbf{a}_5$ | $\mathbf{b}$ |
|---|---|---|---|---|---|
| 1 | $-1$ | 1 | 0 | 0 | 1 |
| $-1$ | 1 | 0 | $-1$ | 1 | 0 |
| 1 | 20 | 0 | 20 | 0 | 3 |

$$\tag{4.38}$$

All nonbasic variables are again set to zero $x_1 = x_2 = x_4 = 0$ and the value of the basic variables can be determined by $\mathbf{Ax} = \mathbf{b}$. Now all costs are positive and thus the minimum is found. The feasible solution minimizing the costs is

$$\mathbf{x}^{\mathrm{T}} = \begin{bmatrix} 0 & 0 & 1 & 0 & 0 \end{bmatrix}, \tag{4.39}$$

with objective function $z(\mathbf{x}) = \mathbf{c}^{\mathrm{T}}\mathbf{x} = 3$. Thus, the unwrapped phase at arc 3 is $\psi = -1.7 + 2\pi$.

### 4.3.3 Spatial Integration

After the determination of a consistent ambiguity set for each arc at one time index, the unwrapped phase at the PSCs and PSs has to be determined. This is done by setting one arbitrarily chosen PSC as reference point and assuming its phase time series (i.e. of the PSC itself, not arcs) as correctly unwrapped.

Additionally, the unwrapped phase at the PSs has to be determined. This is be done by spatial unwrapping only (see Figure 4.18). For each PS located inside a triangle of PSCs, three triangle conditions exist. The unwrapping can be again performed by MCF using the ADI at the PSCs to compute the costs. For each PS located outside the triangulation, only one triangle condition exists. This method implies that the displacement has a certain spatial smoothness. In case one PS is moving with a significant larger velocity, this movement will not be detected. On the other hand, if only one PSC is moving with a significant larger velocity, the surrounding PSs will be estimated having a similar displacement rate.
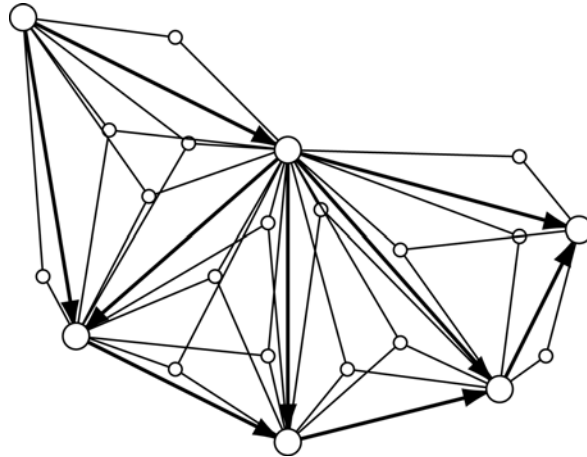


Figure 4.18: For determining the unwrapped phase at the PSs, they are connected with the PSCs of the surrounding triangle.

## 4.4 Atmospheric Correction

In section 3.2.2, different methods were shown to account for the atmospheric phase in interferograms (meteorological observations, estimation at stable targets, spatial interpolation or filtering). All these methods only exploit the spatial properties of the atmospheric phase, i.e. that it is a spatially low-frequency signal. By doing that, a spatially low-frequent displacement signal might be interpreted as atmosphere.

In spaceborne SAR, the atmospheric phase can be assumed to be temporally uncorrelated due sampling intervals of several days. Thus, the atmospheric component can be computed by temporal low pass and spatial high pass filtering the time series. Here, however, the atmospheric component is highly correlated and trends can be caused by long-term changes of atmospheric properties (e.g. seasonal changes). If meteorological observations are available, they should be used to correct the phase data for trends. Necessary parameters to observe are humidity, temperature and pressure. Even if meteorological data is only available at one station near the radar, the accuracy is usually enough to account for long-term trends.

The best way is a correction method that combines meteorological data and filtering techniques. Temporal high frequency atmospheric variations can be determined by selecting stable pixels, whereas the temporal low frequency part is accounted for by applying equation 2.31 to compute the atmospheric phase. Nevertheless, the difficulty remains how to define the stable scatterers. The weather data can be used to determine pixels that are stable by assuming a high correlation between weather data and phase time series. Thus, pixels that are correlated with the weather data are selected as control points and a linear or polynomial model or spatial interpolation techniques can be used to determine the atmospheric effect.

## 4.5 Real-time Monitoring

In the last sections all individual parts of the real-time analysis concept were discussed and now have to be combined. The configuration of IBIS-L and the necessary hardware and accessories are discussed in section 4.5.1. The complete real-time analysis concept is discussed in section 4.5.2.

### 4.5.1 Hardware Configuration

Figure 4.19 shows the configuration of the sensors and their equipment. The power box manages the whole power supply. Power input depends on availability and can be provided by mains power, solar modules, a generator or fuel cells. The use of batteries makes sure that, when the power supply fails, IBIS-L can be operated for at least 24 hours. IBIS-L is connected via USB with the data acquisition laptop. The real-time processing is done on a second laptop which is connected to the IBIS-L laptop via LAN to access the acquired data. Additionally, the processing laptop is responsible for the webcam and weather station control and data acquisition. The weather station should gather at least humidity, temperature and pressure. A rain gauge can be of help to assess trigger effects for displacements and to estimate noise due to rain. A webcam can add useful information on environmental and meteorological conditions. If Wireless LAN (WLAN) is available, the processed data can directly be transferred to a server or accessed remotely.

The most important feature of the concept is the automatic restart in case of power failure. When the power returns, the processing laptop will boot automatically and restart the processing software and data acquisition of the webcam and weather sensor. Furthermore, it wakes the IBIS-L laptop via Wake On LAN, which then continues the monitoring of IBIS-L.

### 4.5.2 Real-time Analysis Software

In Figure 4.21, the complete concept of unwrapping is given. Starting with raw files, the first step, after an observation is finished, is the focusing explained in detail in section 2.1.3. With the focused data, the ADI is updated and the current PSC selection is computed. However, it is possible to omit this step or only carry it out occasionally, to avoid too many changes in the network. After that, the wrapped double differenced phase at the arcs is computed.

The selection of possible ambiguities for time index $t$ is done by computing the a-priori probabilities based on the variance of observations. It is assumed that the double differenced phase is normally distributed and its true value is zero, which is a feasible assumption for short arcs. As shown in section 4.1.1, the ADI is a valid estimation for the standard deviation. The probability for each ambiguity is determined by integrating the probability density function as shown in Figure 4.20, e.g. the a-priori probability for ambiguity $n = 1$ being
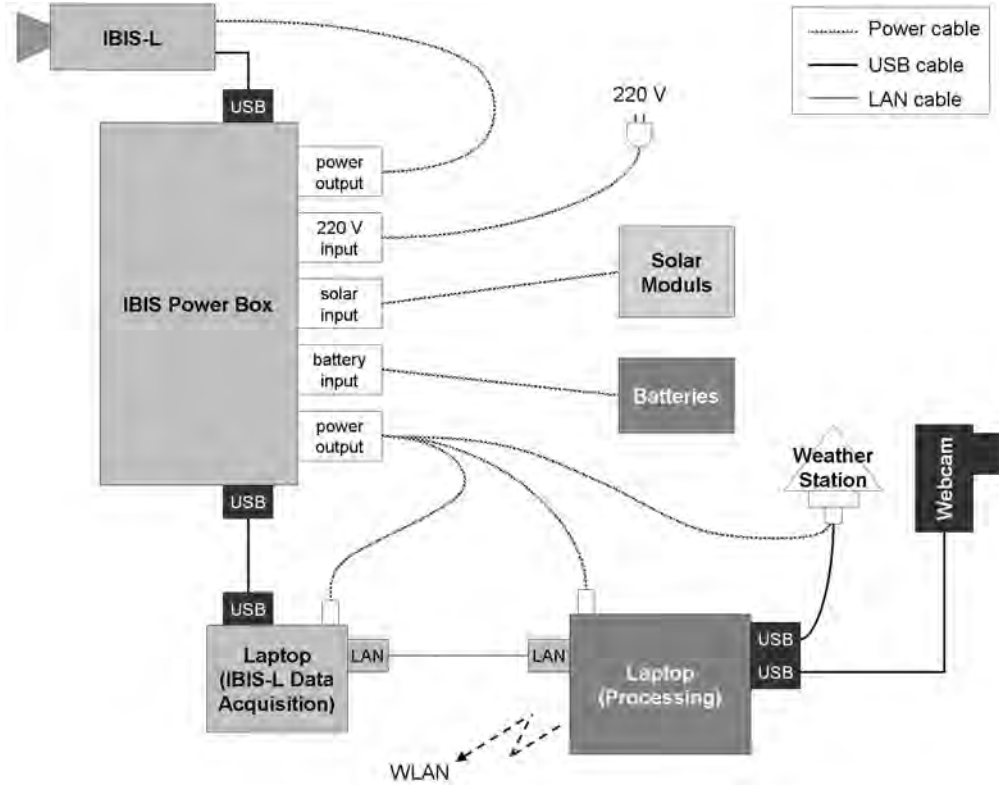
Figure 4.19: Hardware configuration for real-time monitoring.

the correct ambiguity is computed by (Papoulis, 1965)

$$p(n=1) = p(-3\pi \leq \psi \leq -\pi) = \int_{-3\pi}^{-\pi} f(\psi)d\psi, \tag{4.40}$$

with

$$f(\psi) = \frac{1}{\sigma\sqrt{2\pi}} \cdot \exp\left\{-\frac{(\psi - \psi^w)^2}{2\sigma^2}\right\}. \tag{4.41}$$

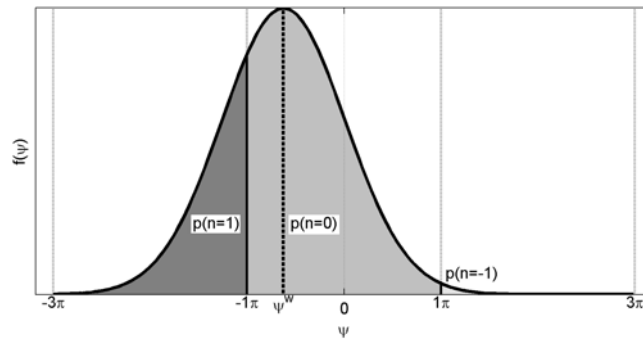Due to the fact that the double differenced phase is wrapped, the probability for $n = 0$ is always highest.



Figure 4.20: A-priori probability determination.

To avoid unnecessary effort in the Kalman filter update, only ambiguities where the a-priori probability exceeds a certain threshold are taken into account. This threshold should not be too limiting, e.g. between 0.1 and 0.01. In the next step, it has to be checked whether a spatially consistent solution for all arcs can be obtained with this choice of possible ambiguities, thus a spatial unwrapping is performed using MCF whereas the costs are computed by the a-priori probabilities according to equation 4.25. If no consistent solution is found, the variance is increased to increase the number of possible ambiguities until a consistent solution is found. Due to the increasing variance, the probability distribution slowly approaches an equal distribution and the number of possible ambiguities increases. The result of the spatial unwrapping leads to the a-priori unwrapped solution.
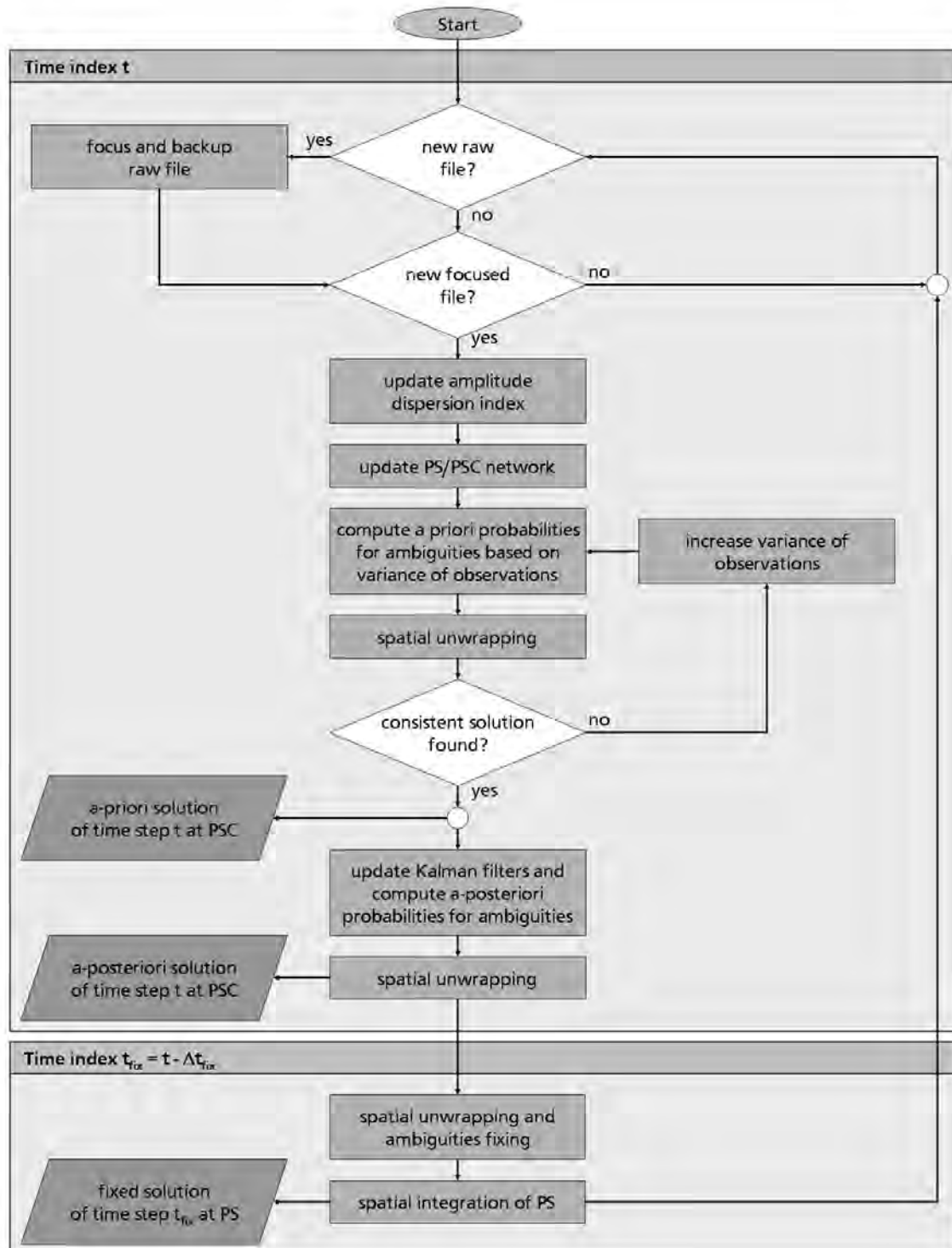
Figure 4.21: Real-time GB-SAR processing concept.

The next step is the Kalman filter prediction and update. The prediction is done for all existing Kalman filters at each arc. For the update, each Kalman filter is split according to the number of possible ambiguities introduced at this time index as described in section 4.2.3. Based on the differences between predicted and observed double differenced phase, the a-posteriori probability for each Kalman filter is computed. These probabilities are input for the spatial unwrapping, which now leads to the a-posteriori unwrapped solution.

The next step is the ambiguity fixing at time index $t_{fix}$, which is by $\Delta t_{fix}$ smaller than the time index of the current observation $t$. The choice for $\Delta t_{fix}$ should be made by estimating the temporal correlation of the decision for the ambiguities, as could be seen in Figure 4.12. But also the number of filters that can be handled should be considered, because a linear increase of $\Delta t_{fix}$ leads to an exponential increase of filters. The value $\Delta t_{fix}$ should thus be between 3 and 10. This means that the fixed solution is available with a delay of about $\Delta t_{fix} \cdot \Delta t_{samp}$, where $\Delta t_{samp}$ is the sampling time of IBIS-L. To fix the ambiguities, the a-posteriori probabilities for the different ambiguities at time step $t_{fix}$ are used as input into the spatial unwrapping. The result of the spatial unwrapping determines which Kalman filters are deleted. For better interpretation, the atmospheric effect should be removed by either meteorological data or filtering techniques.

Finally, the PSs can be integrated into the PSC network by spatial unwrapping. Only PSs in the direct vicinity to any PSCs should be integrated into the network. Otherwise, areas were no PSCs could be identified could adapt the movement of some PSCs further away, which might however not be correct. These areas, where no PSCs are available should rather be marked as not evaluable. The limit for the distance between a PSs and its corresponding PSC should not exceed the maximum arc length chosen for triangulation.

Due to the processing being a real-time method, the computation time for one time step must not exceed the sampling time of IBIS-L. On a Intel Core Duo CPU, 2.2 GHz the processing of 3000 arcs takes around 45 seconds including spatial unwrapping and ambiguity fixing. However, the computation time is highly dependent on the number of Kalman filters and thus on the data quality and the choice for $\Delta t_{fix}$. If the data is noisy and $\Delta t_{fix}$ is high, the number of Kalman filters in each time step increases and the processing will take longer.

In Figure 4.22, the availability of the different kinds of solutions is illustrated. The a-priori solution is available within a few seconds after the observation is finished because it is only based on the a-priori probabilities. The a-posteriori solution is available after the Kalman filter update, thus around a few seconds to minutes after the a-priori solution. The final/fixed solution, which takes into account following measurements to verify and correct the found a-posteriori solution, is available with a delay of around $\Delta t_{fix} \cdot \Delta t_{samp}$ after the observation is finished, so usually half an hour to hour later.
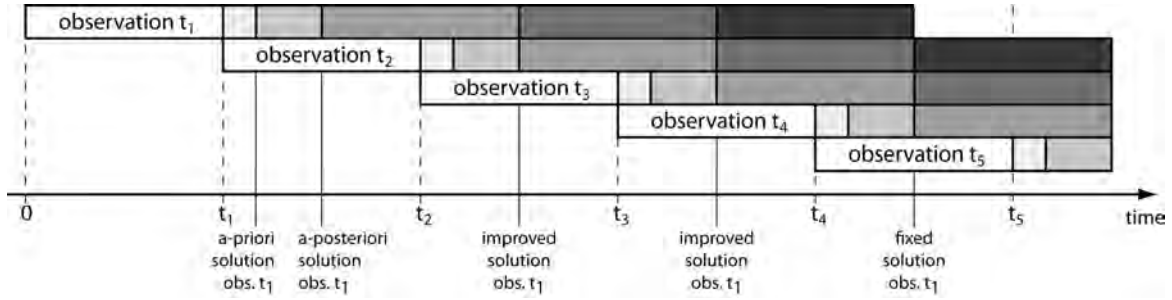


Figure 4.22: Availability of a-priori, a-posteriori and fixed solutions of an observation. The number of time steps until the solution is fixed is here 3.

# 5  Field Tests

Figure 5.1 gives an overview over the locations of the measurement campaigns carried out with IBIS-L and presented in the following sections. In all shown campaigns, additionally to IBIS-L, a weather station was installed in the vicinity of the IBIS-L station. Temperature, humidity and pressure were monitored with a Reinhard weather station DFT 1MV. The standard deviations that can be achieved are 0.3 °C for temperature, 0.8 hPa for pressure and 2 % for humidity.

The first test of continuous monitoring was done in summer 2008 in an active quarry in Dieburg, Germany, for five days. The place was selected to test the equipment in a suitable environment for continuous monitoring. Due to the quarry being active, the challenge in processing was here caused by the constant movement of trucks and other heavy machines around the quarry during day, which results in a high noise level. Processing conditions and results are shown in section 5.1.



Figure 5.1: Overview of the locations of the IBIS-L measurement campaigns.

The second test was performed in Bad Reichenhall, Germany, were a mountain side was monitored. The geophysical motivation for the selection of this place was the occurrence of earthquake swarms in this region (Kraft et al., 2006). The mountain side was observed continuously for 10 days in autumn 2008. Results are shown in section 5.2.

Within the Exupery project, a caldera flank on the island Sao Miguel, Azores, was monitored for about five months in summer 2009. Around Fogo volcano increasing seismic activity occurred (Wallenstein et al., 2007). Due to power supply difficulties and harsh weather conditions, only very little data could be gathered with moderate quality. The results of a few days of continuous monitoring are shown in section 5.3.

The last measurement campaign, presented in section 5.4, was carried out in Gries im Sellrain, located in Austria, within the KASIP project (Eichhorn and Schmalz, 2010). The landslide Steinlehnen, moving with an average rate of 20 mm/year, was observed for a period of about one month in summer 2010.

In Table 5.1, the specifications and processing settings of the four presented missions are shown. In all cases, the ADI selection thresholds for the determination of PSs and PSCs were chosen to be 0.25 and 0.1, respectively. The size of the segments for the PSC selection lies between $4 \times 4$ m$^2$ and $20 \times 20$ m$^2$. The given numbers of PSCs, arcs and triangles were computed using the first 30 images, as the numbers are varying with time. For processing, the same process model was used in all campaigns: a white noise acceleration model with a

acceleration standard deviation of $\sigma_a = 1$ mm/h$^2$. No prior information about the character of the displacements was given. The mean computation time per time step is in all cases far below the sampling rate. In Sellrain, the maximum computation time per time step exceeds with 8 min in one case the sampling rate of 6.5 min. The delay is caught up within the next observation. The number of images until the ambiguity solution is fixed was set to 5. So, after a period of $5 \times$ the sampling rate after the observation is finished, the fixed solution was available (see also Figure 4.22).

|  | **Dieburg** | **Bad Reichenhall** | **Sao Miguel** | **Sellrain** |
|---|---|---|---|---|
| **Country** | Germany | Germany | Azores | Austria |
| **Object** | Active quarry | Mountain side | Caldera flank | Landslide |
| **Time period** | 24.07.-01.08.2008 | 24.09.-03.10.2008 | 29.03.-28.08.2009 | 09.06.-08.07.2010 |
| **Number of images** | 1039 | 1452 | 3490 | 6085 |
| **Sampling rate [min]** | 5.5 | 8.5 | 10.0 | 6.5 |
| **Range limit [m]** | 22 - 320 | 1370 - 2220 | 730 - 1150 | 350 - 1600 |
| **Azimuth limit [rad]** | -0.5 - 0.5 | -0.3 - 0.3 | -0.25 - 0.25 | -0.35 - 0.35 |
| **PS ADI threshold** | 0.25 | 0.25 | 0.25 | 0.25 |
| **PSC ADI threshold** | 0.1 | 0.1 | 0.1 | 0.1 |
| **PSC segments size [m$^2$]** | $4 \times 4$ | $20 \times 20$ | $10 \times 10$ | $10 \times 10$ |
| **Max. arc length [m]** | 10 | 50 | 50 | 50 |
| **Number of PSs** | 13124 | 34998 | 7623 | 38132 |
| **Number of PSCs** | 525 | 765 | 142 | 1106 |
| **Number of arcs** | 1489 | 2205 | 376 | 3236 |
| **Number of triangles** | 942 | 1430 | 228 | 2126 |
| **Mean time / step [min]** | 0.6 | 0.5 | 0.2 | 2.0 |
| **Max. time / step [min]** | 2 | 3 | 1 | 8 |

Table 5.1: Processing settings of the IBIS-L measurement campaigns.

## 5.1 Quarry (Dieburg, Germany)

The quarry in Dieburg, Germany is still active and worked by the Odenwlder Hartstein Industry. Figure 5.2 shows a picture of the quarry with IBIS-L in front. The quarry was chosen as test object and was continuously monitored for five days in summer 2008. In total, 1039 images were gathered. Power supply was provided by solar modules and a generator. IBIS-L was mounted on a little basement consisting of two hollow concrete blocks, each of which weights 70 kg. To protect the instrument from weather, a little tent was built around it. As reference, two corner reflectors were installed, one at range 100 m and one at range 300 m.

The maximum range is only 320 m. The atmospheric component is expected to be low and the phase measurements should be easy to unwrap. The difficulty here lies in the fact that it is an active quarry and thus heavy machines, trucks and similar were constantly driving around during day causing a lot of noise. Furthermore, during the monitoring, the quarry was worked at daytime. In these regions, displacement monitoring is not possible, because the displacement due to digging exceeds the maximum unambiguous displacement that can be detected within one measurement. The coherence was lost there. The weather conditions were dry and hot: the temperature was around 30 to 35 °C during day and cooling down to 20 °C during night. In Figure 5.3 the observed data is plotted versus time. Between day 2.5 and 3 a sudden increase of humidity is visible, which occurred during heavy rainfall and also later between day 3 and 3.5 it was raining.

For the initial determination of the PS and PSC network, the ADI was computed using the first 30 images. Figure 5.4a shows the computed ADI. For better orientation, some features are marked. The ADI is lowest at solid rock due to the good reflectivity properties. At the backmost almost vertical wall, the ADI is somewhat higher caused by the vegetation that covers the wall. The road has a significant higher ADI as the material is finer there leading to a worse reflectivity. During these 30 images, the quarry was being worked, which can be seen at the far end of the working area where the ADI rises to 2.5. In Figure 5.4b, the histogram of the ADI is shown. There is a peak at 0.5, which is expected as this is the theoretical limit for the ADI for constant noise and signal power. But there exist also a lot of pixels with an ADI far beyond 0.5, which is a sign for strong variations of amplitude and noise power.

The ADI threshold for the PS selection was set to 0.25 and by that 13124 PSs were identified (see Figure 5.5a). To select the PSC subset, a ADI threshold of 0.1 was chosen with a segment size of $4 \times 4$ m$^2$. For the initial

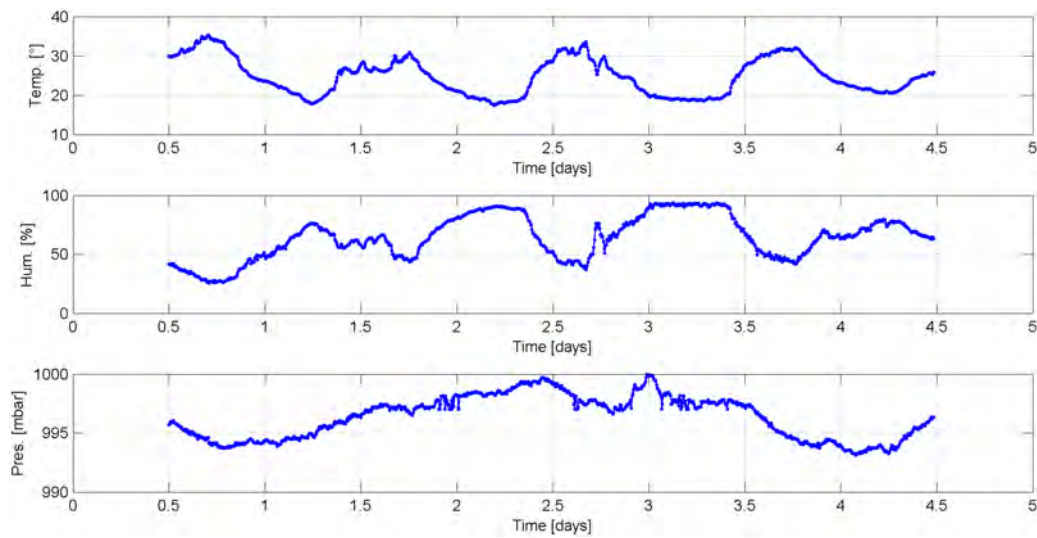Figure 5.2: Picture of the quarry in Dieburg, Germany.



Figure 5.3: Meteorological data gathered during monitoring in Dieburg, Germany.

ADI image, 525 PSCs were identified. The triangulation of the PSC network resulted in 1489 arcs and 942 triangles (see Figure 5.5b). In the processing, every 15 images, the PSC selection changed by updating the ADI. For the new ADI computation always the previous 30 images were used. The number of PSC is here extremely dependent on quarry working hours and a lot of PSC vanished during day.

Figure 5.6 shows the unwrapped cumulated displacement at the PSs observed during the whole monitoring period. The displacements are corrected for atmosphere using meteorological observations only. Negative displacements are movements towards the radar, and positive away from the radar.

Significant displacements occurred at a hill of gravel (marked as hill of gravel 1) that are caused by down sliding material, mainly triggered during day due to machines driving around or due to rain. Figure 5.7a shows the time series of the displacements at two selected PSs located at the hill of gravel. The highest displacements occurred during a rain period. At the PSs near to the radar a displacement towards the radar can be observed and vice versa at the PSs further away from the radar. The PSs moving away from the radar are located at the top of the hill of gravel, while the PSs moving towards the radar are at the foot of the hill. Thus, material from the top was flowing downwards. The hill of gravel broadened slightly. At the second hill of gravel no

(a)  (b)
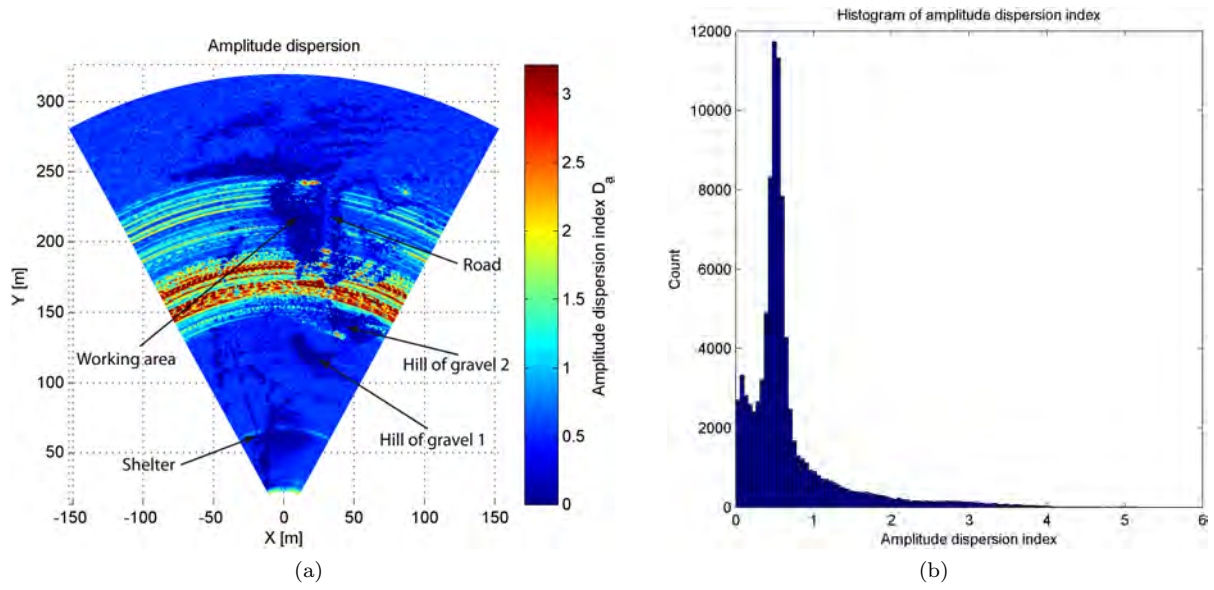
Figure 5.4: Computed ADI and ADI histogram in Dieburg, Germany.
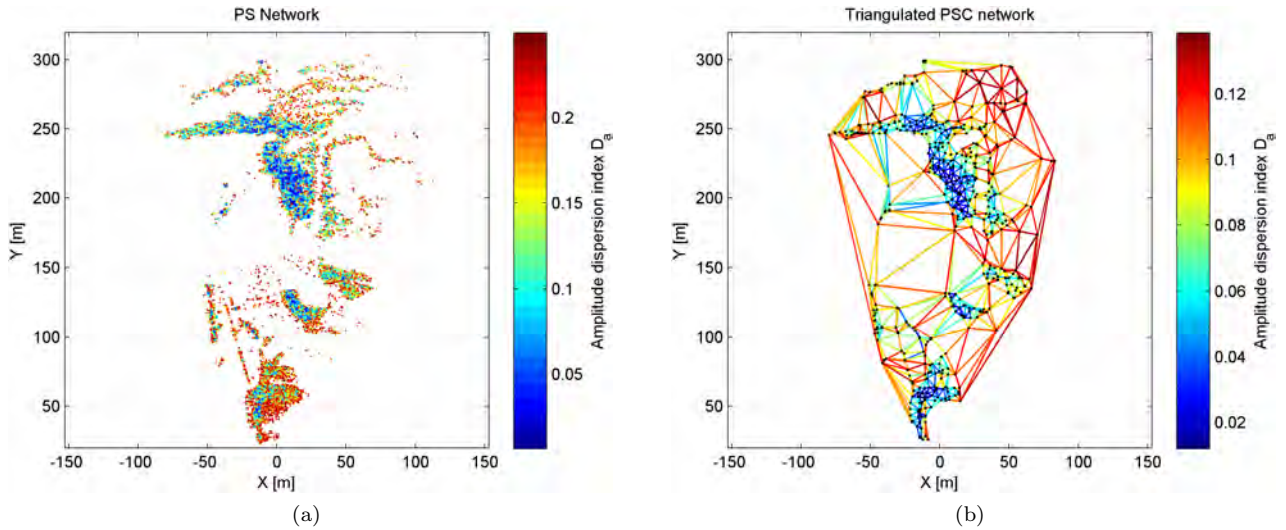


(a)  (b)

Figure 5.5: Selected PS and triangulated PSC network in Dieburg, Germany.

displacement could be observed, which is verified by looking at the time series (Figure 5.7b).

In Figures B.1 and B.2 in the Appendix, displacements separated in day and night can be inspected. The quality difference between day and night is very clear. During day only a very little number of PSCs could be identified in the working area. Thus, in this area the observed displacements during day are rather unreliable as the velocity of digging was too fast to be observed with IBIS-L. Furthermore, the measurements in this area were disturbed considerably by the digging itself. In Figure 5.7c, the time series of two PSs inside the working area are displayed. The increasing noise during day is obvious. Nevertheless, mainly during night a significant displacement towards the radar could be observed.

In all time series and also in the daily displacement maps, at time index 3.0 (night 30. to 31.07.2008) increasing noise and consequently an increasing number of unwrapping errors can be observed. During this time it was raining heavily. At the vertical walls at the back of the quarry, significant displacements could be observed during this time (Figure 5.7d). At first, there is a displacement of around -4 mm. It is very unlikely that this jump is caused by unwrapping errors as unwrapping errors could be identified by sudden jumps of around 8 mm. However, the true displacement might by larger than 4 mm, as sudden displacements cannot be monitored. Shortly after, a sudden displacement of +4 mm can be detected. Except for this short time period, no significant
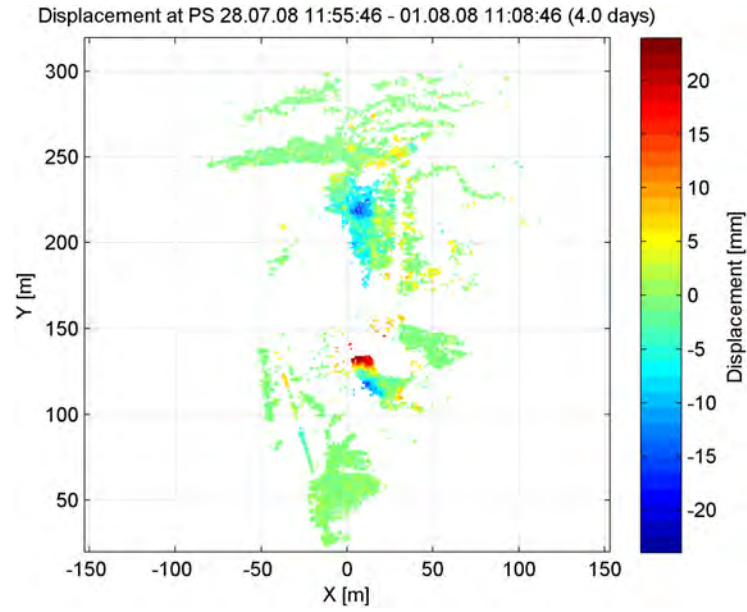
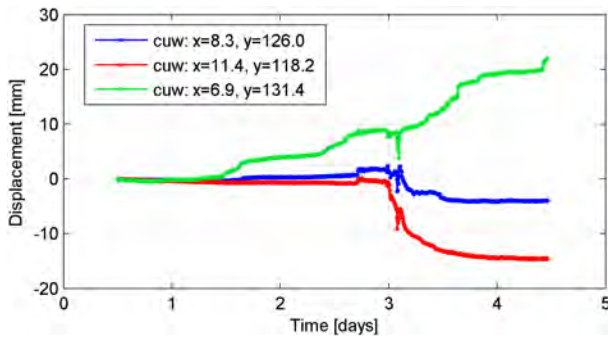Displacement at PS 28.07.08 11:55:46 - 01.08.08 11:08:46 (4.0 days)
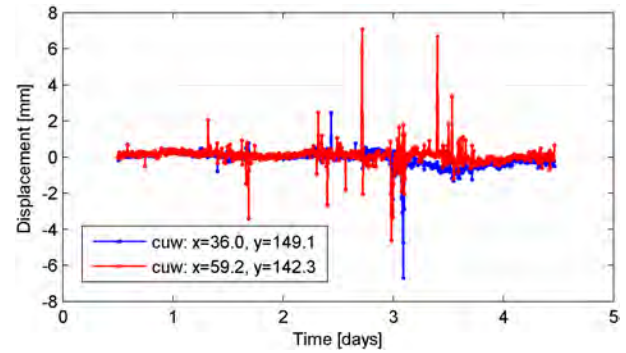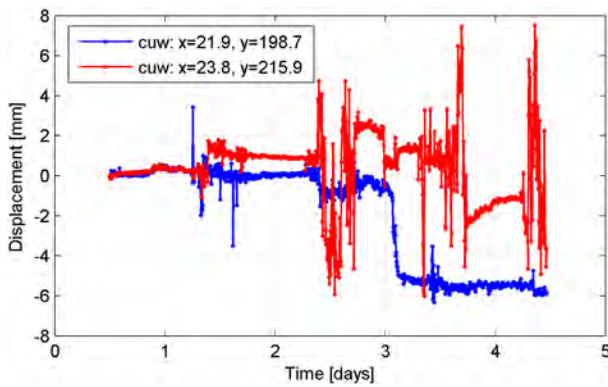


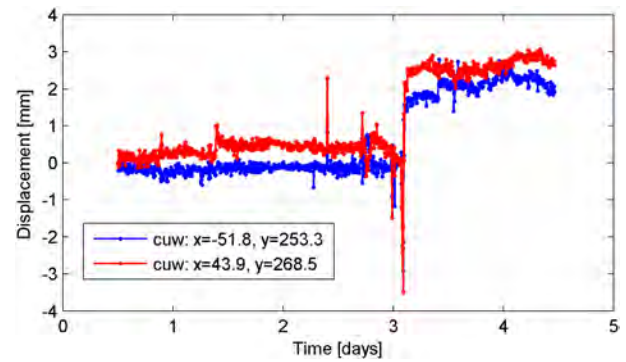Figure 5.6: Unwrapped displacements in Dieburg, Germany



(a) PSs at hill of gravel 1.



(b) PSs at hill of gravel 2.



(c) PSs in the working area.



(d) PSs at the back wall.

Figure 5.7: Displacement time series of selected PS in Dieburg, Germany. Day 0 stands for date 28.7.2008 0:00.

displacements could be observed at the quarry walls.

## 5.2 Mountain Side (Bad Reichenhall, Germany)

Mount Hochstaufen (1775 m) is located northwest of Bad Reichenhall, Germany. The mountain side was mainly chosen as test object to determine how atmosphere can influence the quality of the measurements under difficult circumstances (e.g. large heights differences, cloud cover). Furthermore, an investigation of mass movements was done, due to the occurrence of earthquake swarms triggered by strong rainfall events (Kraft et al., 2006).

The mountain side was observed for about 10 days end of September 2008 and 1452 images were gathered. IBIS-L was positioned at Padinger Alm (670 m). Figure 5.8 shows a picture of the monitored mountain side, partly covered by clouds with the IBIS-L sensor in front. A tent was built around IBIS-L and mains power was available during the whole measurement period.



Figure 5.8: Picture of the mountain side in Bad Reichenhall, Germany.

Additionally to IBIS-L, a meteorological sensor was installed at Padinger Alm. The weather conditions were rather wet. It was raining often and the last day of observation it started snowing at the mountain top. Due to the steep look angle and the fact that only one weather sensor was used, the meteorological data could only roughly give an idea of the atmospheric phase. Furthermore, the mountain was often covered in clouds. The main atmospheric disturbance comes from humidity and thus cloud cover and fog is problematic. It is impossible to estimate this effect by the use of weather data observed at few distinct points.

For the ADI computation, the first 30 images were used (see Figure 5.10). With a threshold of 0.25, 34998 PS were selected as shown in Figure 5.11a. For the PSC network, a threshold of 0.1 was used, with a segment size of $20 \times 20 \text{ m}^2$. Initially, 765 PSC could be identified with 2205 arcs and 1430 triangles (see Figure 5.11b).

Figure 5.12 shows the unwrapped cumulated displacement at the PSs observed during the whole monitoring period. The atmospheric phase is estimated from the observed phase assuming constant atmospheric properties along the path. Stable PS were identified by correlation with the weather data. It can be seen that there is still a spatially low frequency signal left, which is very probably caused by atmosphere. During the whole monitored period no significant displacement could be detected. There are some probable unwrapping errors visible, but these errors occur only at PSs with temporally high noise due to cloud cover or rain and do not cumulate with time. The number of errors does not increase with time. Figure 5.13 shows the displacement time series of some selected scatterers along a profile.
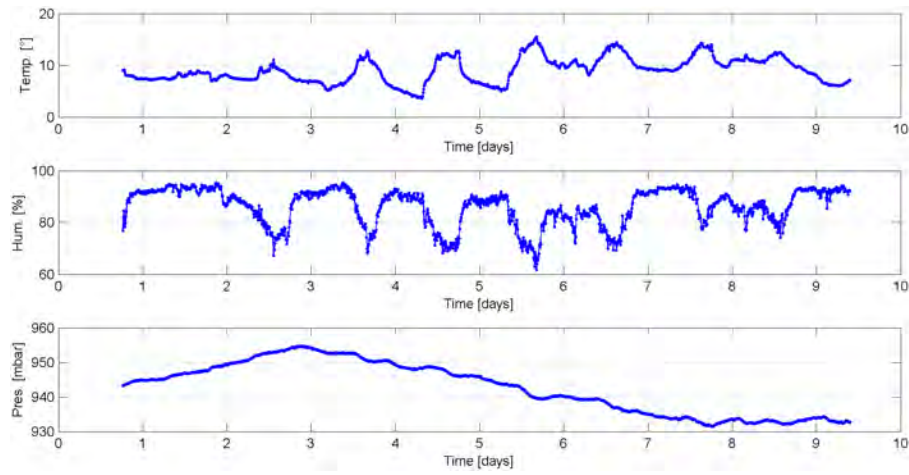
Figure 5.9: Meteorological data gathered during monitoring in Bad Reichenhall, Germany.
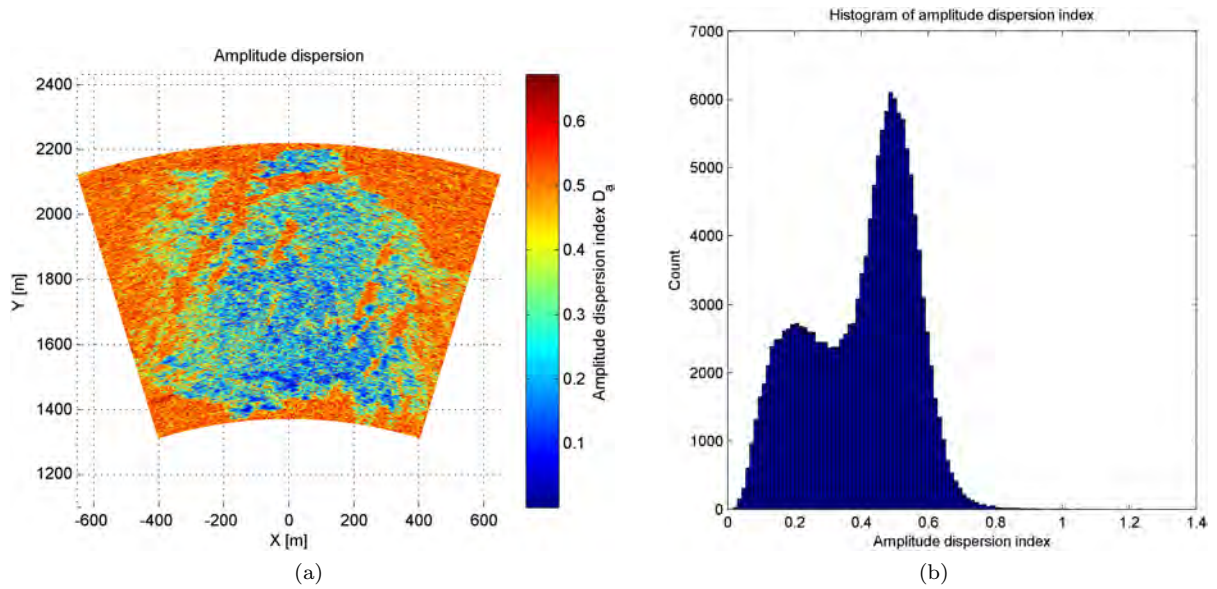


(a)                                          (b)

Figure 5.10: Computed ADI and its histogram in Bad Reichenhall, Germany.
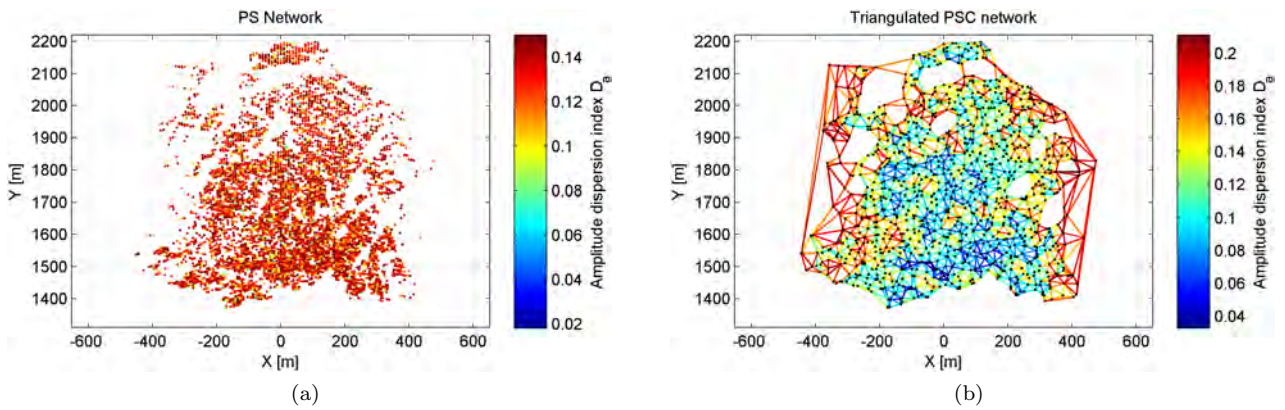


(a)                                          (b)

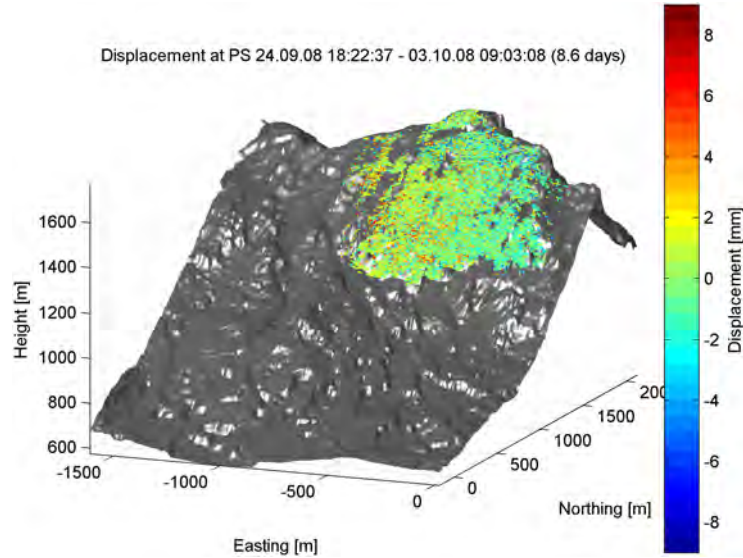Figure 5.11: Selected PS and triangulated PSC network in Bad Reichenhall, Germany.

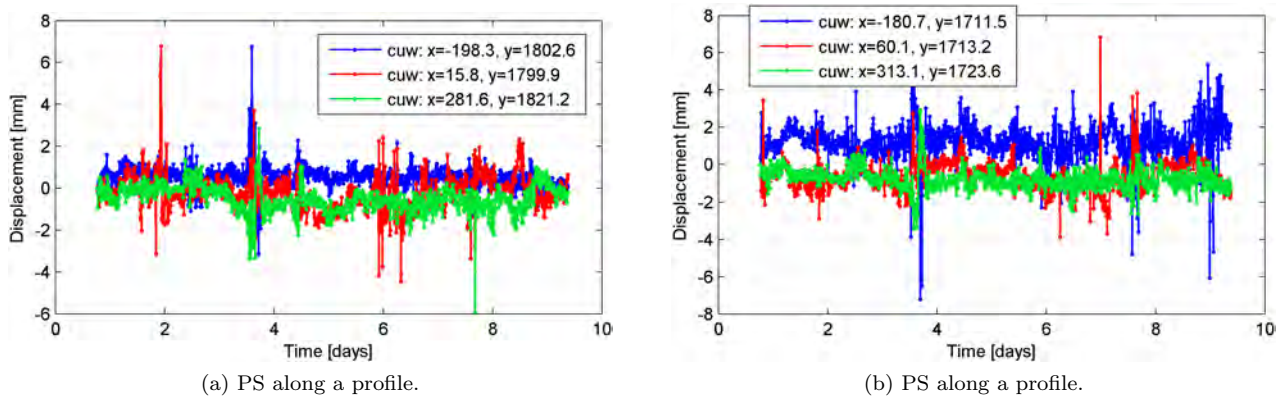Figure 5.12: Unwrapped displacements in Bad Reichenhall, Germany



(a) PS along a profile.



(b) PS along a profile.

Figure 5.13: Displacement time series of selected PS in Bad Reichenhall, Germany. Day 0 stands for date 24.9.2008 0:00.

## 5.3  Caldera (Sao Miguel, Lagoa de Fogo, Azores)

The monitoring of Fogo volcano on island Sao Miguel, Azores was done within the Exupery project funded by the BMBF. The fundamental goal of Exupery was the development of a Volcano Fast Response System (VFRS), to be able to respond rapidly to a volcanic crisis (Hort, 2009). It consisted of five main working groups: the ground based observations, the satellite based observations, the database development and visualization, the physical modelling and the project coordination. To be able to asses the state of the volcano in near real-time, all gathered data should be transferred online to a central database by means of intelligent wireless communication methods. The monitoring with IBIS-L was part of the ground based observations work package. In preparation of this project, the test measurements presented in the last sections were carried out to test the equipment and define necessary improvements.

 The final step of the development was the field test, performed at Fogo volcano between end of March to end of August 2009. Tectonically, the Azores are located at a triple junction between the North American, Eurasian and African plate (Searle, 1980). Fogo volcano is the largest of the three volcanoes on Sao Miguel and is located in the center of the island. The last eruption occurring at Fogo volcano was in the year 1563 (Silveira et al., 2003). Seismic swarms are a recurring phenomena on the island. At the end of 2002, the seismic activity was increasing and reached its maximum in 2005 (Wallenstein et al., 2007). A flank of the crater at Fogo volcano was chosen to be monitored with IBIS-L. Figure 5.14 shows a picture of this area from across the crater lake were IBIS-L was installed.

 As basement, a poured concrete foundation was made and a wooden shelter was built to protect the instrument
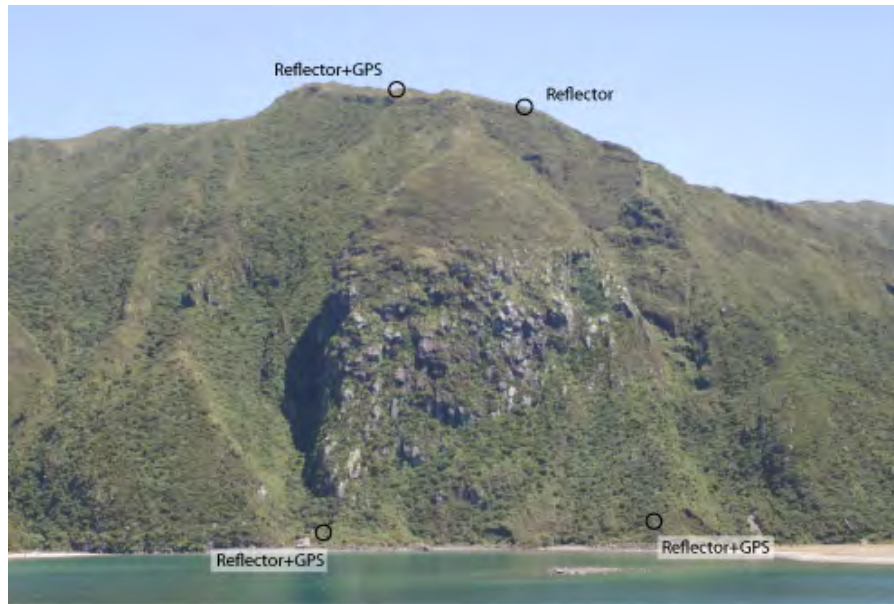
Figure 5.14: Picture of the volcano flank on Sao Miguel, Azores.

from weather and vandalism. In the front, acrylic glass was attached to the housing which the radar can penetrate. No mains power supply was available and therefore solar modules were used. Due to the extremely wet climate during the summer on the Azores only little sun was available to provide IBIS-L with power and IBIS-L worked only in 15 % out of the total monitoring period. Additionally to IBIS-L, four corner reflectors, partly equipped with low-cost single-frequency GPS receivers, were installed inside the monitored area. In the near vicinity, two dual-frequency receivers were established in the stable region, acting as reference stations for the evaluation of the GPS data. Furthermore, a meteorological sensor and a webcam were installed at the radar station.

By the use of meshnodes equipped with WLAN antennas distributed in the field at the GPS and IBIS-L stations, it was possible to access every station through internet and each station could send the gathered data to the database. However, the connection was slow and unstable due to the mentioned power supply problems. The processing of the data was directly done in the field to reduce the size of the files to be sent as much as possible. The raw data was stored on hard disks in the field.

Due to the climate being very humid and the use of acrylic glass in front of the sensor, the signal was dampened significantly, which leads to a lower ADI. To be able to select an initial set of PSs, the ADI was computed from 30 selected images observed during night as the ADI generally tends to be better at night. In Figures 5.15a and 5.15b, the computed ADI and its histogram are shown. For comparison, Figures 5.15c and 5.15d show a very typical ADI distribution using images that were observed during day. Only a very low number of scatterers can be identified as PSs here. These scatterers are mainly located in the rock face. In the upper part, where vegetation covers most of the ground, the scatterers disappear during rain or when the dampening due to atmosphere is high. This fact is a limitation of GB-SAR and can only be improved by installing corner reflectors in these regions.

Exemplary, here only the results of processing 963 images observed from 20.8. to 27.8.2008 are shown, which is the longest continuous measurement with IBIS-L that could be gathered. Figure 5.16 shows an overview of the weather conditions during this period. The humidity never falls below 60 %. This might be amplified due to IBIS-L being located near a lake. The radar waves were in fact crossing the lake. Especially, when the sun is shining and water evaporates from the lake it is impossible to capture this effects with weather stations. On the webcam pictures it could be observed that IBIS-L was very often surrounded by dense clouds and fog.

For processing, 7623 PSs and 142 initial PSCs could be identified by thresholding on the ADI shown in Figure 5.15a using a PS threshold of 0.25 and a PSC threshold of 0.1 and segment size of $10 \times 10$ m$^2$. By triangulation, 376 arcs and 228 triangles were formed. The initial PS network and PSC triangulation is shown in Figure 5.17. Looking at Figure 5.15c, it can be imagined how the number of PSC will be varying during processing. In the worst case, the number of PSC drops down to 8, which leads to a very low reliability of the results, especially in the areas covered with vegetation. Increasing the PSC threshold will not improve the reliability of the results, as the higher noise level could cause more unwrapping errors.
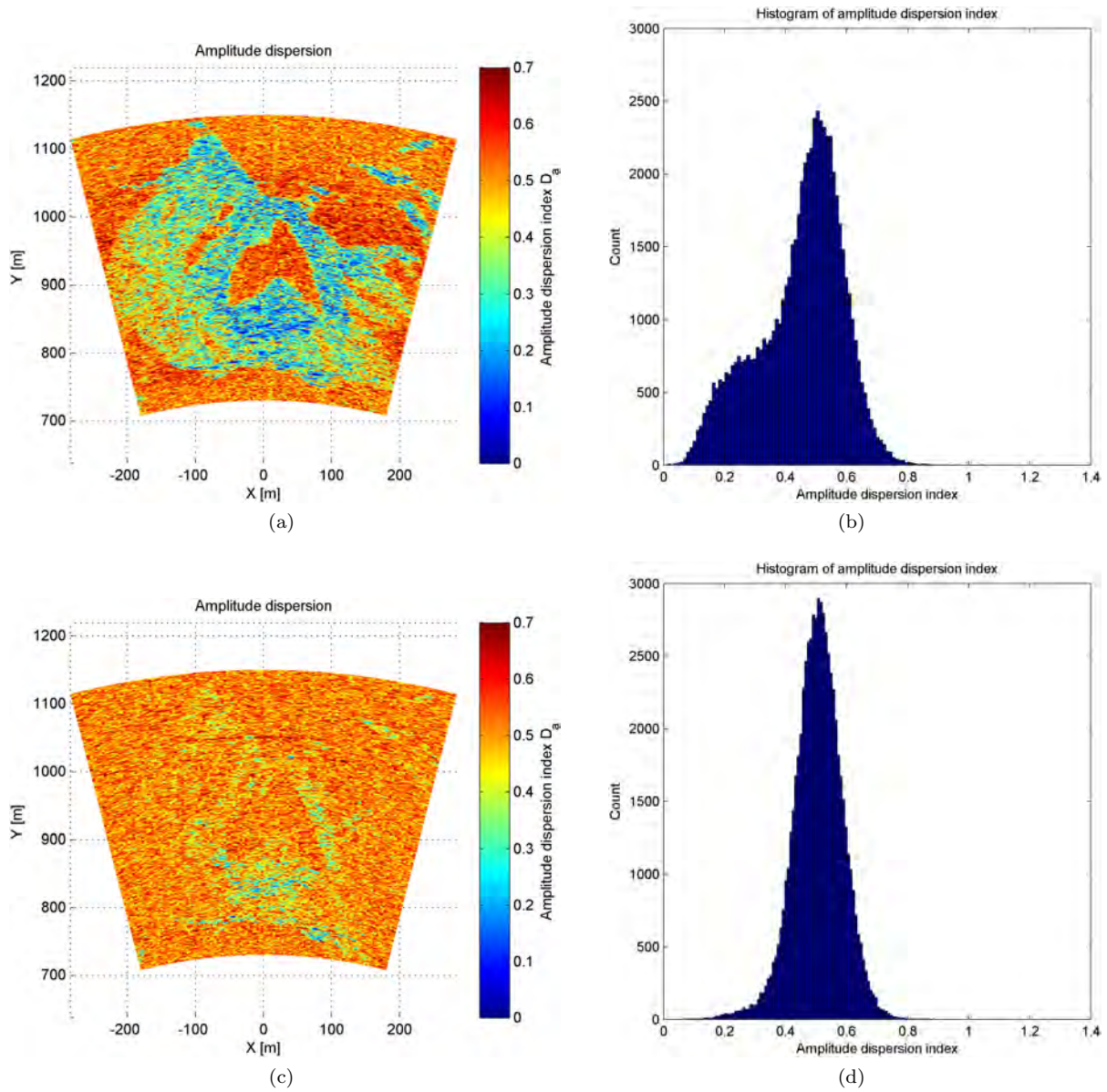
Figure 5.15: Computed ADI and its histogram on Sao Miguel, Azores. The ADI in the upper graphs was computed using images observed during night, in the lower graphs during day.

In Figure 5.18, the unwrapped displacement for selected monitoring period is shown. The atmospheric correction was done by selecting stable PS found by correlation with the weather data. No significant displacement could be detected. This result conforms with the outcomes of the GPS measurements and spaceborne SAR done within the work package 2 (satellite based observations) of the Exupery project. As mentioned before, the reliability of the data in the vegetated areas is questionable, which is, however, a known limitation of GB-SAR.

In Figure 5.19, displacement time series are shown. The time series of the reflectors show some jumps at time index 1.5 (Figure 5.19a) and time index 3 Figure 5.19b. The first jump is caused by work at the reflector station. The cause of the second jump is unknown. It cannot be introduced by false unwrapping, as the jump would then be around 8 mm. At time index 6.5, the noise of the two upper reflectors is suddenly increasing. This is because, the stations were dismantled at that time. During this time the two reflectors were deleted from the list of PSC due to the sudden increase of ADI. Figures 5.19c and 5.19d show PS located at the rock face and somewhere in the vegetated area, respectively. The different noise levels at rock and vegetation are obvious. As expected the measurements at the rock face appear less noisy.
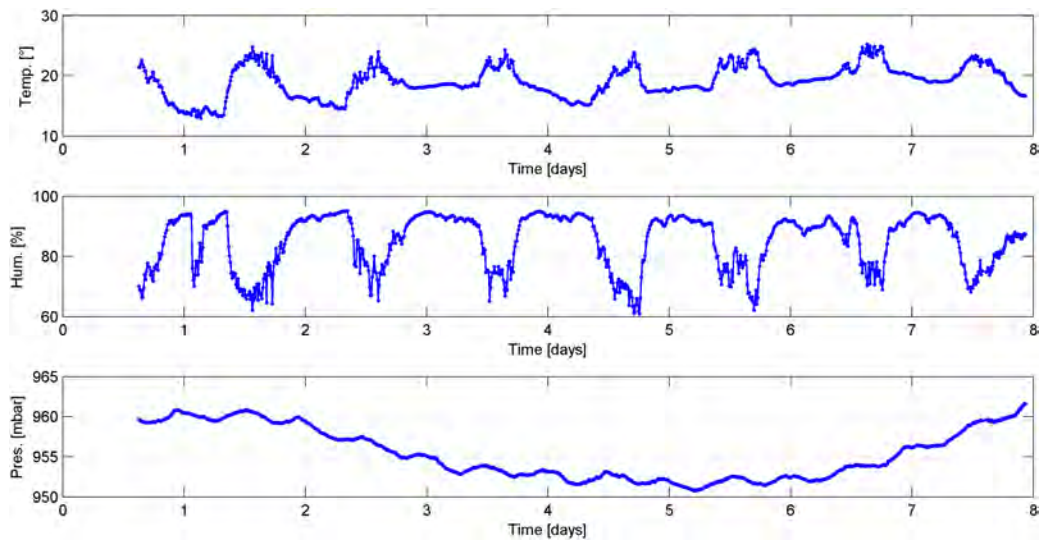
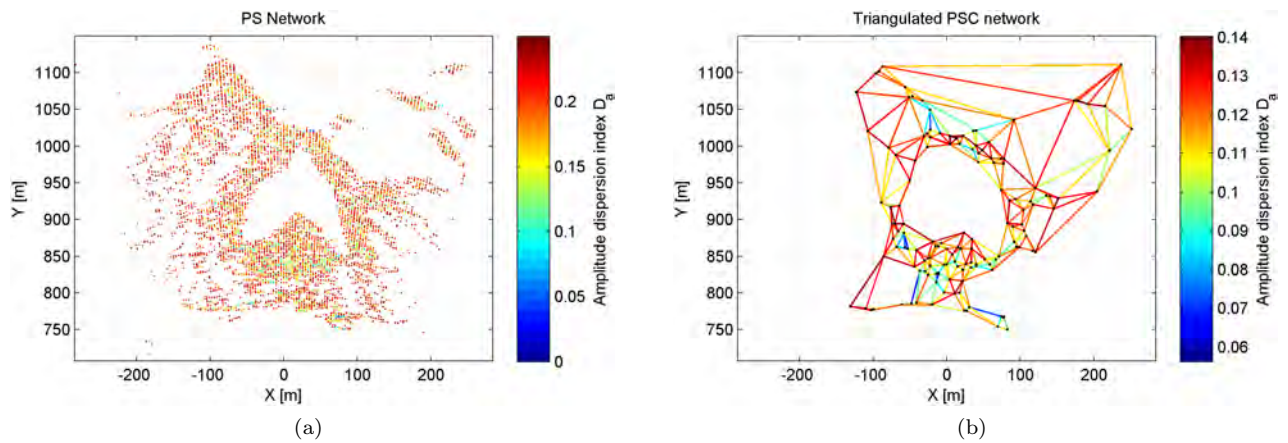Figure 5.16: Meteorological data gathered during monitoring on Sao Miguel, Azores.



(a)                                                                            (b)
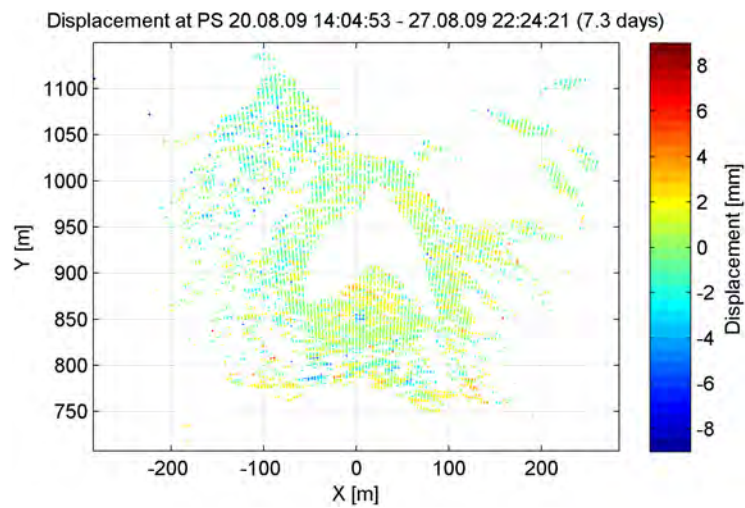
Figure 5.17: Selected PS and triangulated PSC network on Sao Miguel, Azores.



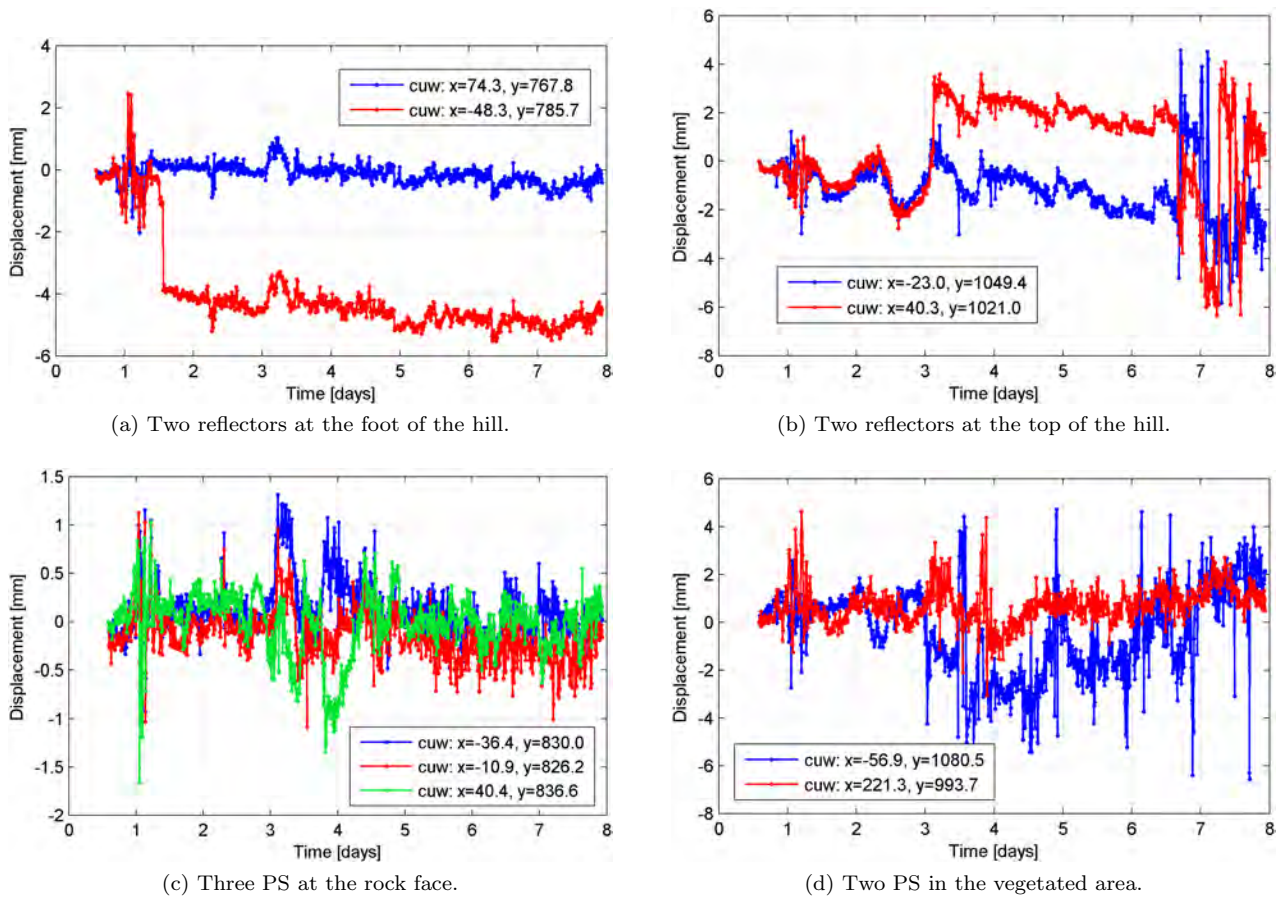Figure 5.18: Unwrapped displacements on Sao Miguel, Azores.

(a) Two reflectors at the foot of the hill.


(b) Two reflectors at the top of the hill.


(c) Three PS at the rock face.


(d) Two PS in the vegetated area.

Figure 5.19: Displacement time series of selected PS on Sao Miguel, Azores. Day 0 stands for date 20.8.2009 0:00.

## 5.4 Landslide (Gries im Sellrain, Austria)

The KASIP (Knowledge-Based Alarm System with Identified Deformation Predictor) project is funded by the Austrian Science fund FWF. Partners are Darmstadt University, Vienna University and alpS, the Austrian center for natural hazards. The goal of the project is the combination of observations with numerical modelling to simulate and predict critical situations at mass movements (Eichhorn and Schmalz, 2010; Schmalz et al., 2010). As study object, the landslide Steinlehnen in Gries im Sellrain, near Innsbruck, Austria, was selected.

In 2003, the landslide became highly active with a total displacement of around 15 to 27 m (Zangerl et al., 2007). With it, the number of rockfalls increased significantly. As a result, a laser scanner was installed opposite to the slope to monitor the movements. When the activity decreased, reflectors for monitoring with a total station where mounted in the active zone. At first, monthly measurements were carried out, later annually, which now show a movement of around 20 mm/year. Due to rockfalls and the constant landslide movement, many total station reflectors, especially in the active zone, were lost. Figure 5.20 shows a picture of the landslide.

In summer 2010, IBIS-L was installed at a height of 1300 m opposite to Steinlehnen and monitored the slope for about one month. The top of the landslide is at a height of 2000 m. IBIS-L was mounted on two concrete blocks and a wooden shelter protected it from rain. In contrary to the Azores, no acrylic glass was placed in front of the radar to reduce the damping effect. Additionally, a meteorological station and webcam were installed. Power supply was provided by solar modules and a generator.

In Figure 5.21, the meteorological data is displayed. The measurement started during sunny weather with temperatures up to 30 °C. At day 4, it began raining and the landslide was covered in clouds most of the time. At day 11, the temperatures dropped down to zero degrees and the rain became snow. Four a few hours, IBIS-L and the landslide were covered with snow. The snow melted completely at the same day it fell when the temperature rose. After that is was sunny again. In the last days, some problems with the power supply occurred and data for a few hours is missing. Apart from that, IBIS-L worked continuously.
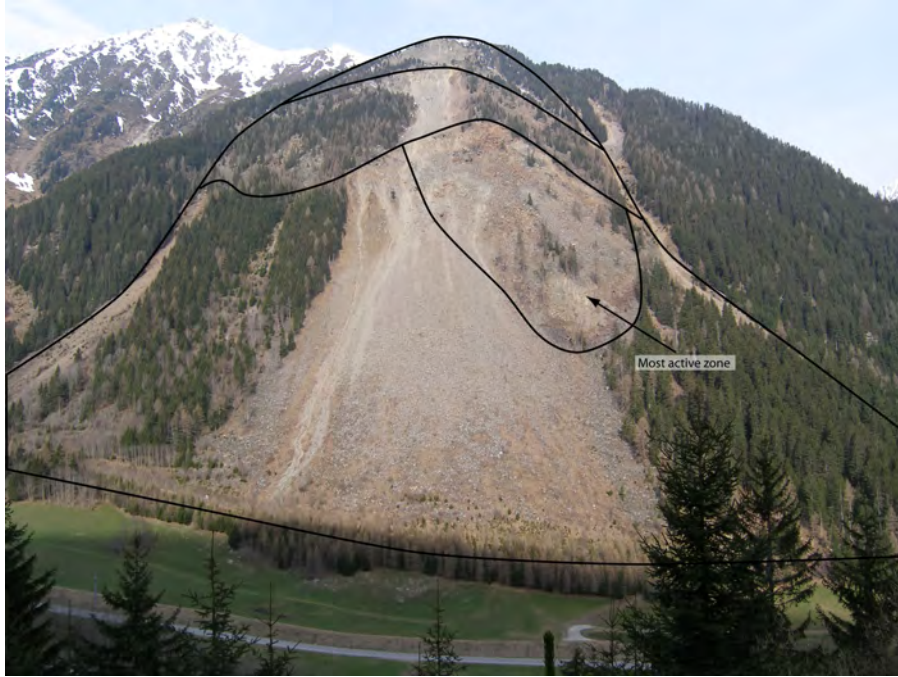
Figure 5.20: Picture of the landslide Steinlehnen in Gries im Sellrain, Austria. The black lines indicate scarp boundaries after Zangerl et al. (2007).
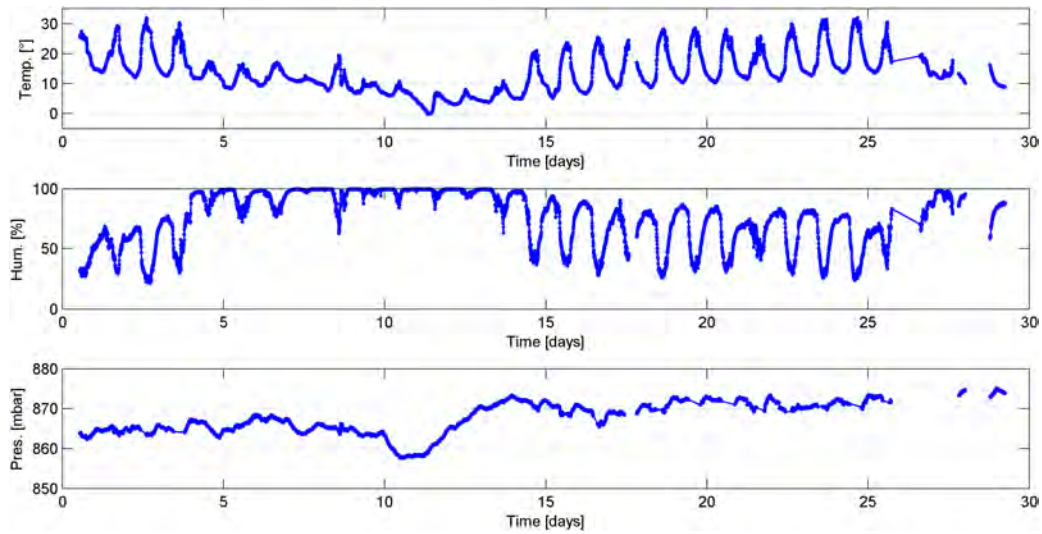


Figure 5.21: Meteorological data gathered during monitoring in Gries im Sellrain, Austria.

For the selection of the PSs and PSCs, the ADI was computed using the first 30 images (see Figure 5.22). For better orientation, the scarp boundaries are indicated according to Zangerl et al. (2007). The PS selection was done with a ADI threshold of 0.25 which results in 38132 PS. Initially, 1106 PSC were identified with a PSC threshold of 0.1 and a segment size of $10 \times 10$ m$^2$. The selected PS and triangulated network are displayed in Figure 5.23.

Figure 5.24a shows the cumulated displacements observed during period 9.6. to 8.7.2010 projected onto a DEM. The atmospheric correction was done by selecting stable scatterers by correlation with the weather data. The active zone can be clearly identified with a significant higher displacement in the center. The total displacement is almost 12 cm towards the radar. The line of sight almost corresponds with the true direction of movement as determined by a total station. In Figure 5.24b, 5.24c and 5.24d, the total displacement is split into the period 9.6. to 20.6.2010, day 20.6.2010 and 20.6. to 8.7.2010, respectively.

In the first few days, displacements of up to 2 cm towards the radar were observed. Rock falls happened frequently mainly in the lower part of the landslide. This leads to several unwrapping difficulties and many
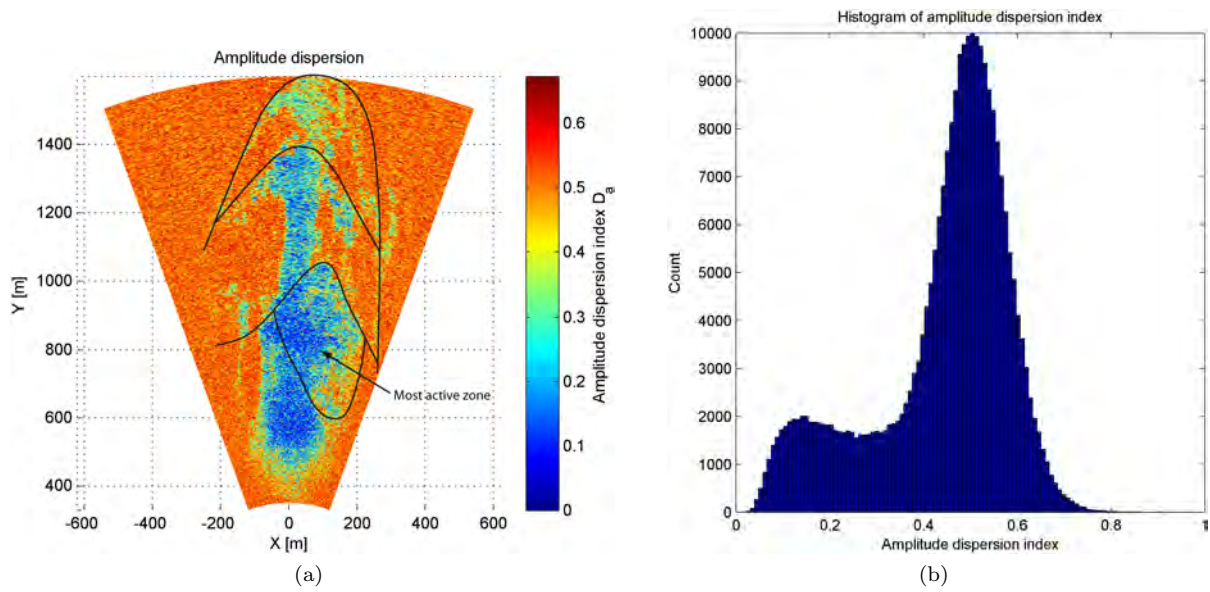
Figure 5.22: Computed ADI and its histogram in Gries im Sellrain, Austria. The black lines indicate scarp boundaries after Zangerl et al. (2007).
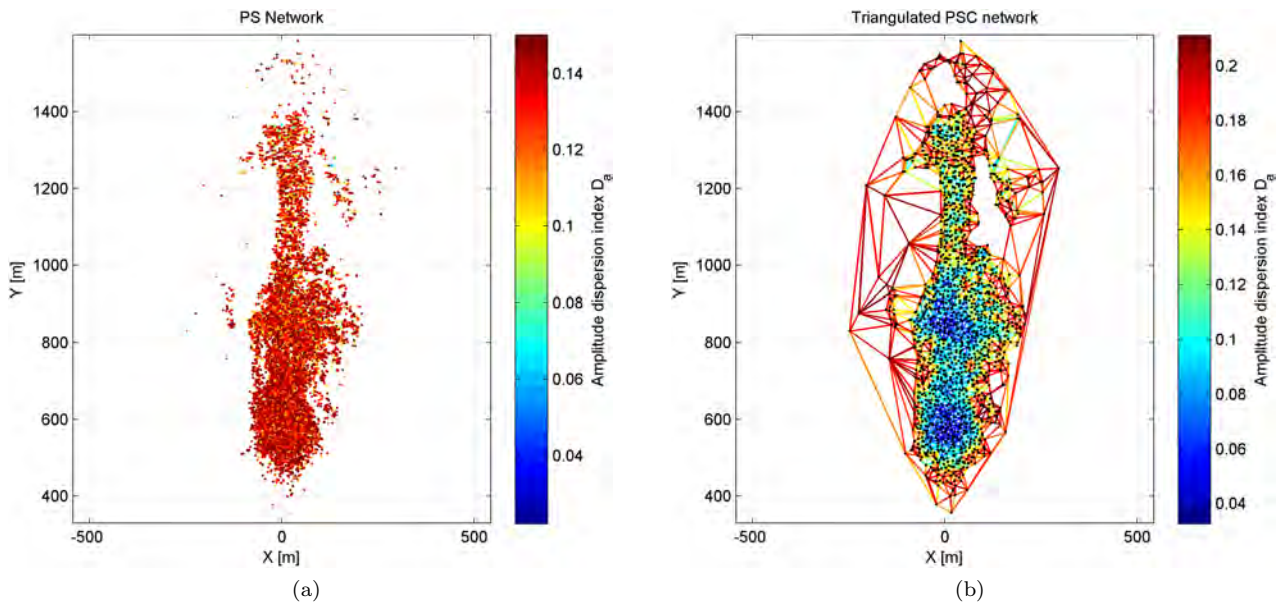


Figure 5.23: Selected PS and triangulated PSC network in Gries im Sellrain, Austria.

PSCs were deleted. Due to the network update being done every 15 images based on the last 30 images, the sudden occurrence of a rockfall does not lead to an immediate removal of the affected PSCs. Thus, the noise is temporally increasing until the PSCs are deleted. During the 20.6.2010, snow was falling and the mountain top was covered with snow for a short time period. During this time, no displacement monitoring was possible in this area as snow changes the reflectivity properties of the surface. Thus, almost no PSC remained on the mountain top. When the snow melted a few hours later, the PSCs were reinstated.

In Figure 5.24c, it can be seen that the maximum displacement during the 20.6.2010 was around 3.5 cm towards the radar in the center of the landslide. During the period 20.6. to 8.7.2010, the displacement in the active zone was up to 9 cm towards the radar.

In Figure 5.25, time series of selected PSCs are shown. Figure 5.25a shows the time series of five PSC along a 100 m-profile through the most active zone. In Figure 5.25a, the time series of two PSCs at the upper border of the active block are presented. The PSCs are about 20 m apart, one being located on the active block and the

(a) Total displacement
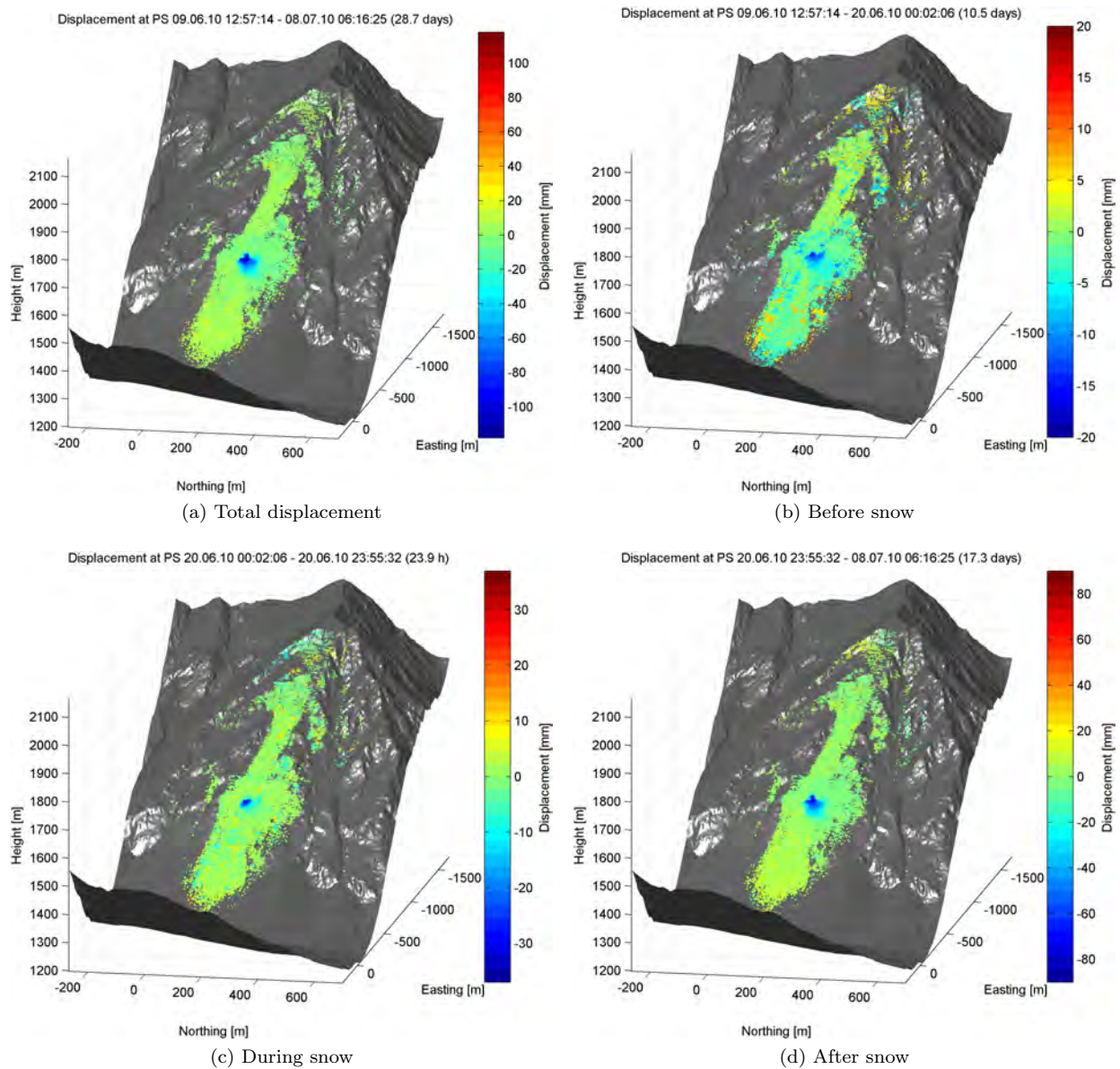
(b) Before snow

(c) During snow

(d) After snow

Figure 5.24: Unwrapped displacements projected onto a DEM in Gries im Sellrain, Austria.

other on the stable block above. A sudden increase of velocity at time index 12.0 (day 20.6.2010) is obvious. This coincides with the drop of temperature to 0 °C. Before that day, it was raining a lot. When the rains started, a slight velocity increase is visible as well (time index 5.0). After a few days, the movement slowed down again.

As already mentioned, many rockfalls took place, especially during the active period. Displacements induced by a rockfall cannot be observed as the falling rocks cause displacements that exceed a quarter of a wavelength. However, the origin and time can be determined by regarding the occurrence of sudden noise in a distinct area as sign for a rockfall. Looking at the wrapped interferograms of two consecutive images, such events can be clearly identified. Also the magnitude can be estimated by determining the size of the area that is affected. The events shown in Figure 5.26 were of higher magnitude as they were also heard and reported by local residents.

In Figure 5.27, a histogram of the rockfall events during the increased activity around 20.6. is displayed. These are only events that were visible in the wrapped interferograms. It is obvious that the number of rockfalls is increasing during a period of higher activity. But also before the strong increase at 20.6., the rockfall frequency is increasing. Further study should be done on this matter by comparing the results found here to seismometer measurements at the slope.
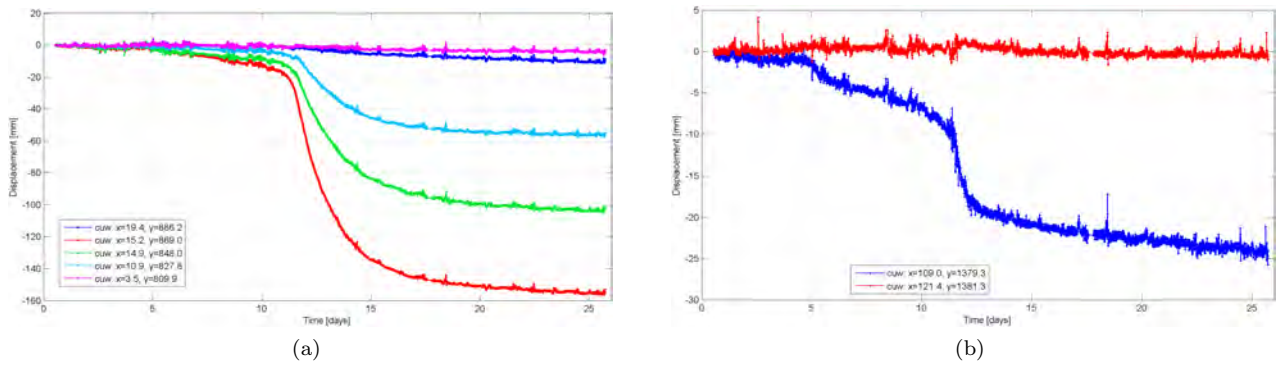
Figure 5.25: Displacement time series of selected PS at Steinlehnen, Austria. Day 0 stands for date 9.6.2010 0:00.
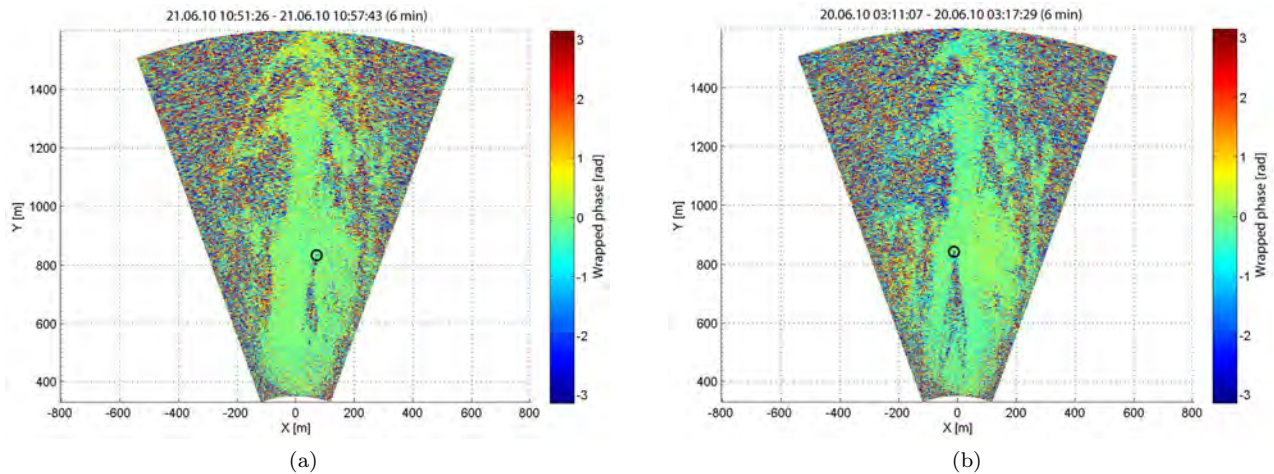


Figure 5.26: Wrapped interferograms of rockfall events occurring at Steinlehnen, Austria. The origin is marked by a black circle.
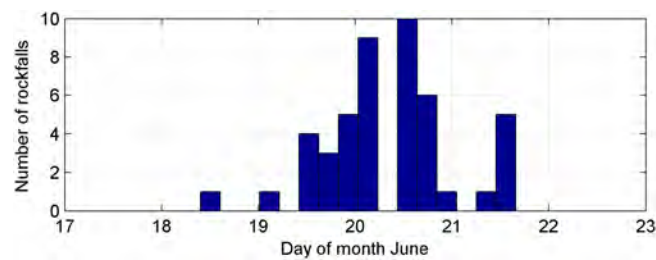


Figure 5.27: Histogram of rockfall events during high activity observed with IBIS-L.

# 6 Conclusion and Outlook

The objective of this thesis was the development of a near-real-time processing concept to be able to derive displacements with the least delay possible from GB-SAR measurements. Real-time processing can help in the assessment of the state of a mass movement online for e.g. early warning applications. Decorrelation and phase unwrapping problems, mainly following from atmospheric effects, prevents the direct analysis of interferograms with the standard InSAR approach. In chapter 4, a real-time method for processing GB-SAR images has been described thoroughly. It relies on the fact that even in very noisy interferograms, single PS can be identified, which keep a good quality over time. Instead of processing each interferogram, the time series of these PSs are analysed.

The most important processing step is the phase unwrapping. For each arc, several Kalman filters exist, each of which represents one ambiguity solution. By analysing the difference between predicted and observed phase, probabilities for each filter to be the correct one can be computed. Based on these probabilities a spatial unwrapping is performed to make sure that the found solution is spatially consistent. With each new observation that is added, the probabilities are reevaluated and the reliability of this ambiguity determination increases. By that, the delay until a first estimation for the displacements can be given is a few seconds to minutes after the observation is finished. The correlation between past ambiguity decisions and the new observation becomes less with passing time and the ambiguities can be fixed. Thus, the fixed result for phase unwrapping will be available half an hour to one hour after an observation.

In chapter 5, several fields of applications were presented. All campaigns were processed with same processing parameters. Merely the selection of the PSs was adjusted to the actual situation. The analysis of these examples shows the flexibility of the algorithm to adapt to the current condition. In case the unwrapping is a simple task due to good weather conditions, the algorithm will deliver accurate results shortly after the observation is finished. The final results will not differ from the a-priori results. In case the conditions are noisy, following observations are used to approve or correct the first estimations.

The advantage of using Kalman filtering is that the state and process model can be extended and modified at will. Thus, all kinds of advance information about the expected displacements can be used to describe and optimize the model as e.g. assumptions on periodicity. Also, other observations types can directly be used as additional input into the filter to simplify the unwrapping as e.g. data from meteorological sensors, GPS, total stations, etc. To be able to make an assessment of the current state of the mass movement, the observations resulting from the real-time analysis could be used as input into a numerical models to simulate and predict critical situations and identify possible trigger effects.

In data simulations, up to a phase standard deviation of 0.8, almost no unwrapping errors occurred during the processing (see Figure 4.14). In the real data experiments, PSs were discarded if their estimated ADI exceeded 0.25. Thus, based on the simulation, no unwrapping errors should occur. However, from the results in the last chapter it can be seen that several unwrapping errors did occur. The problem mainly lies in the determination of the ADI based on the last 20 or 30 images. These measurements might not reflect the current state of the PSs. If the signal noise is temporally unstable, the estimation of ADI may be underestimated for this particular time step. This method can only account for long-term variations of the reflectivity properties. Sudden changes, as e.g. rock falls, rain shower, etc. will not be detected. Furthermore, in the examples the network was updated only with a period of 15 images. Thus, a potential improvement of the processing method is the improvement of the identification of changes in the network. The amplitude time series of the PSs should be analysed to detect these sudden changes. A sudden drop of amplitude at one PS can be an indication for this PS to be removed from the list of PSCs.

A further improvement, which is actually very important for interpretation, is to identify and distinguish reliable and unreliable estimations. Unwrapping errors can probably not be prevented but they should be identified and a value for the reliability, e.g. in form of probabilities, should be made available. One indication can be the probabilities, that are delivered as output from the Kalman filters. A low probability of the finally selected ambiguity indicates a higher chance for unwrapping errors. A further test, for unwrapping errors can be to identify typical patterns, in form of sudden jumps of around 8 mm in time and space, that occur when the ambiguity determination is wrong.

Finally, it can be said that based on the results of the measurement campaigns shown in the last chapter, the algorithm has proven to deliver plausible results even under difficult circumstances. Nevertheless, it is important for the observer to have a sound knowledge about the GB-SAR techniques and the difficulties of analysis to be able to determine the reliability of the measurements.

# References

ADAM, N., KAMPES, B., and EINEDER, M. (2004), Development of a scientific permanent scatterer system: Modifications for mixed ERS/ENVISAT time series. In *ERS-ENVISAT Symposium, 6-10 September 2004, Salzburg, Austria.*

AHUJA, R.K., MAGNANTI, T.L., and ORLIN, J.B. (1993), *Network flows: theory, algorithms, and applications.* Prentic Hall Inc., Englewood Cliffs (NJ).

ALBA, M., BERNADINI, G., GIUSSANI, A., RICCI, P., RONCORONI, F., SCAIONI, M., VALGOI, P., and ZHANG, K. (2008), Measurement of Dam Deformations by Terrestrial Interferometric Techniques. In *International Archives of the Photogrammetry, Remote Sensing and Spatial Information Sciences. Vol. XXXVII. Part B1, 3-11 July 2008, Beijing, China.*

ANGELI, M.G., PASUTO, A., and SILVANO, S. (2000), A critical review of landslide monitoring experiences. *Engineering Geology*, 55(3):133–147. ISSN 0013-7952.

ANTONELLO, G., CASAGLI, N., FARINA, P., LEVA, D., NICO, G., SIEBER, A., and TARCHI, D. (2004), Ground-based SAR interferometry for monitoring mass movements. *Landslides*, 1:21–28. doi: 10.1007/s10346-003-0009-6.

BAMLER, R. (2000), Principles of Synthetic Aperture Radar. *Surveys in Geophysics*, 21:147–157.

BAMLER, R. and HARTL, P. (1998), Synthetic aperture radar interferometry. *Inverse Problems*, 14:R1–R54.

BAR-SHALOM, Y., LI, X.R., and KIRUBARAJAN, T. (2001), *Estimation with applications to tracking and navigation.* Wiley-Interscience.

BERGEN, K.M. and DOBSON, M.C. (1999), Integration of remotely sensed radar imagery in modeling and mapping of forest biomass and net primary production. *Ecological Modelling*, 122(3):257–274.

BITELLI, G., DUBBINI, M., and ZANUTTA, A. (2004), Terrestrial laser scanning and digital photogrammetry techniques to monitor landslide bodies. In *Proceedings of the XXth ISPRS Congress, Istanbul*, volume 35, pages 246–251.

BREKKE, C. and SOLBERG, A.H.S. (2005), Oil spill detection by satellite remote sensing. *Remote Sensing of Environment*, 95(1):1–13.

BROWN, R.G. and HWANG, P.Y.C. (1997), *Introduction to Random Signals and Applied Kalman Filtering.* John Wiley & Sons, inc.

CARBALLO, G.F. and FIEGUTH, P.W. (2000), Probabilistic cost functions for network flow phase unwrapping. *Transactions on Geoscience and Remote Sensing*, 38(5):2192–2201.

COLLISON, A., WADE, S., GRIFFITHS, J., and DEHN, M. (2000), Modelling the impact of predicted climate change on landslide frequency and magnitude in SE England. *Engineering Geology*, 55 (3):205–218. ISSN 0013-7952.

CONSTANTINI, M. (2002), A novel phase unwrapping method based on network programming. *Transactions on Geoscience and Remote Sensing*, 36(3): 813–821. ISSN 0196-2892.

CROSETTO, M., TSCHERNING, C.C., CRIPPA, B., and CASTILLO, M. (2002), Subsidence monitoring using SAR interferometry - Reduction of the atmospheric effects using stochastic filtering. *Geophysical Research Letters*, 29(9):26–1.

CURLANDER, J.C. and MCDONOUGH, R.N. (1991), *Synthetic Aperture Radar: Systems and Signal Processing.* John Wiley & Sons, inc.

CUSACK, R., HUNTLEY, JM, and GOLDREIN, HT. (1995), Improved noise-immune phase-unwrapping algorithm. *Applied Optics*, 34(5):781–789.

DANTZIG, G.B., ORDEN, A., and WOLFE, P. (2003), The generalized simplex method for minimizing a linear form under linear inequality restraints. In *The basic George B. Dantzig.* Stanford University Press.

DELAUNAY, B. (1934), Sur la sphre vide. *Bulletin of Academy of Sciences of the USSR*, VII:793–800.

EICHHORN, A. and SCHMALZ, T. (2010), Investigations to the Calibration of a Numerical Slope Model by Means of Adaptive Kalman-Filtering. In *FIG Congress 2010, Facing the Challenges - Building the Capacity, 11-16 April 2010, Sydney, Australia.*

FERRETTI, A., PRATI, C., and ROCCA, F. (2000), Nonlinear subsidence rate estimation using permanent scatterers in differential SAR interferometry. *Transactions on Geoscience and Remote Sensing*, 38(5):2202–2212.

FERRETTI, A., PRATI, C., ROCCA, F., and OTHERS. (2001), Permanent scatterers in SAR interferometry. *Transactions on Geoscience and Remote Sensing*, 39(1):8–20.

FLYNN, T.J. (1997), Two-dimensional phase unwrapping with minimum weighted discontinuity. *Journal of the Optical Society of America A*, 14(10):2692–2701.

FREEMAN, A. (1992), SAR calibration: An overview. *Transactions on Geoscience and Remote sensing*, 30 (6):1107–1121.

GHIGLIA, D.C. and PRITT, M.D. (1998), *Two-dimensional Phase Unwrapping: Theory, Algorithms, and Software*. Wiley New York.

GILI, J.A., COROMINAS, J., and RIUS, J. (2000), Using Global Positioning System techniques in landslide monitoring. *Engineering Geology*, 55(3):167–192. ISSN 0013-7952.

GOLDSTEIN, R., ZEBKER, H., and WERNER, C. (1988), Satellite radar interferometry - Two-dimensional phase unwrapping. *Radio Science*, 23 (4):713–720.

GREWAL, M.S. and ANDREWS, A.P. (2001), *Kalman filtering: theory and practice using MATLAB*. Wiley New York.

HANSSEN, R.F. (2002), *Radar Interferometry: Data Interpretation and Error Analysis*. Kluwer Academic Publishers.

HARRIS, F.J. (1978), On the use of windows for harmonic analysis with the discrete Fourier transform. *Proceedings of the IEEE*, 66(1):51–83. ISSN 0018-9219.

HERRERA, G., FERNÁNDEZ-MERODO, J.A., MULAS, J., PASTOR, M., LUZI, G., and MONSERRAT, O. (2009), A landslide forecasting model using ground based SAR data: The Portalet case study. *Engineering Geology*, 105:220–230.

HOOPER, A., ZEBKER, H., SEGALL, P., and KAMPES, B. (2004), A new method for measuring deformation on volcanoes and other natural terrains using InSAR persistent scatterers. *Geophysical Research Letters*, 31(23):L23611.

HOOPER, A., SEGALL, P., and ZEBKER, H. (2007), Persistent scatterer InSAR for crustal deformation analysis, with application to Volcán Alcedo, Galápagos. *Journal of Geophysical Research*, 112 (B07407):19.

HORT, M.K. (2009), Exupéry-a mobile fast response system for managing a volcanic crisis. In *AGU Fall Meeting Abstracts*, volume 1, page 2050.

HUNTLEY, J.M. (2001), Three-dimensional noise-immune phase unwrapping algorithm. *Applied Optics*, 40(23):3901–3908.

IPCC. (2007), *Climate Change 2007: Synthesis Report. Contribution of Working Groups I, II and III to the Fourth Assessment Report of the Intergovernmental Panel on Climate Change*. IPCC, Geneva, Switzerland.

ISDR. (2009), *Global Assessment Report on Disaster Risk Reduction*. United Nations, Geneva, Switzerland.

ITOH, K. (1982), Analysis of the phase unwrapping algorithm. *Applied Optics*, 21(14):2470–2470.

IUGS-WGL. (1995), A suggested method for describing the rate of movement of a landslide. *Bulletin of the International Association of Engineering Geology*, 52:75–78.

JUST, D. and BAMLER, R. (1994), Phase statistics of interferograms with applications to synthetic aperture radar. *Applied Optics*, 33(20):4361–4368.

KALMAN, R.E. (1960), A new approach to linear filtering and prediction problems. *Journal of Basic Engineering*, 82(1):35–45.

KAMPES, B. (2006), *Radar Interferometry: Persistent Scatterer Technique*. Springer.

KAMPES, B.M. and HANSSEN, R.F. (2004), Ambiguity resolution for permanent scatterer interferometry. *IEEE Transactions on Geoscience and Remote Sensing*, 42(11):2446–2453.

KLAUSING, H. and HOLPP, W., editors. (2000), *Radar mit realer und synthetischer Apertur: Konzeption und Realisierung*. Oldenbourg Wissenschaftsverlag.

KÖNIG, M., WINTHER, J.G., and ISAKSSON, E. (2001), Measuring snow and glacier ice properties from satellite. *Reviews of Geophysics*, 39(1):1–27.

KRAFT, T., WASSERMANN, J., SCHMEDES, E., and IGEL, H. (2006), Meteorological triggering of earthquake swarms at Mt. Hochstaufen, SE-Germany. *Tectonophysics*, 424(3-4):245–258.

KRAUS, H. (2004), *Die Atmosphäre der Erde*. Springer.

LEACHTENAUER, J.C. and DRIGGERS, R.G. (2001), *Surveillance and reconnaissance imaging systems: modeling and performance prediction*. Artech House Publishers. ISBN 1580531326.

LEE, D.T. and SCHACHTER, B.J. (1980), Two algorithms for constructing a Delaunay triangulation. *International Journal of Parallel Programming*, 9 (3):219–242.

LUENBERGER, D.G. and YE, Y. (2008), *Linear and nonlinear programming*. Springer Verlag.

LUZI, G., PIERACCINI, M., MECATTI, D., NOFERINI, L., GUIDI, G., MOIA, F., and ATZENI, C. (2004), Ground-based radar interferometry for landslides monitoring: Atmospheric and instrumental decorrelation sources on experimental data. *Transactions on Geoscience and Remote Sensing*, 42:2454–2466.

LUZI, G., PIERACCINI, M., MECATTI, D., NOFERINI, L., MACALUSO, G., GALGARO, A., and ATZENI, C. (2006), Advances in groundbased microwave interferometry for landslide survey: a case study. *International Journal of Remote Sensing*, 27: 2331–2350. doi: doi:10.1080/01431160600554975.

MARINKOVIC, P., VAN LEIJEN, F., KETELAAR, G., and HANSSEN, R. (2005), Recursive Persistent Scatterer Interferometry. In *Fringe Workshop, 28 November - 2 December 2005, Frascati, Italy*, volume 610, page 23.

MARTINEZ-VAZQUEZ, A. and FORTUNY-GUASH, J. (2006), Snow Cover Monitoring in the Swiss Alps with a GB-SAR. *Geoscience and Remote Sensing Society Newsletter*, March 2006:11–14.

MASSONNET, D. and FEIGL, K.L. (1998), Radar interferometry and its application to changes in the Earth's surface. *Reviews of Geophysics*, 36(4):441–500.

MASSONNET, D. and SOUYRIS, J.C. (2008), *Imaging with Synthetic Aperture Radar*. EFPL Press.

MEYER, F., KAMPES, B., BAMLER, R., and FISCHER, J. (2005), Methods for Atmospheric Correction in INSAR Data. In *Fringe Workshop, 28 November - 2 December 2005, Frascati, Italy*.

MODARESSI, H. (2006), Climate Change and ground Movements. *Geosciences*, 3:44–49.

MOREIRA, A., KRIEGER, G., HAJNSEK, I., WERNER, M., HOUNAM, D., RIEGGER, S., and SETTELMEYER, E. (2004), TanDEM-X: A TerraSAR-X add-on satellite for single-pass SAR interferometry. In *IEEE International Geoscience and Remote Sensing Symposium, IGARSS, 20-24 September 2004, Anchorage, USA*, pages 1000–1003.

NOFERINI, L., PIERACCINI, M., MECATTI, D., LUZI, G., ATZENI, C., TAMBURINI, A., and BROCCOLATO, M. (2005), Permanent scatterers analysis for atmospheric correction in ground-based SAR interferometry. *Transactions on Geoscience and Remote Sensing*, 43(7):1459–1471. doi: 10.1109/TGRS.2005.848707.

NOFERINI, L., PIERACCINI, M., LUZI, G., MECATTI, D., MACALUSO, G., and ATZENI, C. (2006), Ground-based Radar Interferometry for Terrain Mapping. In *IEEE International Geoscience and Remote Sensing Symposium, IGARSS, 31 July - 4 August 2006, Denver, USA*.

NOFERINI, L., PIERACCINI, M., MECATTI, D., MACALUSO, G., LUZI, G., and ATZENI, C. (2007), DEM by Ground-Based SAR Interferometry. *Geoscience and Remote Sensing Letters*, 4(4):659–663. doi: 10.1109/LGRS.2007.905118.

NOFERINI, L., LUZI, G., PIERACCINI, M., STROZZI, T., and WERNER, C. (2008a), DEM reconstruction examples. Technical report, GALA-HAD Project Deliverable D3.8.

NOFERINI, L., TAKAYAMA, T., PIERACCINI, M., MECATTI, D., MACALUSO, G., LUZI, G., and ATZENI, C. (2008b), Analysis of Ground-Based SAR Data With Diverse Temporal Baselines. *Transactions on Geoscience and Remote Sensing*, 46(6):1614–1623. doi: 10.1109/TGRS.2008.916216.

PAPOULIS, A. (1965), *Probability, random variables, and stochastic processes*, volume 73660116. McGraw-Hill New York.

PAULOSE, A. High radar range resolution with the step frequency waveform. Master's thesis, Naval Postgraduate School, (1994).

PIERACCINI, M., LUZI, G., and ATZENI, C. (2001), Terrain mapping by ground-based interferometric radar. *Transactions on Geoscience and Remote Sensing*, 39(10):2176–2181. doi: 10.1109/36.957280.

PIERACCINI, M., CASAGLI, N., LUZI, G., TARCHI, D., MECATTI, D., NOFERINI, L., and ATZENI, C. (2003), Landslide monitoring by ground-based radar interferometry: a field test in Valdarno (Italy). *International Journal of Remote Sensing*, 24:1385–1391. doi: 10.1080/0143116021000044869.

PIERACCINI, M., LUZI, G., MECATTI, D., NOFERINI, L., and ATZENI, C. (2006), Ground-based SAR for short and long term monitoring of unstable slopes. In *Proceedings of the 3rd European Radar Conference, EuRAD, September 2006, Manchester, UK*.

RABUS, B., EINEDER, M., ROTH, A., and BAMLER, R. (2003), The shuttle radar topography mission- a new class of digital elevation models acquired by spaceborne radar. *ISPRS Journal of Photogrammetry and Remote Sensing*, 57(4):241–262.

REINHARDT, P. (2009), *Bedienungsanleitung Sensoren mit Datalogger*. Reinhardt System- und Messelectronic GmbH.

RÖDELSPERGER, S., BECKER, M., GERSTENECKER, C., LÄUFER, G., SCHILLING, K., and STEINECK, D. (2010a), Digital elevation model with the ground-based SAR IBIS-L as basis for volcanic deformation monitoring. *Journal of Geodynamics*, 49(3-4):241–246. ISSN 0264-3707.

RÖDELSPERGER, S., LÄUFER, G., GERSTENECKER, C., and BECKER, M. (2010b), Monitoring of displacements with ground-based microwave interferometry: IBIS-S and IBIS-L. *Journal of Applied Geodesy*, 4(1):41–54. ISSN 1862-9016.

RÖDELSPERGER, S., LÄUFER, G., GERSTENECKER, C., and BECKER, M. (2010c), Terrestrische Mikrowelleninterferometrie - Prinzip und Anwendungen. *Allgemeine Vermessungsnachrichten*, 10:324–333.

ROTHROCK, D.A., CARSEY, F.D., CURLANDER, J.C., HOLT, B., KWOK, R., and WEEKS, W.F. (1992), Ice tracking techniques, implementation, performance, and applications. *Advances in Space Research*, 12:141–147.

RUDOLF, H., LEVA, D., TARCHI, D., and SIEBER, AJ. (1999), A mobile and versatile SAR system. In *IEEE 1999 International Geoscience and Remote Sensing Symposium, 1999. IGARSS'99 Proceedings*, volume 1.

SCHMALZ, T., BUHL, V., and EICHHORN, A. (2010), An adaptive Kalman-filtering approach for the calibration of finite difference models of mass movements. *Journal of Applied Geodesy*, in press:9. ISSN 1862-9016.

SCHULER, D.L., LEE, J.S., KASILINGAM, D., and POTTIER, E. (2004), Measurement of ocean surface slopes and wave spectra using polarimetric SAR image data. *Remote Sensing of Environment*, 91(2): 198–211.

SEARLE, R. (1980), Tectonic pattern of the Azores spreading centre and triple junction. *Earth and Planetary Science Letters*, 51(2):415–434. ISSN 0012-821X.

SILVEIRA, D., GASPAR, JL, FERREIRA, T., and QUEIROZ, G. (2003), Reassessment of the historical seismic activity with major impact on S. Miguel Island (Azores). *Natural Hazards and Earth System Sciences*, 3:615–623.

SOUSA, J.J., HOOPER, A.J., HANSSEN, R.F., and BASTOS, L.C. (2009), Comparative Study of Two Different PS-InSAR Approaches: DePSI vs. StaMPS. In *Fringe Workshop, 30 November - 4 December 2009, Frascati Italy*.

STROZZI, T., FARINA, P., CORSINI, A., AMBROSI, C., THÜRING, M., ZILGER, J., WIESMANN, A., WEGMÜLLER, U., and WERNER, C. (2005), Survey and monitoring of landslide displacements by means of L-band satellite SAR interferometry. *Landslides*, 2(3):193–201.

TARCHI, D., RUDOLF, H., PIERACCINI, M., and ATZENI, C. (2000), Remote monitoring of buildings using a ground-based SAR: application to cultural heritage survey. *International Journal of Remote Sensing*, 21(18):3545–3551. doi: 10.1080/014311600750037561.

TARCHI, D., CASAGLI, N., FANTI, R., LEVA, D., LUZI, G., PASUTO, A., PIERACCINI, M., and SILVANO, S. (2003), Landslide monitoring by using ground-based SAR interferometry: an example of application to the Tessina landslide in Italy. *Engineering Geology*, 68:15–30.

WALLENSTEIN, N., DUNCAN, A., CHESTER, D., and MARQUES, R. (2007), Fogo volcano (Sao Miguel, Azores): a hazardous edifice. *Geomorphologie: relief, processus, environnement*, 3:259–270.

WRIGHT, T., FIELDING, E., and PARSONS, B. (2001), Triggered slip: observations of the 17 August 1999 Izmit (Turkey) earthquake using radar interferometry. *Geophysical Research Letters*, 28(6):1079–1082.

ZANGERL, C., EBERHARDT, E., SCHÖNLAUB, H., and ANEGG, J. (2007), Deformation behaviour of deep-seated rockslides in crystalline rock. In *Proceeding of the 1st Canada-US Rock Mechanics Symposium, Vancouver, Canada*, pages 901–908.

ZEBKER, H.A., ROSEN, P.A., and HENSLEY, S. (1997), Atmospheric effects in interferometric synthetic aperture radar surface deformation and topographic maps. *Journal of Geophysical Research*, 102(B4):7547–7563.

# List of Acronyms

| | |
|---|---|
| ADI | Amplitude Dispersion Index |
| APS | Atmospheric Phase Screen |
| BMBF | Bundesministerium für Bildung und Forschung |
| DEM | Digital Elevation Model |
| DePSI | Delft PS-InSAR Processing Package |
| ERS | European Remote Sensing Satellite |
| ESA | European Space Agency |
| GB-SAR | Ground based Synthetic Aperture Radar |
| GPS | Global Positioning System |
| IBIS-L | Image By Interferometric Survey |
| InSAR | Interferometric Synthetic Aperture Radar |
| IDS | Ingegneria dei Sistemi S.p.A. |
| ILS | Integer Least Squares |
| JRC | Joint Research Center |
| KASIP | Knowledge-Based Alarm System with Identified Deformation Predictor |
| LAN | Local Area Network |
| LiSA | Linear Synthetic Aperture Radar |
| LOS | Line Of Sight |
| MCF | Minimum Cost Flow |
| MMAE | Multiple Model Adaptive Estimation |
| NASA | National Aeronautics and Space Administration |
| PDF | Probability Density Function |
| PS | Persistent Scatterer |
| PS | Permanent Scatterer |
| PSC | Persistent Scatterer Candidate |
| PSC | Permanent Scatterer Candidate |
| PSI | Persistent Scatterer Interferometry |
| RCS | Radar Cross Section |
| SAR | Synthetic Aperture Radar |
| SCR | Signal to Clutter Ratio |
| SFCW | Stepped Frequency Continuous Wave |
| SNR | Signal to Noise Ratio |
| SRTM | Shuttle Radar Topography Mission |
| StaMPS | Stanford Method for Persistent Scatterers |
| USB | Universal Serial Bus |
| VFRS | Volcano Fast Response System |
| WLAN | Wireless LAN |

# List of Symbols

**Scalars**

| Symbol | Description | Symbol | Description |
|---|---|---|---|
| $a$ | Amplitude | $m$ | Number of state parameters |
| $a$ | Polynomial coefficient | $m$ | Polynomial degree |
| $a$ | Reflector edge length | $m_a$ | Mean amplitude |
| $A$ | Set of arcs | $n$ | Phase ambiguity |
| $b$ | Reflector edge length | $n$ | Refractive index |
| $b$ | Supply value | $N$ | Number of frequency steps |
| $B$ | Bandwidth | $N$ | Number of Kalman filters |
| $B_f$ | Bandwidth (total frequency shift due to movement on rail) | $N$ | Set of nodes |
| | | $N$ | Window length |
| $B_s$ | Spatial baseline | $p$ | Number of constraints |
| $B_t$ | Temporal baseline | $p$ | Probability |
| $c$ | Calibration factor for amplitude dispersion index | $P$ | Horizontal distance |
| | | $P$ | Atmospheric pressure |
| $c$ | Costs | $P_e$ | Transmitted power |
| $c$ | Speed of light | $P_n$ | Noise power |
| $d$ | Displacement in line of sight | $P_r$ | Received power |
| $D_a$ | Amplitude dispersion index | $q, r, s$ | Indices for arcs |
| $e$ | Partial pressure of water vapour | $r$ | Number of arcs |
| $E$ | Saturation vapour pressure | $r, R$ | Range |
| $f$ | Frequency | $S$ | Physical effective area of a radar reflector |
| $f$ | Function in time domain | | |
| $f$ | Conditional density | $SNR$ | Signal to noise ratio |
| $F$ | Function in frequency domain | $SNR^{thermal}$ | Thermal signal to noise ratio |
| $G$ | Antenna gain | $t$ | Time |
| $G$ | Directed graph | $T$ | Temperature |
| $G_c$ | Number of independent cross-range observations | $u$ | Upper limit for ambiguities |
| | | $U$ | Radial basis function |
| $G_r$ | Number of independent range observations | $v$ | Velocity |
| | | $w$ | Window function |
| $h$ | Relative humidity | $x$ | Flow |
| $h$ | Root mean square variation of surface height | $x, y$ | Local 2D coordinate system with origin in center of rail |
| | | $X, Y, Z$ | Local 3D coordinate system with origin in center of rail |
| $H$ | Objective function | | |
| $i$ | Imaginary number | $z$ | Complex observation |
| $i,j,k,l,m,n$ | Index | $z$ | Minimum cost flow objective function |
| $I_0$ | Zeroth order modified Bessel function of the first kind | $\overline{z}, z$ | Height |
| $k$ | Angular wavenumber | $\alpha$ | Azimuth with respect to the look direction of the instrument |
| $K$ | Number of possible ambiguities | | |
| $l$ | Atmospheric loss | $\beta$ | Elevation angle |
| $l$ | Lower limit for ambiguities | $\beta$ | Kaiser window shaping parameter |
| $l$ | Number of observations | $\beta_s$ | Spatial baseline angle with respect to the vertical |
| $L$ | Length of antenna | | |
| $L_s$ | Length of synthetic antenna (rail) | $\gamma$ | Coherence |

| | | | |
|---|---|---|---|
| $\gamma$ | Local incidence angle with respect to slope inclination | $\phi_{topo}$ | Interferometric phase due to topography |
| $\delta_c$ | Cross range resolution | $\psi$ | Absolute / unwrapped double differenced phase at arc |
| $\delta_{gr}$ | Ground range resolution | $\psi^u$ | Itoh-unwrapped double differenced phase at arc |
| $\delta_r$ | Range resolution | | |
| $\delta_{rc}$ | Real Aperture Radar cross range resolution | $\psi^w$ | Wrapped double differenced phase at arc |
| $\theta$ | Slope inclination with respect to horizontal | $\psi_{atm}$ | Double differenced phase due to atmosphere |
| $\lambda$ | Wavelength | $\psi_{disp}$ | Double differenced phase due to displacement |
| $\nu$ | Spatial frequency | | |
| $\sigma$ | Radar cross section | $\psi_{lin}$ | Double differenced phase containing only linear signals |
| $\sigma$ | Standard deviation | | |
| $\sigma^0$ | Backscatter coefficient | $\psi_{lindisp}$ | Double differenced phase containing only linear displacement |
| $\tau$ | Pulse width | | |
| $\varphi$ | Absolute / unwrapped phase | $\psi_{noise}$ | Double differenced phase due to noise |
| $\varphi^w$ | Wrapped phase | $\psi_{nonlin}$ | Double differenced phase containing only nonlinear signals |
| $\phi$ | Absolute / unwrapped interferometric phase | | |
| $\phi^w$ | Wrapped interferometric phase | $\psi_{nonlindisp}$ | Double differenced phase containing only nonlinear displacement |
| $\phi_{atm}$ | Interferometric phase due to atmospheric changes | $\psi_{topo}$ | Double differenced phase due to topography |
| $\phi_{disp}$ | Interferometric phase due to object displacement | $\omega$ | Angular velocity |
| $\phi_{noise}$ | Interferometric phase due to noise | | |

## Vector and matrices

| Symbol | Description | Symbol | Description |
|---|---|---|---|
| $\mathbf{a}_i$ | Column $i$ of matrix $\mathbf{A}$ | $\mathbf{Q}$ | Covariance matrix of process noise |
| $\mathbf{A}$ | Triangle - arc relations for minimum cost flow | $\mathbf{R}$ | Covariance matrix of measurement noise |
| $\mathbf{b}$ | Constraints | $\mathbf{s}$ | Unit vector of line of sight direction |
| $\mathbf{B}$ | Basis matrix | $\mathbf{T}$ | State transition matrix |
| $\mathbf{c}$ | Cost vector | $\mathbf{u}$ | Upper bound vector |
| $\mathbf{d}$ | Innovations | $\mathbf{v}$ | Measurement noise |
| $\mathbf{d}_{xyz}$ | 3D displacement vector | $\mathbf{w}$ | Process noise |
| $\mathbf{D}$ | Covariance matrix of innovations | $\mathbf{w}$ | Weights |
| $\mathbf{H}$ | Measurement matrix | $\mathbf{x}$ | Flow vector |
| $\mathbf{K}$ | Kalman gain matrix | $\mathbf{x}$ | State vector |
| $\mathbf{l}^w$ | Observation vector containing $\psi^w$ | $\hat{\mathbf{x}}^-$ | A priori estimate of state vector |
| $\mathbf{l}^u$ | Observation vector containing $\psi^u$ | $\hat{\mathbf{x}}^+$ | A posteriori estimate of state vector |
| $\mathbf{n}$ | Ambiguity vector | $\mathbf{x}_B$ | Basis variables vector |
| $\mathbf{N}$ | Nonbasis matrix | $\mathbf{x}_N$ | Nonbasis variables vector |
| $\mathbf{P}^-$ | A priori covariance matrix of state vector | $\mathbf{z}$ | Measurement vector |
| $\mathbf{P}^+$ | A posteriori covariance matrix of state vector | | |

## Operators

| Symbol | Description |
|---|---|
| $d(\,\cdot\,)$, $\partial(\,\cdot\,)$ | Differential operator |
| $\Delta(\,\cdot\,)$ | Difference operator |
| $E\,\{\,\cdot\,\}$ | Expectation value |

| Symbol | Description |
|---|---|
| $\mathcal{W}\,\{\,\cdot\,\}$ | Wrapping operator $\mathcal{W}\,\{\,\cdot\,\} = \mod\{\,\cdot\,+\pi\}$ |
| $(\,\cdot\,)^{*}$ | Complex conjugation |
| $\mod\{\,\cdot\,,2\pi\}$ | Modulus $2\pi$ |

# A  Standard Deviation of Interferometric Phase

According to section 2.2, the interferometric phase is a sum of several effects:

$$\phi^w = \phi_{topo} + \phi_{disp} + \phi_{atm} + \phi_{noise} - 2\pi n. \tag{A.1}$$

## A.1  Atmosphere

For constant atmospheric properties along the propagation path with length $r$, the atmospheric phase $\phi_{atm}$ is given by (see also section 2.2.1)

$$\phi_{atm} = \frac{4\pi}{\lambda} \left( A\frac{P}{T}r + B\frac{e}{T^2}r \right), \tag{A.2}$$

with $A = 7.76 \times 10^{-5}$ K/hPa, $B = 3.73 \times 10^{-1}$ K$^2$/hPa, pressure $P$ in hPa, temperature $T$ in Kelvin, $e = hE/100$, humidity $h$ in percent, $E = c \cdot \exp(a(T-273)/(T-b))$, $c = 6.107$, $a = 17.26939$ and $b = 36.86$ (Zebker et al., 1997; Kraus, 2004). If temperature $T$, humidity $h$ and pressure $P$ are observed by a weather station nearby the radar with standard deviations $\sigma_T$, $\sigma_h$ and $\sigma_P$, the standard deviation of the atmospheric phase $\sigma_{\phi_{atm}}$ can be estimated by

$$\sigma_{\phi_{atm}}^2 = \left( \frac{\delta\phi_{atm}}{\delta T} \right)^2 \sigma_T^2 + \left( \frac{\delta\phi_{atm}}{\delta h} \right)^2 \sigma_h^2 + \left( \frac{\delta\phi_{atm}}{\delta P} \right)^2 \sigma_P^2, \tag{A.3}$$

with the partial derivatives

$$
\begin{aligned}
\frac{\delta\phi_{atm}}{\delta T} &= \frac{4\pi}{\lambda} \left( -A\frac{P}{T^2} + Be\frac{a(273-b)}{T^2(T-b)^2} - \frac{2}{T^3} \right) r, \\
\frac{\delta\phi_{atm}}{\delta h} &= \frac{4\pi}{\lambda} \frac{BE}{100T^2}r, \\
\frac{\delta\phi_{atm}}{\delta P} &= \frac{4\pi}{\lambda} \frac{A}{T}r.
\end{aligned}
\tag{A.4}
$$

## A.2  Topography

The relation of height $z$ and topographic phase $\phi_{topo}$ is given by (see also section 2.2.2)

$$
\begin{aligned}
z &= \overline{z}\cos\beta_s + r_0\sin\beta_s, \\
\text{with} \qquad r_0 &= \sqrt{r_1^2 - \overline{z}^2}, \\
\text{and} \qquad \overline{z} &= \frac{\lambda}{4\pi}\frac{r_1}{B_s}\phi_{topo}.
\end{aligned}
\tag{A.5}
$$

The standard deviation $\sigma_z$ that can be acchieved for $z$, depends on the standard deviations of phase measurement $\sigma_{\phi_{topo}}$, spatial baseline $\sigma_{B_s}$ and baseline angle $\sigma_{\beta_s}$ (Noferini et al., 2008a)

$$\sigma_z^2 = \left( \frac{\delta z}{\delta\phi_{topo}} \right)^2 \sigma_{\phi_{topo}}^2 + \left( \frac{\delta z}{\delta B_s} \right)^2 \sigma_{B_s}^2 + \left( \frac{\delta z}{\delta\beta_s} \right)^2 \sigma_{\beta_s}^2, \tag{A.6}$$

with the partial derivatives

$$
\begin{aligned}
\frac{\delta z}{\delta\phi_{topo}} &= \left( \cos\beta_s + \frac{\overline{z}\sin\beta_s}{r_0} \right) \frac{\lambda}{4\pi}\frac{r_1}{B_s}, \\
\frac{\delta z}{\delta B_s} &= - \left( \cos\beta_s + \frac{\overline{z}\sin\beta_s}{r_0} \right) \frac{\lambda}{4\pi}\frac{r_1}{B_s^2}\phi_{topo}, \\
\frac{\delta z}{\delta\beta_s} &= r_0\cos\beta_s - \overline{z}\sin\beta_s.
\end{aligned}
\tag{A.7}
$$

## A.3  Coherence, SNR and Phase Standard Deviation

| Coherence $|\gamma|$ | SNR according to equation 2.42 | Phase standard deviation $\sigma_\phi$ according to equation 2.47 | Standard deviation of displacement for Ku-band radar ($\lambda = 17.4$ mm) |
|:---:|:---:|:---:|:---:|
| 0.5 | 0 dB | | |
| 0.8 | 6.0 dB | 0.53 rad (30°) | 1.50 mm |
| 0.9 | 9.5 dB | 0.34 rad (20°) | 0.95 mm |
| 0.95 | 12.8 dB | 0.23 rad (13°) | 0.65 mm |
| 0.99 | 20.0 dB | 0.10 rad (5.8°) | 0.28 mm |
| 0.999 | 30.0 dB | 0.03 rad (1.8°) | 0.09 mm |
| 0.9999 | 40.0 dB | 0.01 rad (0.6°) | 0.03 mm |

Table A.1: Relation between coherence, SNR and standard deviation of phase and displacement measurement.

# B Results for Quarry (Dieburg, Germany)
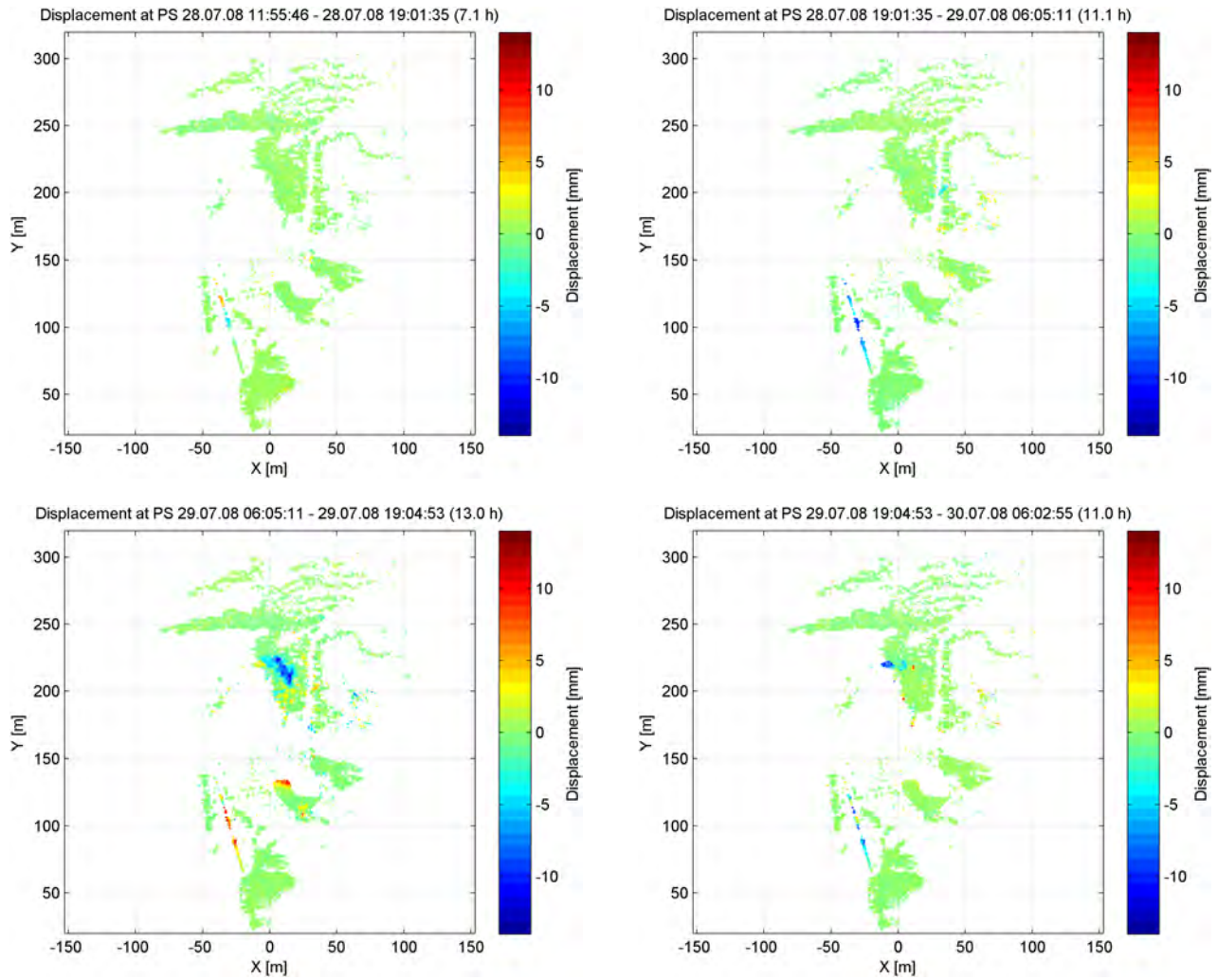


Figure B.1: Displacement observed during day and night between 28. - 30.07.2008 in Dieburg, Germany. The displacements are corrected for atmosphere using meteorological observations.
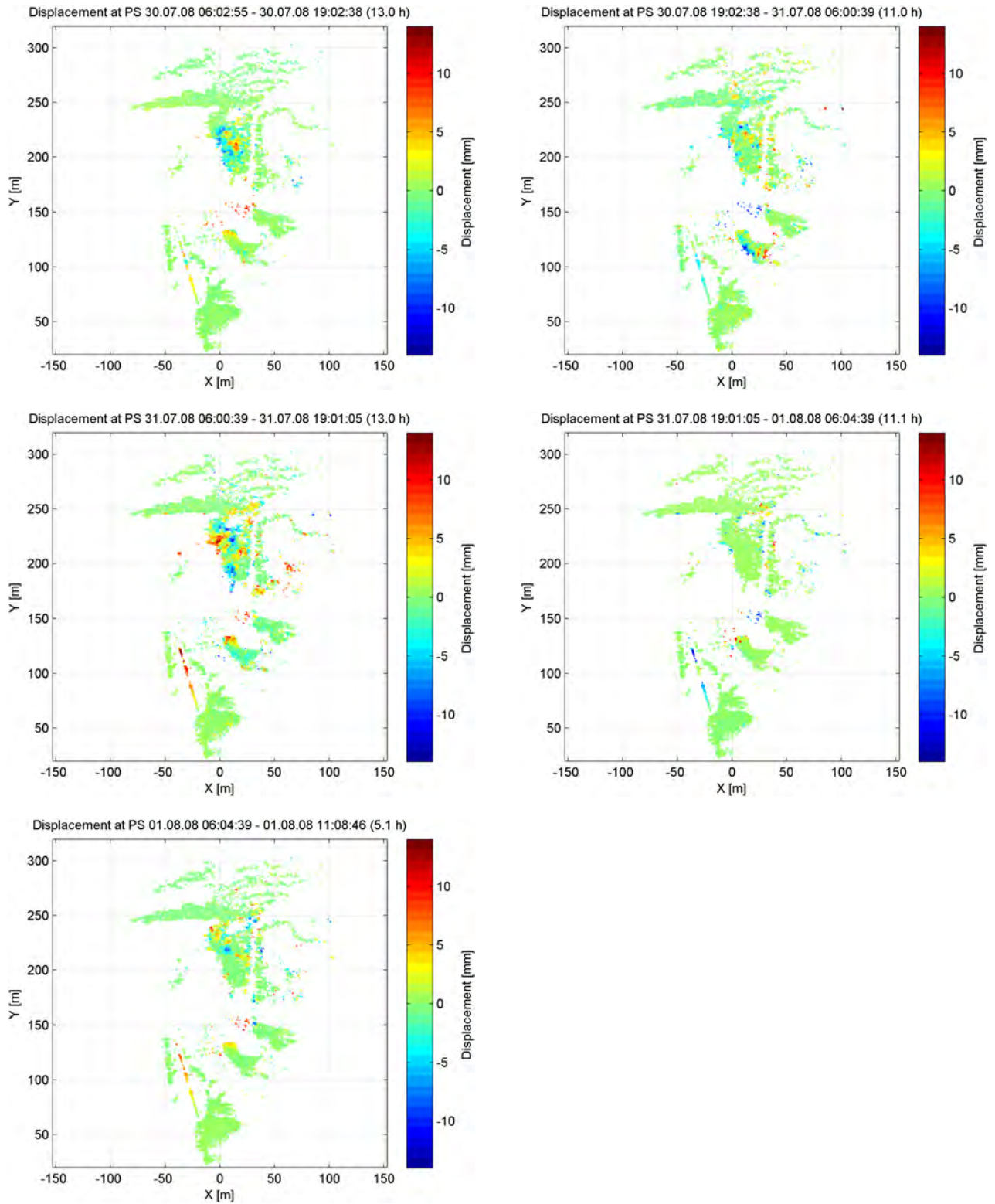
Figure B.2: Displacement observed during day and night between 30.07. - 01.08.2008 in Dieburg, Germany. The displacements are corrected for atmosphere using meteorological observations.

# Danksagung

# Lebenslauf

| | |
|---|---|
| **Name:** | Sabine Rödelsperger |
| **Geburtsdatum:** | 29.10.1981 |
| **Geburtsdatum:** | Offenbach am Main |

## Schulausbildung

| | |
|---|---|
| 1988 - 1992 | **Grundschule Heubach, Groß-Umstadt** |
| 1992 - 2001 | **Max-Planck-Gymnasium, Groß-Umstadt**<br>Abschluss: Abitur |

## Studium

| | |
|---|---|
| Okt. 2001 - Jul. 2006 | **Technische Universität Darmstadt**<br>Studium Vermessungswesen mit Vertiefungsrichtung Geomatik,<br>Abschluss: Diplom-Vermessungsingenieur |
| Nov. 2005 - Jun. 2006 | **Curtin University of Technology, Perth, Australien**<br>Auslandsaufenthalt zum Anfertigen der Diplomarbeit |

## Berufstätigkeit

| | |
|---|---|
| seit Jul. 2006 | **Technische Universität Darmstadt**<br>Wissenschaftliche Mitarbeiterin am Institut für Physikalische Geodäsie |